Asphaltene Gasification : Soot Formation and Metal Distribution

by

Vinoj Kurian

A thesis submitted in partial fulfillment of the requirements for the degree of

Doctor of Philosophy

in

CHEMICAL ENGINEERING

Department of Chemical and Materials Engineering

University of Alberta

Abstract

Athabasca oil sands contain 8 to 14% bitumen and are recovered using surface mining or steam assisted gravity drainage (SAGD). During primary upgrading of bitumen, the vacuum residuum from the distillation column is sent to the solvent de-asphalting unit where a paraffinic solvent is used to remove the high carbon content asphaltenes from the vacuum tower bottoms. These asphaltenes, about one-third of the vacuum residuum, are liquid at operating temperatures and are very problematic in bitumen upgrading facilities. Considering factors such as an increase in world energy demand, large reserves of Canadian oil sands, improved upgrading technologies and an alternative to natural gas for SAGD operation, asphaltene gasification could be a great option to maximize its usability and reduce the waste product.

In this work, the soot formed during the pyrolysis, partial oxidation and steam gasification of Athabasca asphaltene in an electrically heated entrained-flow reactor is analyzed. The effects of feed particle size, temperature, and residence time on the properties of soot particles were investigated for pyrolysis. The experiments were conducted at temperatures between 800 °C and 1400 °C and the residence time was varied between 5 to 12 s by controlling the carrier gas nitrogen flow rate. The asphaltene feed particle size was varied from 53 to 212 μm. Morphological, structural, and elemental properties of collected soot were also investigated. The asphaltene devolatilizes to produce char, light gases and tar. The feed asphaltene particle size had a negligible effect on the properties of the soot formed. The yield of soot formed increased with pyrolysis temperature. It was observed that the average size of primary

soot particles decreases with an increase in temperature. With increase in residence time the average size of the primary soot particles increases.

Vanadium, nickel, and other trace metal distribution is investigated in char and soot formed during pyrolysis, partial oxidation, and steam gasification. The pyrolysis temperature plays a major role in the trace metal content of the char and soot. With an increase in the pyrolysis temperature, the V and Ni contents decrease for both char and soot. An increase in the stoichiometric oxygen content decreases the soot yield during partial oxidation of asphaltenes as a result of the increase in the oxygen/carbon ratio. It is found that the V and Ni contents in both the char ash and soot ash decrease with an increase in stoichiometric oxygen in the feed. During asphaltene gasification with steam, the V content increases with the increase in the steam/fuel weight ratio for both char and soot. The Ni content slightly decreases in char with an increase in the steam/fuel ratio, whereas the Ni content increases in soot with an increase in the steam/fuel ratio.

The soot-water, soot-cake and cooler fouling samples collected from an industrial asphaltene gasifier are analyzed to compare with the soot from lab scale entrained-flow reactor. The metal species evolved during gasification are of different types and major part of it is captured or associated with soot formed and exit the gasification system as soot-water and soot-cake. But a minor quantity of metals which are not associated with soot are getting deposited when cooled in the syngas cooler. The high metallic content of the soot-water and soot-cake shows that collection of metallic species, the act for which soot blowing is intended, has been to some extent successful in preventing slag formation in the gasifier. The very low soot content in the fouling sample (2-3 % soot) collected from the syngas cooler concludes that the deposits are formed in the cooler wall with a different mechanism for which soot blowing has not had a very positive effect.

A CFD model is developed using ANSYS FLUENT by incorporating the single rate devolatilization model, volumetric species transport reactions and Moss-Brooks-Hall soot model into the basic continuity, momentum and energy equations. The model acts as a simple tool to estimate the soot formation in a reactor where the reaction conditions are favorable for soot formation. The influence of different steps of soot formation like nucleation, coagulation, and surface growth on the soot formation can be analyzed using the model.

Preface

The format of this thesis is a compilation of several papers; some of which are published and others are to be submitted for publication. Some of the papers are co-authored and the following list indicates the contributions for each paper.

Chapter 1: Introduction: Original work by Vinoj Kurian.

Chapter 2: Literature Review: Original work by Vinoj Kurian.

Chapter 3: Experimental Section: Original work by Vinoj Kurian.

Chapter 4: A version of this chapter has been published as "Analysis of Soot Formed during the Pyrolysis of Athabasca Oil Sand Asphaltenes" co-authored by Vinoj Kurian, Nirlipt Mahapatra, Ben Wang, Mehdi Alipour, Frans Martens, and Rajender Gupta in *Energy and Fuels*, 2015, 29, 6823–6831. Experiments in the entrained-flow reactor were conducted by Vinoj Kurian in collaboration with Nirlipt Mahapatra and Ben Wang, involving collection of char and soot. We also worked together for modification of the reactor setup, and a few common experimental characterizations. Vinoj Kurian was responsible for characterization of the soot samples such as SEM, TEM, and CHNS, data analysis and manuscript composition and preparation. Frans Martens was responsible for reviewing results, providing insight based on industrial perspective and proof reading the manuscript. Mehdi Alipour and Rajender Gupta supervised the project, assisted with data interpretation and proofread the manuscript prior to submission.

Chapter 5: A version of this chapter has been published as "Distribution of Vanadium, Nickel, and Other Trace Metals in Soot and Char from Asphaltene Pyrolysis and Gasification" co-authored by Vinoj Kurian and Rajender Gupta in *Energy and Fuels*, 2016, 30, 1605–1615. Vinoj Kurian was responsible for conducting the experiments, characterizing the samples, data analysis and interpretation as well as manuscript preparation. Rajender Gupta supervised the work and assisted with data interpretation and proofread the manuscript prior to submission.

Chapter 6: A version of this chapter is to be submitted as "Computational Fluid Dynamics Modeling of Soot Formation from Asphaltene Gasification" co-authored by Vinoj Kurian, Andre Bader, Petr Nikrityuk, and Rajender Gupta. It is also accepted for presentation at 8^{th} International Freiberg Conference on IGCC & XtL Technologies, 12–16 June 2016, Cologne, Germany. The geometry creation and meshing of the entrained-flow reactor were done by Andre Bader and Vinoj Kurian. Vinoj Kurian was responsible for defining the problem, modeling the physics, carried out the simulations, post processing, data interpretation and manuscript preparation. Petr Nikrityuk and Rajender Gupta supervised the work and assisted with data interpretation and proofread the manuscript prior to submission.

Chapter 7: Conclusion: Original work by Vinoj Kurian.

Dedicated to my Parents & Teachers

Acknowledgements

I express my deep gratitude to my research supervisor, Dr. Rajender Gupta, for his constant support, encouragement and guidance throughout this work and for providing many opportunities to work in different research projects in the group. Discussions with him always resulted in new insights for me. His knowledge, integrity, commitment and gentleness have been an inspiration to me.

I also acknowledge the financial support provided by Nexen Energy ULC., Helmholtz-Alberta Initiative (HAI), Canadian Centre for Clean Coal / Carbon and Mineral Processing Technologies (C^5MPT) and Natural Sciences and Engineering Research Council of Canada (NSERC). I gratefully thank Dr. Frans Martens and Mr. Pieter van Nierop from Nexen Energy for their valuable comments and suggestions during the monthly progress meetings. I would also like to thank my supervisory committee members; Dr. Robert Hayes and Dr. Vinay Prasad, for their insightful comments and scientific discussions that have helped me to complete this work more effectively.

I am thankful to my senior colleagues Dr. Farshid Vejahati, Mr. Behnam Berahman and Dr. Seyyedali Hosseini for assisting me in learning about the entrained-flow reactor experimental set up. I am also thankful to Dr. Shan Ramasamy and Dr. Moshfiqur Rahman for helping me in preparing the standard operating procedure and risk assessment and making the course of my experiments hazard free and safe. I greatly appreciate the help and assistance of Mr. Nirlipt Mahapatra, Dr. Ben Wang, Dr. Mehdi Alipour, Ms. Satarupa

Dhir and Dr. Deepak Pudasainee during the course of my project.

I would also like to thank Dr. Nathan Gerein, Mr. Walter Boddez, Mr. Shiraz Merali, Mr. Wayne Moffat for their technical help for my research. I would also like to appreciate the help of all the technicians and staff of the Department of Chemical and Materials Engineering, for their services during the course of my work. I am thankful to all C^5MPT group members for their effort in conducting routine safety inspections and creating a safe work place.

I would like to thank Almighty for blessing me so much to achieve my dream. Last but not the least I would like to thank my whole family members, especially my wife Sony and my son Immanuel for their love, understanding, mental support and encouragement throughout my research which were more crucial for the successful completion of my research.

Contents

Page

Contents **x**

List of Tables **xii**

List of Figures **xiii**

1 Introduction **1**

1.1 Canada's Oilsands 1

1.2 Gasification 3

1.3 Soot 5

1.4 Objectives 7

1.5 Thesis Outline 8

2 Literature Review **10**

2.1 Asphaltenes 10

2.2 Gasification Theory 14

2.2.1 Fixed Bed Gasifier 16

2.2.2 Fluidized bed gasifier 17

2.2.3 Entrained flow gasifier 19

2.3 Asphaltene / Heavy oil Gasification 20

2.4 Soot Formation 23

2.5 Mechanism of Soot Formation 29

2.6 Metals in Asphaltene 33

3 Experimental Section **39**

3.1 Experimental Setup 39

3.2 Feed Asphaltene 46

3.3 Thermal Analysis of Asphaltene 48

4 Analysis of Pyrolysis Soot **50**
4.1 Introduction . . . 50
4.2 Results and Discussion . . . 52
4.2.1 Effect of Feed Particle Size . . . 56
4.2.2 Effect of Pyrolysis Temperature . . . 58
4.2.3 Effect of Residence Time . . . 67
4.3 Conclusions . . . 69

5 Metal Distribution in Soot **71**
5.1 Introduction . . . 71
5.2 Entrained-flow Reactor Experiments . . . 75
5.2.1 Pyrolysis . . . 75
5.2.2 Partial Oxidation . . . 85
5.2.3 Steam Gasification . . . 91
5.3 Soot Formation in an Industrial Gasifier . . . 94
5.3.1 Syngas Cooler Fouling Deposit . . . 95
5.3.2 Soot Water and Soot Cake . . . 97
5.3.3 TEM of Soot Water and Soot Cake samples . . . 99
5.4 Conclusions . . . 101

6 CFD Modeling of Soot Formation **105**
6.1 Introduction . . . 105
6.2 Modeling Methodology . . . 107
6.2.1 Governing Equations . . . 109
6.2.2 Boundary conditions . . . 114
6.2.3 Numerical method . . . 115
6.3 Results and Discussion . . . 116
6.4 Conclusions . . . 121

7 Conclusions and Recommendations **124**
7.1 Conclusions . . . 124
7.2 Recommendations for future work . . . 127

Bibliography **129**

A Appendix **140**
A.1 Temperature calibration of the reactor . . . 140

A.2 Process Flow Diagram of the experimental set up 142

List of Tables

2.1 Typical properties of asphaltenes from various origins [22] . . . 11
2.2 Element type and chemical form in fuel oil [61] 35

3.1 Cascade Impactor Stage Data [68] 45
3.2 Proximate and Ultimate Analysis of Asphaltene. 46

4.1 Ultimate Analysis of the Soot Collected for Different Feed Particle Sizes 55

5.1 XRF Elemental Analyses of Asphaltene Ash and Pyrolysis Char Ash 83
5.2 XRF Elemental Analysis of Pyrolysis Soot Ash 84
5.3 XRF Elemental Analyses of Partial Oxidation Char Ash and Soot Ash 87
5.4 XRF Elemental Analyses of Steam Gasification Char Ash and Soot Ash 93
5.5 XRF Elemental Analyses of soot cake 99

6.1 Boundary conditions for pyrolysis simulation 114
6.2 Boundary conditions for partial oxidation simulation 115

List of Figures

1.1 Characteristics of oil sands [5]. 2
1.2 Primary upgrading of bitumen [4]. 4
1.3 Gasification-based energy conversion options [9]. 5

2.1 Separation of asphaltenes from petroleum residuum. 12
2.2 Structure of asphaltene molecule [25]. 13
2.3 Modified Yen model for the asphaltene structure [30]. 14
2.4 Fixed bed gasifier [31]. 17
2.5 Fluidized bed gasifier [31]. 18
2.6 Entrained-flow gasifier [31]. 18
2.7 Heterogeneous phase reaction model [33]. 21
2.8 Schematic representation of single bio-oil droplet gasification [35]. 22
2.9 Micrograph of diesel soot [36]. 23
2.10 Secondary pyrolysis processes and products [45]. 25
2.11 Scheme of soot formation process [52]. 29
2.12 Diesel soot formation mechanism [19]. 30
2.13 Coagulation of soot particles [55]. 32
2.14 Main existence forms of vanadium and nickel in asphaltene. [61]. 34
2.15 TEM images of the obtained vanadium oxides: (a) the $VO(Ac)_2$ as precursor; (b) the $VOSO_4$ as precursor; (c) the NH_4VO_3 as precursor; (d) the V_2O_5 as precursor; (e)the V_2O_5 as precursor and infused carbon oxides before reaction [67]. 37
2.16 Possible growth mechanism of sphere-like V_2O_3 nanoparticle [67]. 38

3.1 Schematic diagram of the entrained-flow reactor. 40
3.2 Schenck AccuRate volumetric feeder. 41
3.3 Design of feeder tube. 42
3.4 Drop tube furnace header with feeder tube. 43
3.5 Cascade impactor [68]. 44

3.6 Particle collecting mechanism of cascade impactor [68]. 44
3.7 Feed asphaltenes as received. 47
3.8 TG and DTG curves for asphaltene from 25 and 900 °C in N_2 atmosphere with a heating rate of 15 °C/min. 48

4.1 Presumed pathways for soot formation. 51
4.2 Soot on stages 1–6 of the cascade impactor. 53
4.3 SEM images of soot collected on different stages of the cascade impactor during pyrolysis at 1200 °C: (a) stage 11; b) magnified image of the circled portion in (a); (c) stage 3; (d) stage 8. . . 54
4.4 Particle size distribution of soot collected for different feed particle sizes. 56
4.5 SEM images (at same magnification) of soot collected for different feed particle sizes on stage 5 of the cascade impactor: (a) 53–106 μm; (b) 106–150 μm; (c) 150–212 μm. 57
4.6 (a) & (b) Morphology of the mixture of tar and soot collected at 800 °C (c) Morphology of dried soot separated from the tar mixture formed at 800 °C. 59
4.7 Soot yields at different pyrolysis temperatures. 60
4.8 SEM images of soot particles collected at (a) 800 °C, (b) 1000 °C, (c) 1200 °C, and (d) 1400 °C on stage 3 of the cascade impactor. All images are at the same magnification. 62
4.9 TEM images of the soot formed at 1400 °C. 63
4.10 EDX analysis of points marked in Figure 4.9. 64
4.11 Sulfur and hydrogen contents in soot formed at different temperatures. 65
4.12 FTIR spectrum of asphaltenes and soot collected at different temperatures. 66
4.13 Sulfur and hydrogen contents in soot formed at different resident times. 67
4.14 SEM images of soot particles formed at residence times of (a) 5 s, (b) 6.6 s, (c) 8.5 s, and (d) 12 s on stage 3 of the cascade impactor at 1200 °C. 68

5.1 Trace metals present in asphaltene analyzed using ICP-MS. . . 74

5.2 (a) Pyrolysis char fragmented at 1400 °C and (b and c) soot observed on the top surface of the char particle formed at 1000 °C. 76
5.3 Back-scattered image of the char from pyrolysis at 1400 °C. . 77
5.4 Back-scattered image of soot from pyrolysis at 1400 °C. 78
5.5 EDX elemental analysis: (a) char point 1 of Figure 5.3, (b) char point 2 of Figure 5.3, (c) char point 3 of Figure 5.3, and (d) soot entire area of Figure 5.4. 79
5.6 Trace metal content of soot formed during pyrolysis at 1000, 1200, and 1400 °C. 81
5.7 Trace metal content of char formed during pyrolysis at 1000, 1200, and 1400 °C. 81
5.8 Vanadium and nickel contents of soot and char formed during pyrolysis at 1000, 1200, and 1400 °C. 82
5.9 Mass balance of partial oxidation experiments. 86
5.10 Back-scattered SEM image. 88
5.11 TEM analysis of the soot from partial oxidation. 89
5.12 EDX analysis of areas 1 and 2 marked in Figure 5.11. 90
5.13 Back-scattered image of the partial oxidation soot ash. 90
5.14 EDX analysis of the partial oxidation soot points marked in Figure 5.13. 91
5.15 Back-scattered image of the partial oxidation char ash. 92
5.16 EDX analysis of the partial oxidation soot points marked in Figure 5.15. 92
5.17 Fouling deposit sample preparation procedure for SEM. 96
5.18 BSE and EDX mapping of first, second, third and fourth part of deposit (from left to right, leftmost being the tube material). 97
5.19 BSE image and EDX mapping of the cross-section of soot cake. 98
5.20 Soot particles and textures observed by TEM. 100
5.21 EDX map of area 1 of soot, TEM micrograph (DF = dark field image). 100
5.22 TEM Micrographs of soot cake. 101
5.23 Pathways for Ni and V during soot formation. 104

6.1 Numerical grid of the entrained-flow reactor and the magnified view of the inlet region. 108

6.2 Modeling methodology. 109
6.3 Schematic diagram of the model. 116
6.4 Velocity profile in the reactor. 117
6.5 Temperature profile in the reactor. 118
6.6 Soot mass fraction during pyrolysis along the axial length of the reactor. 119
6.7 Nucleation, coagulation and surface growth of soot during pyrolysis. 120
6.8 Comparison between experimental and modeling results on pyrolysis soot mass fraction. 121
6.9 Soot mass fraction during partial oxidation along the axial length of the reactor. 122
6.10 Nucleation, coagulation and surface growth of soot during partial oxidation. 123

A.1 Temperature calibration of the reactor. 141
A.2 Process flow diagram of the set up. 143

Chapter 1

Introduction

1.1 Canada's Oilsands

Global energy demand is expected to increase 56% between 2010 and 2040 as the economies in both developed and developing countries continue to grow and improve the standards of living [1]. A greater number of sources of energy will be needed to meet the growth in global demand. As conventional oil resources are declining, the need for maximum utilization of unconventional resources, like oil sands, will increase. Canada has the third largest oil reserves in the world and 97% of these reserves are in the oil sands. According to Canadian Association of Petroleum Producers (CAPP) report, Canada has 174 billion barrels of oil that can be recovered with existing technologies [2]. Oil sands generally contain a mixture of sand, water, clay and bitumen. Bitumen is a component of oil that is too thick to flow without being diluted with a diluent or heated to a sufficient temperature to reduce its viscosity [2].

Oil sands deposits of Canada are found in three important basins such as Athabasca, Peace River and Cold Lake in Alberta. The two important methods used for oil sands recovery are surface mining and drilling (in situ) which are based on the depth of the reserves. 20% of the oil sands deposits are close enough to the surface, that they can be mined using shovels and trucks. The remaining 80% of the deposits are at greater depths and are recovered using in situ technologies, which entails drilling wells [3]. Advanced technology is used

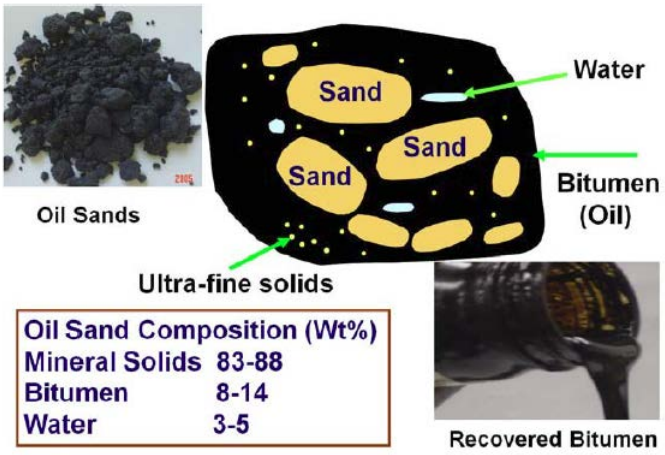

Figure 1.1: Characteristics of oil sands [5].

to inject steam or other sources of heat into the reservoir to heat the deposited bitumen so it can be pumped out to the surface through recovery wells. This technology is called steam assisted gravity drainage (SAGD) and natural gas is used for generating steam [4]. Bitumen production by SAGD is more energy intensive with lower recovery and greater greenhouse gas emissions as compared to open pit mining. But SAGD requires less water and minimal direct land disturbances, and has a lower capital cost per m^3 of bitumen production [4]. Also considering the large reserves available for bitumen production by in situ technology, it is important to find alternative energy sources other than natural gas for further exploration of oil sands.

Albertan bitumen from different sources has about 15 wt% of asphaltenes, the heaviest solubility class, which accounts for half of the Micro Carbon Residue (MCR) and most of the sulfur and mineral matter [6, 7]. The ore from Athabasca oil sands contains between 8 to 14% bitumen and the rest is coarse sands, fine silts and clays which are impregnated with bitumen as shown in Figure 1.1 [5]. Compared to conventional crude oil, crude bitumen has much lower hydrogen to carbon ratio, higher molecular weight distribution, greater specific gravity, and higher sulfur, nitrogen and metal content. Crude bitumen may be upgraded before it is refined to other petroleum products.

Bitumen upgrading occurs in two stages, primary upgrading and secondary upgrading. Primary upgrading is the initial process and achieves most of the value improvement for the feed. Secondary upgrading is a refining process that controls the quality and stabilizes the product [4]. In an upgrading process integrated with SAGD, carbon rejection is one of the preferred methods to increase the hydrogen to carbon ratio of the bitumen. The rejected carbon stream can be used as fuel for gasification and the product is syngas. Asphaltenes are formed during the primary upgrading process of bitumen as shown in Figure 1.2 [4]. The vacuum residuum from the distillation column is sent to the solvent de-asphalting unit where a paraffinic solvent is used to remove the high carbon content asphaltenes from the vacuum tower bottoms. These asphaltenes, about one-third of the vacuum residuum, are liquid at operating temperatures and are very problematic in bitumen upgrading facilities [8]. Asphaltenes are highly aromatic and normally contain substantial quantities of coke precursors, metals, sulfur, and nitrogen, thus handling asphaltenes is a real challenge for the oil sands industry. Considering factors such as an increase in world energy demand, large reserves of Canadian oil sands, improved upgrading technologies and an alternative to natural gas for SAGD operation, asphaltene gasification could be a great option to maximize its usability and reduce the waste product.

1.2 Gasification

Gasification is a reliable technology that can produce various products such as syngas for power generation, hydrogen and reformable liquid fuels and other valuable products as shown in Figure 1.3 [9]. The gasification process converts carbonaceous feedstock into synthesis gas that can be used for power generation and production of chemical feedstock [10]. Under high temperature and pressure conditions, carbonaceous materials in the feed react with oxygen, steam and CO_2, and produce H_2 and CO, while the minerals form a molten slag. The feedstock for gasification can be any carbonaceous fuel such

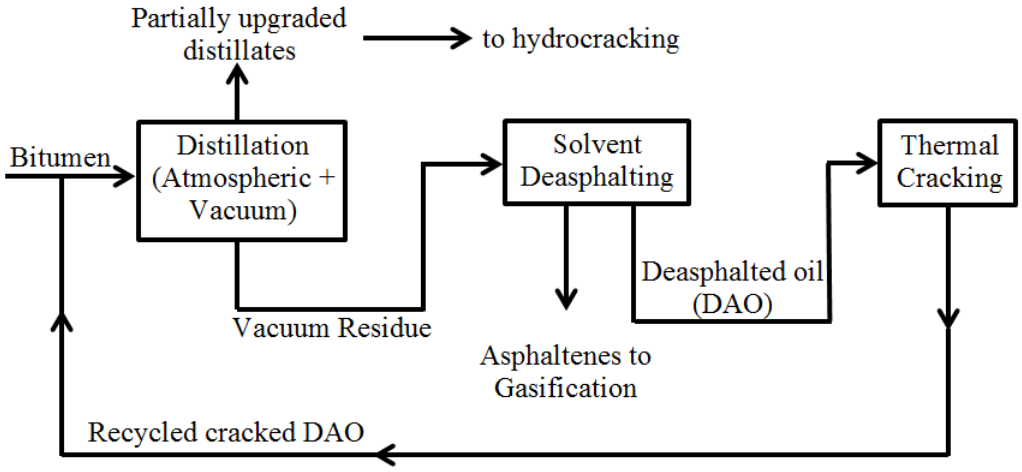

Figure 1.2: Primary upgrading of bitumen [4].

as coal, biomass, pet-coke or asphaltenes. The initial step of gasification is pyrolysis during which the fuel devolatilizes to form char and this char undergoes various heterogeneous reactions to form syngas. The whole process takes few seconds according to the residence time of the gasifier in use.

Nowadays, the increased demands for oil products necessitate taking deeper cuts in refining crude, leaving a high molecular weight residual high in vanadium, nickel and sulfur [11]. The increasing production of asphaltene has created an interest in using this by-product from a refining operation as a fuel for steam generators producing steam and electricity [8]. However, high content of sulfur (6–7 wt%) and the presence of high concentrations of hetero-atoms and metals in the asphaltene creates many problems for traditional utilization. Even though some portion of the asphaltene is used as an essential glue for paving road, most asphaltene is considered refinery waste, which makes it more attractive as a gasification feedstock. Understanding thermal behavior of a fuel is a preliminary step in evaluating various process alternatives such as fuel gasification or combustion.

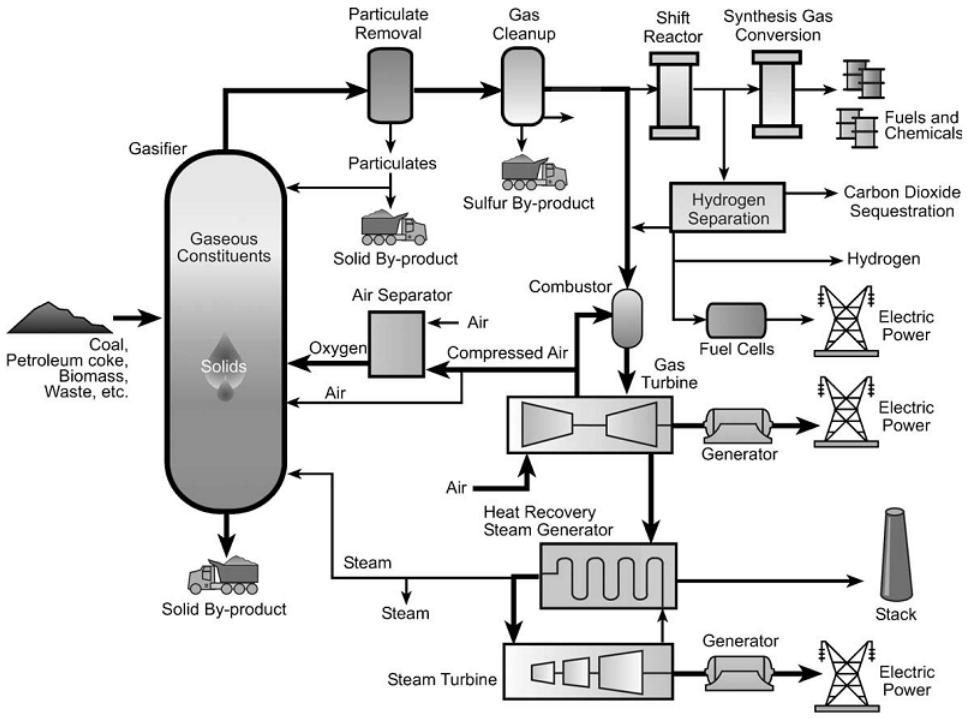

Figure 1.3: Gasification-based energy conversion options [9].

1.3 Soot

The term soot is given to the particulates formed during combustion of carbonaceous fuels under sub-stoichiometric conditions, either by design e.g. for the production of carbon black, or in poor mixing conditions. It is usually formed when the process conditions are sufficiently fuel rich as to allow condensation or polymerization reactions of the fuel (and its initial decomposition products) to compete with oxidation [12]. The formation of soot depends strongly on the fuel composition. It is the residual pyrolyzed fuel particles that may become airborne during pyrolysis. According to Neves et al., [13] polycyclic aromatic hydrocarbons (PAH) are products of primary pyrolysis and the pre-cursors of the soot particles in a secondary pyrolysis process.

Soot formation has been studied in many fossil fuel utilization processes such as pyrolysis, combustion, and gasification and is considered as one of the main pollutants. Soot is a highly undesirable byproduct formed in many

practical processes ranging from a burning candle to sophisticated combustors such as gas turbines, internal combustion engines or gasifiers. Soot particles exhausted by combustion devices present a significant environmental hazard when inhaled, as it often contains adsorbed polycyclic aromatic hydrocarbons (PAH)— an important class of higher hydrocarbons formed under fuel-rich conditions present in rich premixed and always in non-premixed flames. It is usually partially oxidized as well as combusted within the combustion chamber and may also appear in the flue gas, becoming an air pollutant. However, presence of soot in combustion flames is very important because it significantly enhances the radiative heat transfer with its large surface area [14, 15]. Ahluwalia and Im [16] observed that the soot particles significantly enhanced radiative heat transfer. The near-burner flame temperature could be lowered several hundred degrees due to the extra heat transfer to the surrounding walls due to the presence of soot particles in addition to gas, char and ash. The low temperature at the burner will decrease the thermal NO_x as well as fuel NO_x formation [17].

In addition to contributing to pollution, soot also enhances the emission of other pollutants like carbon monoxide. A study conducted at Stanford University reported that carbon dioxide was the number one cause of man-made global warming, accounting for 48% of the problem. Soot was second with 16% of the warming [18]. Soot causes greenhouse gas emissions only if released into air. Also, smaller soot particles are suspected to exhibit dangerous effects on human health as they penetrate easily into the respiratory tracts. Soot can act as a nucleus on which sulfates and heavy metal oxides condense and can adsorb some polycyclic aromatic hydrocarbons [19].

Soot contributes many serious problems in the industry and therefore, the guideline for the design and construction of power generating combustion devices is to avoid soot formation. Soot formation affects the carbon conversion efficiency because carbon is lost from the furnace without adding any value.

The metals present in the fuel liberates during the reactions inside the reactor either in the pure form or in mineral form. These metals/minerals may cause erosion/fouling in the downstream of the reactor. The erosion is due to the high velocity hitting of hard metal/mineral particle on the wall surfaces and the fouling is caused by the sticking of some of the minerals at certain temperatures. If the soot formed in the reactor encapsulates the metal/mineral liberated, the problems can be minimized. During gasification of asphaltene also, the metals present in asphaltene may be concentrated in gasifier soot and leave without creating any operational problems. If the metals are not encapsulated by soot, it may cause severe damage or fouling of the heat transfer tubes in the downstream of the gasification unit.

Since soot formation affects the operation and design of technical devices and has implications on both effective operation and pollutant emission, the formation of soot has become one of the major themes of research activities in the area of pyrolysis, combustion and gasification of hydrocarbon fuels. Therefore, understanding the characteristics of soot formed during pyrolysis and gasification of asphaltenes is fundamental in solving these problems and improving the efficiency of asphaltene gasification.

1.4 Objectives

The aim of this proposed research is to comprehensively understand the formation of soot during asphaltene pyrolysis and gasification in an entrained-flow reactor. On the other hand, the obtained soot will be characterized as a function of particle size distribution, chemical composition, and morphology. Also, a further objective is to investigate the interaction between the metals in asphaltene and soot formed. The fundamental knowledge gained from the above studies will help to understand the operational issues due to the influence of soot.

The research will focus on:

1. Investigate the properties of soot formed during pyrolysis and gasification of asphaltene in an entrained-flow reactor. The characterization of the soot includes particle size distribution, chemical composition, morphology and metal content.

   Specific attention is given to the:

   - Effect of feed particle size
   - Effect of operating temperature
   - Effect of reaction atmosphere (like pyrolysis and gasification)
   - Effect of residence time

2. Computational Fluid Dynamic Modeling of soot formation.

   A detailed model was developed in Ansys Fluent, taking into account of devolatilization and gasification of asphaltene particles in the entrained-flow reactor using Discrete Phase Modeling and Devolatilization models. Further, the simulation results are compared with the obtained experimental results.

1.5 Thesis Outline

The following description outlines each chapter in this thesis:

Chapter 1 is a general introduction on the problem and thesis objectives, along with the outline of the thesis.

Chapter 2 contains a literature review on soot formation. Several gasification techniques are reviewed, and particular focus is made to review the asphaltene behavior and its trace metal contents.

Chapter 3 contains the experimental details including the description of the entrained-flow reactor set up and properties of the feed asphaltene.

Chapter 4 investigates the properties of the soot formed during the pyrolysis of oil sands asphaltene in an entrained-flow reactor. The effect of operating parameters like feed particle size, pyrolysis temperature and residence time on the composition, morphology, and particle size distribution of the soot formed are analyzed in detail.

Chapter 5 explains the distribution of V, Ni, and other trace metals in soot and char collected from pyrolysis, partial oxidation, and steam gasification of asphaltene. The pyrolysis is done at different operating temperatures, partial oxidation is done at a fixed temperature for different stoichiometric ratios of oxygen, and steam gasification is done at a fixed temperature for different steam to fuel ratios. The soot-water, soot-cake and cooler fouling samples collected from an industrial asphaltene gasifier are analyzed to compare with the soot produced in the lab scale entrained-flow reactor.

Chapter 6 contains the soot formation modeling using Ansys Fluent. The feed asphaltene particles entering the reactor is modeled using discrete phase model and also devolatilization and soot formation models are incorporated into it. The simulation results are analyzed in detail to explain the effect of pyrolysis temperature and stoichiometric oxygen content on soot formation.

Chapter 7 contains the summary of the thesis, conclusions and recommendations for future work.

Chapter 2

Literature Review

2.1 Asphaltenes

The name 'asphaltene' was first used by J.B. Boussingault in 1837 when he observed that the distillation residue of crude oils had asphalt-like properties. Asphaltenes are insoluble in n-pentane (or n-heptane) and are soluble in toluene. The path of separation of asphaltene from petroleum residuum is shown in Figure 2.1. Asphaltenes are the heaviest and most polar molecular component of any carbonaceous material such as crude oil, bitumen or coal. Asphaltenes consist of carbon, hydrogen, nitrogen, oxygen, and sulfur and significant amounts of vanadium and nickel in addition to other trace metals. The H/C ratio is approximately 1: 1.1 to 1.2, depending upon the asphaltene source and the solvent used for extraction. Asphaltenes have a density between 1.1 and 1.2 g/mL [20].

Asphaltenes have been the subject of considerable discussion and controversy in the literature. Controversy and ambiguity arise largely because of the lack of chemical definition of asphaltene mixtures for which composition is dependent upon the source material and method of isolation. Asphaltenes are generally classified by the particular paraffin used to precipitate them from the benzene-soluble portion of the feed. Thus, there are pentane asphaltenes, hexane asphaltenes, heptane asphaltenes, and so on. However, the present tendency is to define the material precipitated by n-heptane as asphaltenes.

Table 2.1: Typical properties of asphaltenes from various origins [22]

	Fosterton	Neilburg	San Fernando	Orimulsion	Athabasca
Proximate Analysis (wt%)					
Volatile matter	23.9	61.5	78.89	58.18	61.72
Fixed carbon	75.1	38.1	19.89	12.84	37.88
Ash	0.88	0.39	0.53	0.18	0.4
Ultimate Analysis (wt%)					
C	55.4	82.6	81.1	84.28	80.3
H	5.2	7.8	8.62	10.33	8
N	0.5	1.1	1.01	0.64	1.2
S	1.7	6.5	4.29	3.95	8.2
O	37.2	2	4.39	0.55	2.5
H/C	1.1	1.1	1.3	1.5	1.2

The inter-relationship of polarity and molecular weight in terms of solubility behavior can be better understood. There is not a specific chemical composition or a specific molecular weight description for asphaltenes and it contain a wide distribution of polarities and molecular weights [21].

The classic definition of asphaltenes is based on the solution properties of petroleum residuum in various solvents. The asphaltene fraction of petroleum crude is defined according to Nellensteyn [23] as the fraction insoluble in low boiling point paraffin hydrocarbons but soluble in carbon tetrachloride and benzene. According to Pfeiffer [24], asphaltene is defined as the fraction insoluble in n-heptane but soluble in toluene. The asphaltenes from different

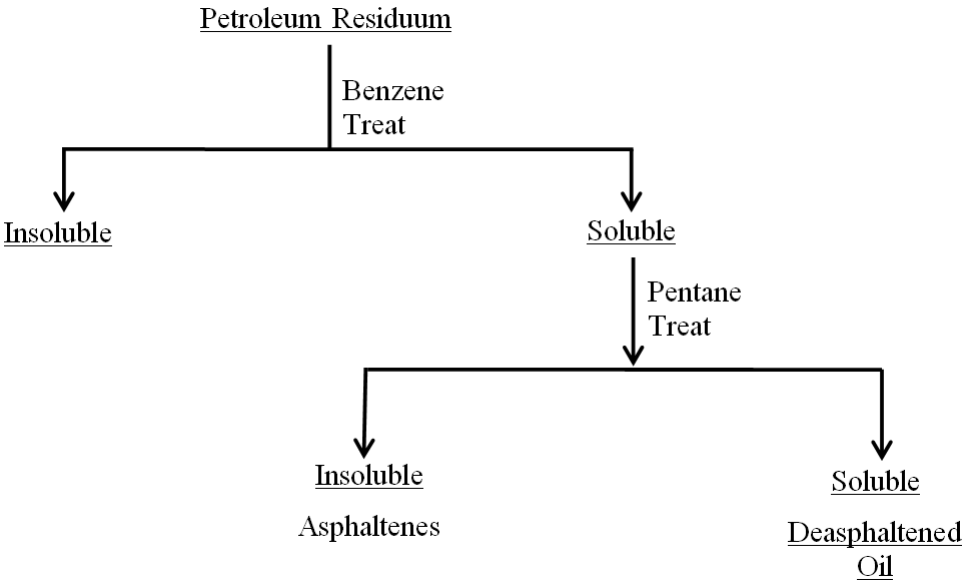

Figure 2.1: Separation of asphaltenes from petroleum residuum.

origins have specific properties. Table 2.1 shows the properties of asphaltenes from Fosterton and Neilburg in Saskatchewan, San Fernando in Columbia and Orimulsion in Venezuela. Asphaltenes generally contain very low ash (mostly less than one percent), but are high in volatile matter and fixed carbon. The sulfur content of the asphaltenes varies based on the origin of asphaltenes. The H/C ratio is around one due to it is being composed of mostly aromatic components.

Structure and molecular weight of asphaltenes has been a subject of debate among researchers [20, 26, 25, 27, 28, 29]. Two types of models have been proposed to describe the molecular architecture in asphaltenes: (i) archipelago models, and (ii) island models. The archipelago models consider that several aromatic clusters are bridged together via aliphatic chains, whereas island models suggest that there is predominantly one fused polycyclic aromatic hydrocarbon (PAH) ring system per asphaltene molecule with pendant aliphatic chains. Archipelago models are reported to fit observed experimental pyrolysis data more closely [7, 25]. Sheremata et al. [25] used Monte Carlo method to predict the structure of Athabasca asphaltenes and the molecular

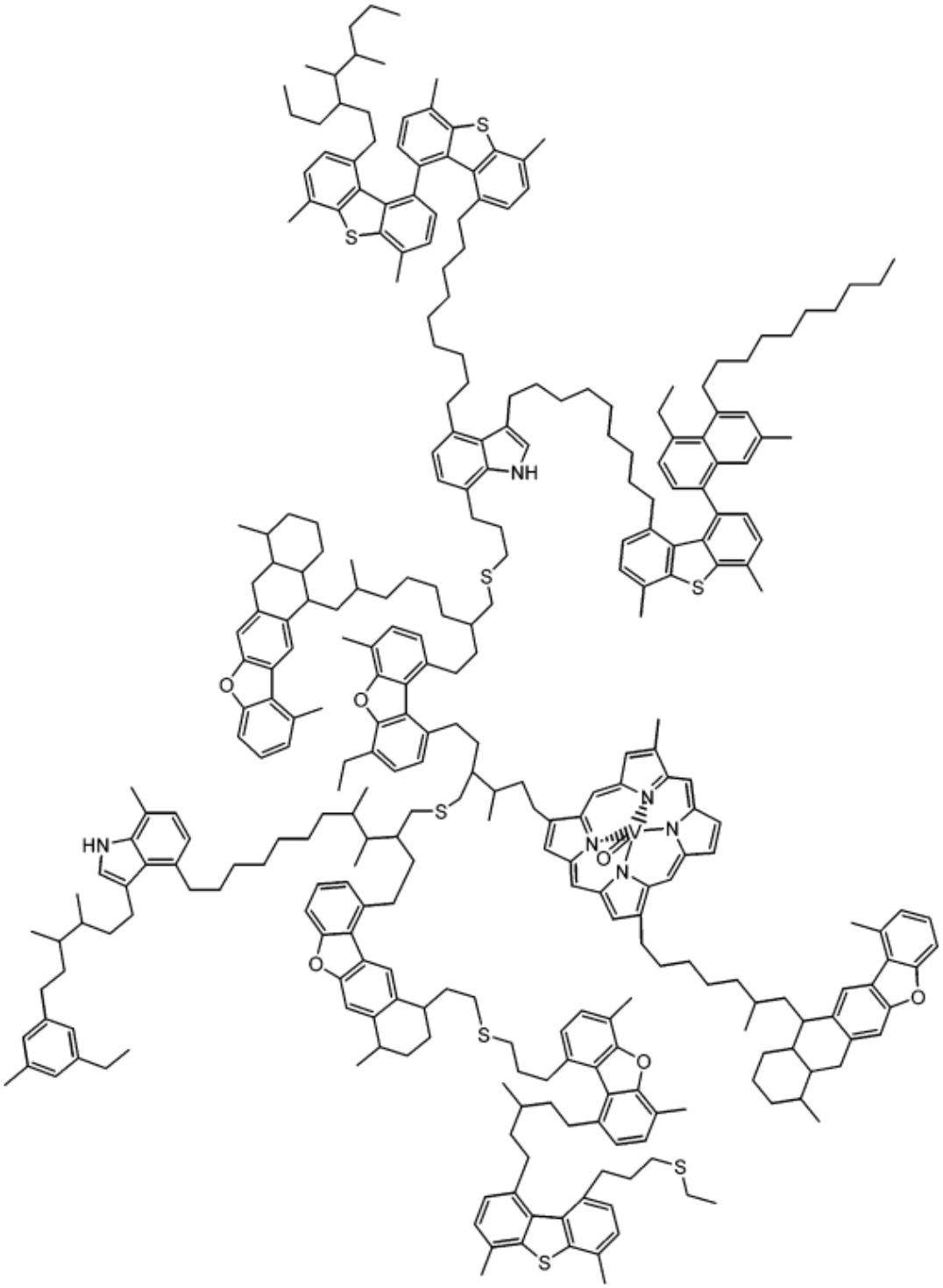

Figure 2.2: Structure of asphaltene molecule [25].

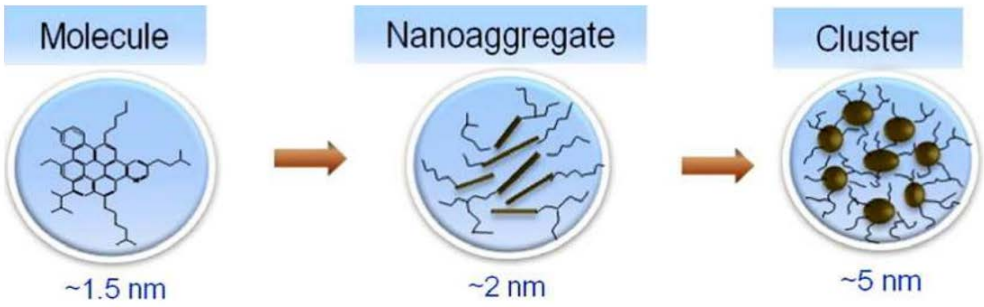

Figure 2.3: Modified Yen model for the asphaltene structure [30].

weight of asphaltene was determined by vapor pressure osmometry using o-dichlorobenzene as the solvent. They reported that asphaltene molecules are composed of different aromatic clusters linked to each other by aliphatic chains and sulfur side linkages. One of their molecular representation of asphaltene with molecular formula $C_{318}H_{395}N_6O_6S_8V$ and molecular weight 4705 g/mol is shown in Figure 2.2. This model was the first quantitative representation of archipelago model of asphaltenes.

Mullins et al. [30] proposed the modified Yen model for asphaltenes which consists of three primary components viz. asphaltene molecules, asphaltene nano-aggregates and clusters of asphaltene nano-aggregates. The island architecture exhibits attractive forces in the molecule interior and steric repulsion from alkane peripheral groups. The Yen model has been very useful, particularly for considering bulk properties of phase-separated asphaltenes. Nevertheless, at the time the Yen model was proposed, there were many uncertainties in asphaltene molecular weight, architecture, and colloidal structure. Figure 2.3 shows the schematic of the modified Yen model. The island architecture exhibits attractive forces in the molecule interior (PAH) and steric repulsion from alkane peripheral groups.

2.2 Gasification Theory

Gasification can be summarized into two major steps [31]:

1. Pyrolysis

   It is also called thermolysis. During pyrolysis organic substances are decomposed into solid residue (i.e., char) and volatiles when it is heated in the absence of oxygen.

$$\text{Organic matter} + \text{Heat} \longrightarrow \text{Char} + \text{Liquids} + \text{Gases} \tag{2.1}$$

2. Gasification

   The reaction between the char (from pyrolysis) and gasifying agents including oxygen, CO_2 or steam.

$$\text{Char} + \text{Gasifying agent} + \text{Heat} \longrightarrow \text{Gases} + \text{Ash} \tag{2.2}$$

Moreover, gasification reactions can be summarized into these parallel reactions:

(a) Partial oxidation and complete combustion with O_2

$$C + O_2 \longrightarrow CO_2 \, (\Delta H = -405.9\,\text{kJ/mol}) \tag{2.3}$$

$$C + \frac{1}{2}\,O_2 \longrightarrow CO \, (\Delta H = -123.1\,\text{kJ/mol}) \tag{2.4}$$

$$2\,H_2 + O_2 \longrightarrow 2\,H_2O \tag{2.5}$$

Partial oxidation and complete combustion with oxygen are exothermic reactions which provide required energy for proceeding gasification reactions by using much of the oxygen in the gasifier.

(b) Reaction of CO_2 with carbon (Boudouard's reaction)

$$C + CO_2 \rightleftharpoons 2\,CO \, (\Delta H = +159.7\,\text{kJ/mol}) \tag{2.6}$$

The reaction is endothermic and is much slower than combustion reaction at the same temperature in the absence of catalyst.

(c) Water gas reaction

$$H_2O + C \rightleftharpoons H_2 + CO \, (\Delta H = +118.9\,kJ/mol) \tag{2.7}$$

This endothermic reaction is favored by elevated temperature and reduced pressure, and in the absence of catalyst, occurs slowly at temperatures below 1200 K.

(d) Methanation reaction

$$C + 2\,H_2 \rightleftharpoons CH_4 \, (\Delta H = -87.4\,kJ/mol) \tag{2.8}$$

This reaction is very slow except at high pressures. The following gas phase reactions are important for the final gas quality to influence H_2/CO ratio. This ratio is important if the gas is for synthesis or hydrogen production.

(i) Water gas shift reaction

$$H_2O + CO \rightleftharpoons H_2 + CO_2 \, (\Delta H = -40.9\,kJ/mol) \tag{2.9}$$

(ii) Steam methane reforming reaction

$$CH_4 + H_2O \rightleftharpoons CO + 3\,H_2 \tag{2.10}$$

Gasification process can be performed in different reactors or gasifiers depending on operating condition and required situation obligated by fuel properties. Three main types of gasifiers that are available for commercial use are: fixed bed gasifier, fluidized bed gasifier and entrained-flow gasifier.

2.2.1 Fixed Bed Gasifier

The flow of fuel and the gasification agent in fixed bed is usually counter current as shown in Figure 2.4. Gases flow upward through a bed of feedstock

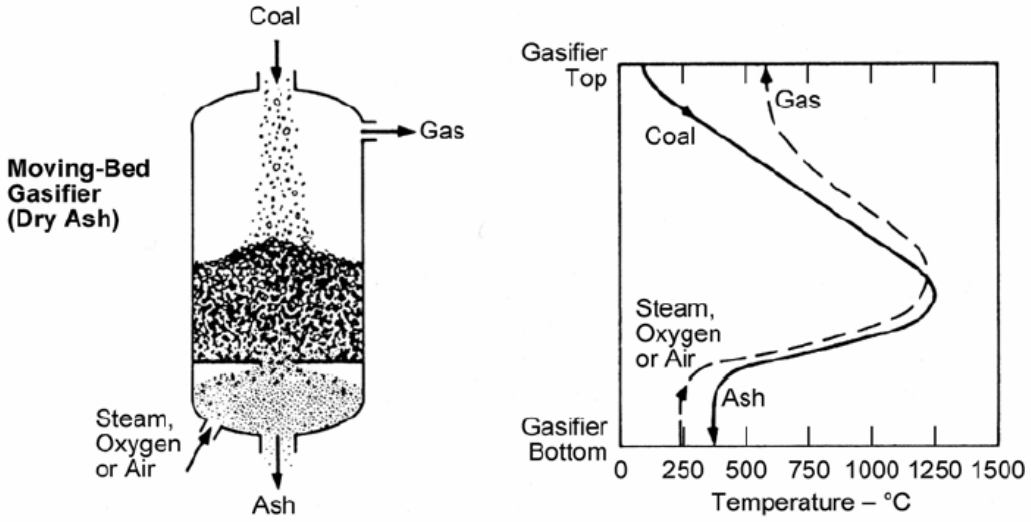

Figure 2.4: Fixed bed gasifier [31].

with the typical particle size of 5–80 mm. In this type of gasifier, the residence time is relatively long in range of 0.5–1 h which is suitable for large particles. This kind does not have the temperature limitation of fluidized bed, so they can operate at low temperature and produce just dry ash or operate at high temperature as a slagging gasifier. To maintain permeability of the fixed bed in slagging fixed bed, physical strength and coking behavior of coal particles are very important factors. They are principally used for the production of heat and also for small scale power generation [31].

2.2.2 Fluidized bed gasifier

In fluidized bed gasifier feedstock fuel particles usually with size of 0.5–5 mm are suspended in a bed of coal ash, sand and other material and the bed is fluidized by gas flow. A diagram of the fluidized bed gasifier is shown in Figure 2.5. This kind of gasifier operates at low temperature in the range of 600–1000 °C and the feedstock should be dry and crushed. Ash agglomeration in fluidized bed causes uneven bed fluidization so in order to avoid this matter the ash fusion temperature of fuel should be higher than operating temperature. They generally operate in the MWh range, and are generally of two types, i.e.,

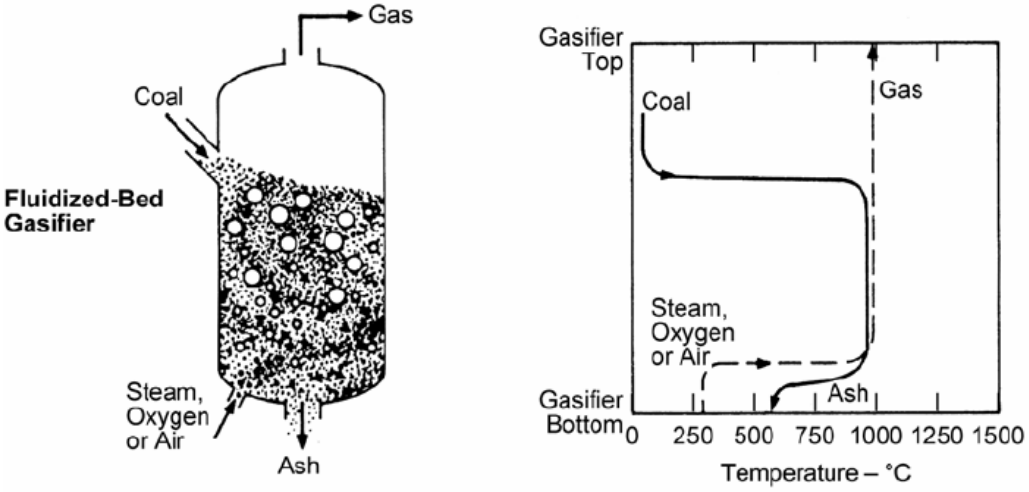

Figure 2.5: Fluidized bed gasifier [31].

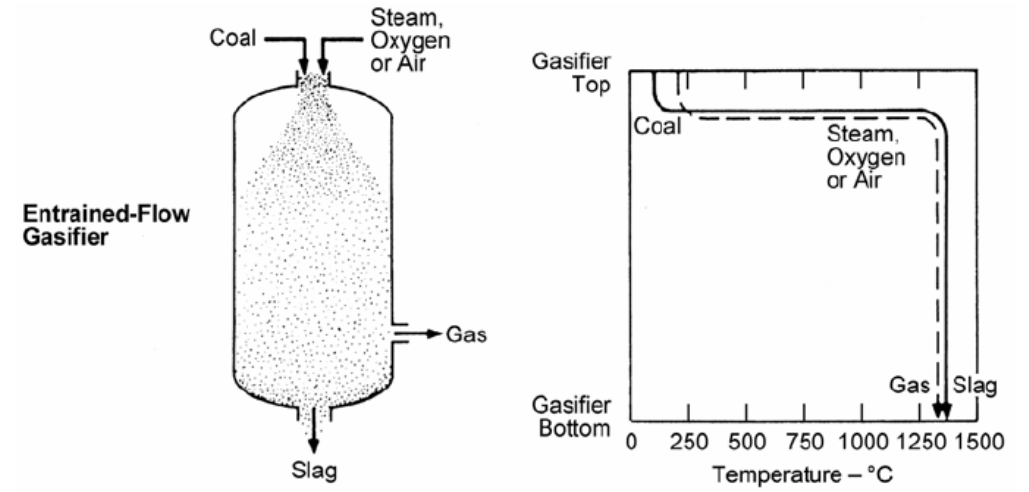

Figure 2.6: Entrained-flow gasifier [31].

bubbling fluidized bed (BFB) gasifiers and circulating fluidized bed (CFB) gasifiers [31].

2.2.3 Entrained flow gasifier

Fuel particles and gases flow concurrently from top to bottom in entrained-flow gasifier as shown in Figure 2.6. Therefore due to this kind of flow configuration the residence time of fuel particles is very short in the gasification zone (usually in the range of 5–10 s). Consequently due to this short residence time in entrained-flow gasifier to have high carbon conversion, the fuel should be pulverized and the system should be designed to operate at high temperatures. Due to intense reaction condition inside of this kind of gasifiers, entrained-flow gasifiers are capable of working with high throughput and can use a wide range of less reactive coals. Entrained-flow gasifier are also capable of working with dry or slurry feed depending on their design; however, dry-fed gasifier is more coal efficient and less oxygen consuming in comparison with slurry-fed, because slurry-fed system requires additional energy to evaporate water in slurry. These are generally larger units for power generation and operate at very high temperatures, in excess of 1200 °C and for very short residence times. They are normally fired with fossil fuels [31]. Generic characteristics of entrained flow gasifiers include:

- High-temperature slagging operation
- Entrainment of some molten slag in the raw syngas
- Relatively large oxidant requirements
- Large amount of sensible heat in the raw syngas
- Ability to gasify all coal regardless of rank, caking characteristics or amount of fines

Many IGCC plants utilize entrained-bed gasifiers. Entrained-bed gasifiers are available in much larger capacities (100 MWe) than other types, and these are

more commonly used for fossil fuels like coal, refinery wastes, etc. Entrained-flow gasification is applied in this study.

2.3 Asphaltene / Heavy oil Gasification

Very limited information is available for asphaltene or heavy oil gasification. Ashizawa et al. [32] investigated the gasification characteristics of extra heavy oil in a research-scale gasifier with a capacity of 2.4 tons/day. The feedstock for this study was Orimulsion, which is a bitumen-based fuel constituted by 70% bitumen and 30% water. The set up consisted of a pressurized (1.9 MPa) entrained flow type gasifier, a raw-gas cooler and, 15 m^3 feedstock storage tank along with a supply system. The gasifying agent used was oxygen with an oxygen ratio of 0.37 to 0.41. They found that increasing the oxygen ratio leads to increase of carbon conversion while it reduces the cold gas efficiency (CGE) and caloric value of products. The higher heating value (HHV) wet values were in the range of 9.5–10.5 MJ/m^3 and CGE was about 75–80% and carbon conversion was more than 97%. They collected char and gas samples at different levels of the gasifier and found that high carbon conversion efficiency was obtained at top 1/3 of the reactor. Also, gas analyses revealed that CH_4, H_2O and CO concentrations decreased along the gasifier while H_2 and CO_2 concentrations increased.

Moreno et al. [34] investigated gasification of Colombian asphaltenes from San Fernando crude oil with oxygen in a laboratory scale batch process. The objective of their work was to find the effect of temperature and gasifying agent flow rate on syngas composition. The asphaltene sample was placed in a horizontal tubular oven and heated up to 1000 °C. The continuous flow of O_2 diluted with argon at 170 psi (11.6 atm) was supplied as the gasifying agent. The temperature of the gasification experiments were varied in the range of 900 to 1000 °C. Their results indicated that increasing the temperature improved the syngas composition (i.e., CO and H_2 content) and carbon conversion be-

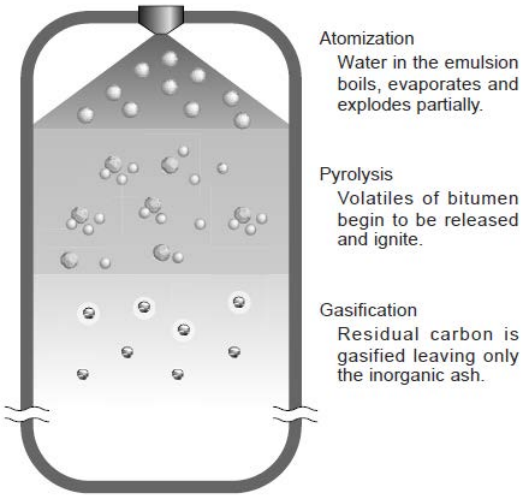

Figure 2.7: Heterogeneous phase reaction model [33].

cause of gasification at higher temperatures decreases the amount of tar and other by-products. They varied the gasifying agent from 33% to 47% (of the amount of oxygen required for complete combustion) and it was established that the best results in terms of CO and H_2 content is obtained at 40% of stoichiometric oxygen.

Watanabe et al. [33] developed a numerical model for the design and performance evaluation of the extra heavy oil gasification in an entrained-flow gasifier. Four reaction processes like atomization, pyrolysis, coke gasification and gaseous phase reaction were modeled. Heterogeneous phase reaction concept of this model is shown in Figure 2.7. The particle transport is modeled with Lagrangian particle tracking approach. Comparison between the computational results and the experimental results on research gasifier for liquid fuel shows that temperature distribution, the gas composition distribution, the heating value and the carbon conversion efficiency are matches well.

Chhiti et al. [35] experimentally investigated the gasification of bio-oil in a lab scale high temperature entrained flow reactor over a temperature range from 1000 to 1400 °C. They found that hydrogen yield increases with temper-

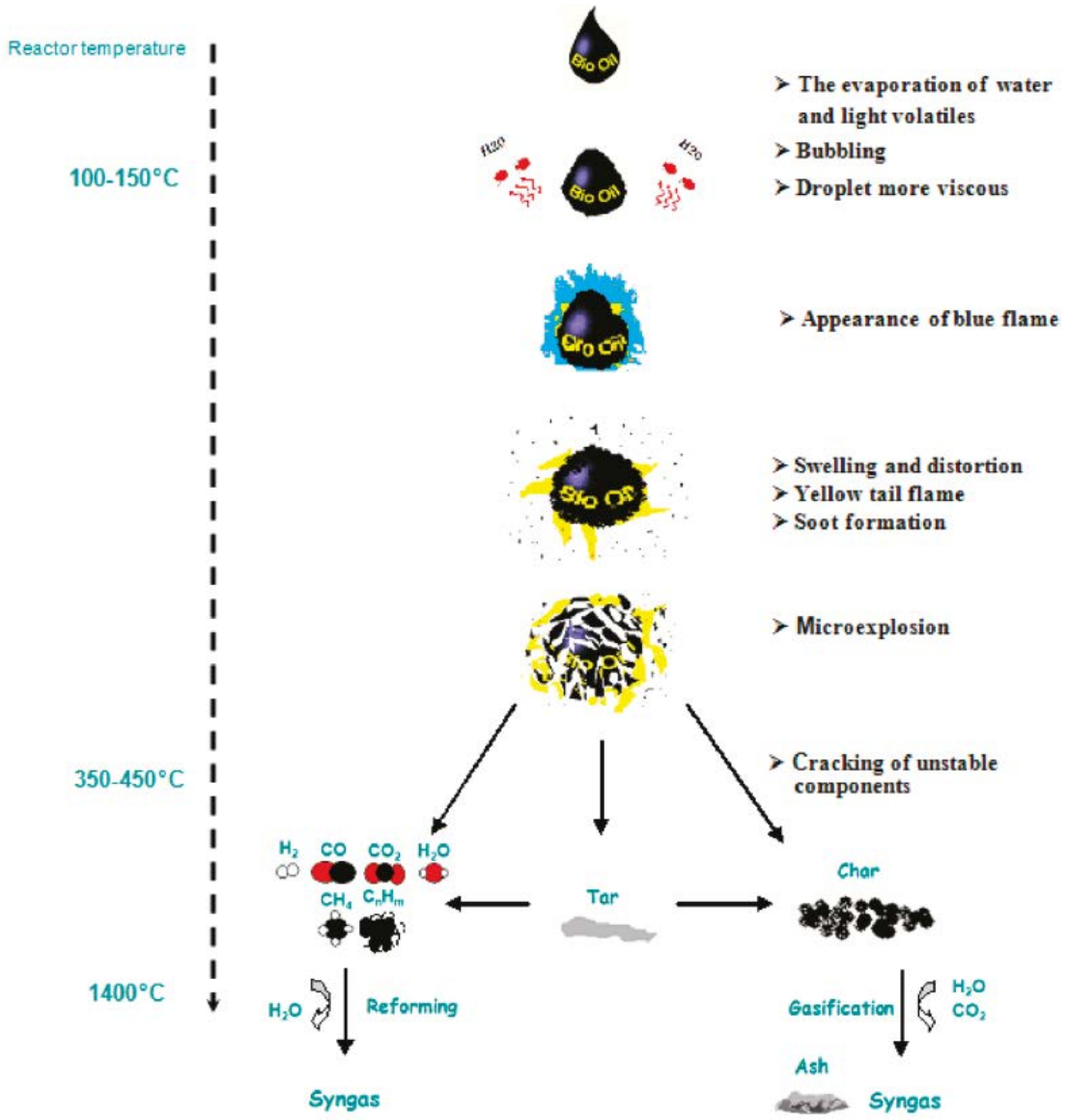

Figure 2.8: Schematic representation of single bio-oil droplet gasification [35].

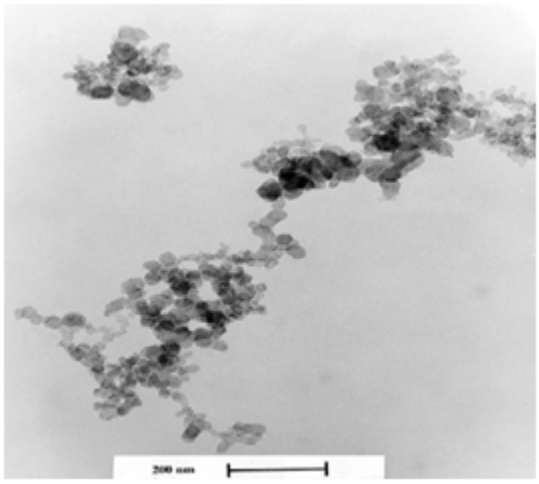

Figure 2.9: Micrograph of diesel soot [36].

ature by steam reforming of CH_4 and C_2H_2 and with water gas shift reaction. The influence of ash on the gasification process has found to cause a decrease in the total amount of gas produced. A schematic representation of air/steam gasification of single droplet of bio-oil is proposed in Figure 2.8. Upon entering the reactor, the moisture and light volatiles evaporate from the fuel droplet. A blue flame may be observed due to the combustion of the light volatiles. Swelling and distortion of the spherical particle will take place followed by micro explosion to produce char, tar and light gases. The char undergoes gasification reactions to form syngas and the light gas reforms to give syngas. The tar undergoes cracking or gasification to end up with syngas.

2.4 Soot Formation

Soot exists in the form of both individual particles and agglomerates comprised of several primary particles. The nature of soot varies with aging. The fundamental units of soot agglomerates are the spherules [36]. Spherule diameter varies from 10–50 nm. Soot size increases, mainly by agglomeration, from a few nanometers up to 200 nm particle diameter. During this process the free radical character of the soot decreases. The concentration of soot particles in post-flame gases remains typically in the range 10^6–10^9 cm^{-3}. The soot

hydrogen content is about 1% by weight and the soot density is about 1.8–2 g/cm^3 [37]. Figure 2.9 shows the shape of soot particle consisting of clusters (about 4000 spherules) or chains of spherules [36].

Significant progress has been made in the past decade on the detailed reaction kinetics of aromatics formation, growth, and oxidation in hydrocarbon combustion in different experimental devices, such as flames, shock wave reactors, and flow reactors [38, 39, 40]. Soot (mean diameters around 20–30 nm) [14] has been understood to form in many hydrocarbon flames principally from the combination and condensation of acetylene, benzene, or other aromatic hydrocarbons [14, 41, 42]. It is widely observed that soot is produced in high temperature processes (1000–2500 °C) [41] with fuel rich atmospheres, such as pyrolysis and gasification. Its formation at high temperatures is usually accompanied or preceded by the formation of unsaturated hydrocarbons, especially acetylenes and condensed unsaturated ring systems, PAHs which are thermodynamically relatively stable. It has been observed that increasing the reaction temperature favors soot formation. However, at higher temperature, soot or its precursors probably have higher gasification reactivity. As a result of the competition between soot formation and destruction, its yield starts to drop down after reaching a peak value [42, 43, 44].

There are differences that exist in the formation and properties between coal-derived soot and the soot from conventional hydrocarbon flames. The theory regarding soot formation from coal is available in the literature. Pyrolysis is the initial reaction step that occurs in a coal particle. Primary pyrolysis products include light gases, char, and tar, which is a gas mixture of heavy-molecular-weight hydrocarbons at high temperatures and condensable at room temperature. Simultaneously, the volatile matter released in the gas phase may also undergo secondary reactions. Soot is believed to be one of the products of these secondary reactions (Figure 2.10) [45]. During coal pyrolysis, it is considered that coal tar does not break down to C_2H_2 and reform

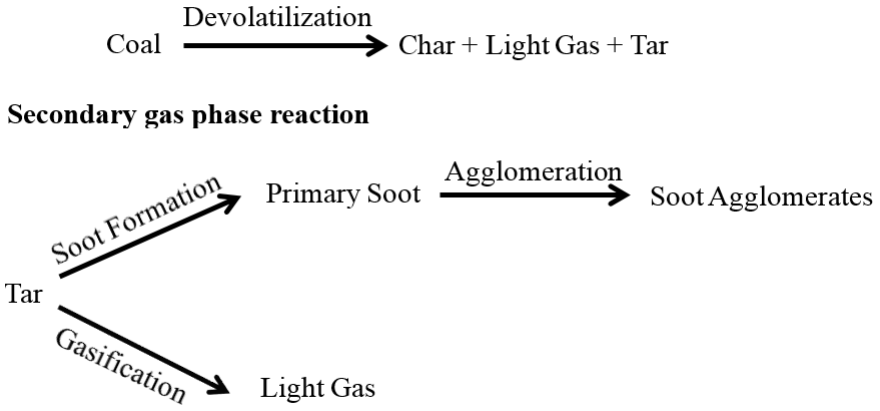

Figure 2.10: Secondary pyrolysis processes and products [45].

an aromatic ring. Tar is the primary precursor of soot. The tar from primary pyrolysis consists of many PAHs. These hydrocarbon molecules are very likely to undergo both cracking and polymerization processes at high temperature. The mixing of different hydrocarbon may also promote soot formation. The hetero-aromatic compounds containing O, S, and N are found in coal tar, but not in most ordinary hydrocarbon fuels. They are probably also involved in the soot formation mechanism according to Ma [45].

Ma [45] used a flat-flame laminar flow reactor and simulated the temperature and gas-phase environment in the flame region of an industrial furnace to determine the properties of coal-derived soot, soot formation chemistry, and product and element distributions of pyrolysis of coals. Coal particles were pyrolyzed in the post-flame zone of a CH_4/H_2/air flat-flame operated under fuel rich conditions with almost no oxygen existing in the post-flame region. A thermophoretic technique was applied to extract soot and other aerosol deposits from the soot cloud. The sampling method yielded high quality images of deposits using the transmission electron microscopy (TEM), which allowed a detailed examination of soot particle morphology as a function of particle residence time. TEM is an optical analysis technique with resolutions that

are orders of magnitude higher than in SEM. Similar to SEM, a beam of electrons passes through an ultra-thin sample of few hundred nm thickness to create interactions between the electron beam and sample atoms. Based on TEM micrographs, soot was found to exist in both distinct single particles and agglomerates. The primary soot particle diameter was in the range of 25–60 nm. Total soot yield was related to temperature and coal rank. Residence time showed little effect on total soot yield in this study because soot formation was very fast at the high temperature conditions examined. High soot formation rates in the temperature range from 1650 K to 1900 K suggest that mixing-limited turbulent reactions may be applicable to turbulent systems. Ma [45] concluded that soot formation in coal combustion proceeds by a different mechanism than reported for simple hydrocarbon fuels.

Kozinski and Saade [43] studied the effect of combustion of three different kinds of biomass, namely paper-mill residue, hard pine-wood, and particle board on soot aggregates and PAHs formation. Conditions similar to those in typical residential space heating systems used to burn wood have been simulated in a laboratory furnace. Soot was collected using a Fisher fiberglass filter system. It has been found that the effect of temperature/heat input and oxygen/local mixing conditions appear to be important for the preparticle chemistry, responsible for the formation of incipient soot particles, and the soot surface-mass growth. The experiments have shown that the temperature-time history and C/O ratio are important parameters affecting PAHs formation/destruction in biomass combustion. The higher the temperature, the higher the soot mass concentration and the smaller the soot particles/aggregates. It is possible that the higher combustion temperature and thermal input influenced the conversion kinetics of gas precursors forming soot. Higher temperatures might also have increased the sooting tendency by increasing the rate of elementary chemi-ionization reactions and intensifying biomass pyrolysis.

Wijayanta et al. [46, 47] investigated numerically the primary reactions of coal volatiles for soot formation mechanism under pyrolysis (thermal decomposition), partial oxidation (O_2 gasification) and O_2/CO_2 gasification conditions for coal as well as biomass fuels. They reported a detailed soot formation reaction mechanism involving 276 species, 2158 conventional gas phase reactions and 1635 surface phase reactions. The composition of biomass volatiles produced from pine saw-dust pyrolysis was used to analyze the combustion products, including PAHs. A plug flow reactor model for reactions of biomass volatiles was assumed. The reaction temperature and pressure varied was in the range of 1073–1873 K and 0.1–2 MPa. They found that production of PAHs increases with increasing the temperature (1073–1473 K) and decreases at higher temperatures (1678–1873 K). The effect of temperature on product concentration was more emphasized than that of pressure. O_2 concentration was important in reducing PAHs at low temperatures. Below 1473 K, an increase in the O_2 concentration decreased PAH and soot production. High level of CO_2 at the inlet has a significant effect on PAH reduction at high temperatures (>1473 K). At low temperatures, the O_2 input becomes important in reducing PAHs. They also mentioned that use of air eliminates the PAHs, but cannot produce syngas efficiently.

Although entrained flow gasifiers usually operate at high temperature (>1200 °C) to produce a syngas with low or no tar content, soot produced at higher temperature is another serious issue, especially for biomass because of its high volatile content. There is limited literature considering soot formation in biomass entrained flow gasification. Qin et al. [44] investigated biomass gasification of wood and straw in a laboratory scale atmospheric pressure entrained flow reactor (5 kW) with an objective to elucidate the effects of operating conditions, such as reaction temperature, steam/carbon molar ratio, excess air ratio, and biomass type on the product yield (soot, tar, and $H_2/CO/CO_2$/hydrocarbons). A cyclone with a cut size of 2.5 μm was used to collect the char, and a metal filter was used to capture soot. They observed

that biomass was completely converted at all investigated operating conditions and the syngas contained nearly no tar but some soot at the highest applied reaction temperature of 1350 °C and concluded that higher temperature was beneficial to lower the amount of tar while the soot yield showed a peak of 56.7 g/kg fuel at 1200 °C. It is assumed that higher temperature favors soot formation. However, due to higher gasification reactivity of soot or its precursors (i.e., as a result of the competition between soot formation and destruction) at higher temperature, soot yield starts to drop down after reaching a peak value at 1200 °C. They also observed the similar trend for the gasification experiments without steam addition at higher temperature (1200–1350 °C). Moreover, steam addition gave an obvious reduction in the soot yield, but it was not possible to completely avoid soot.

Although soot formation and its importance in coal combustion, pyrolysis and gasification have been known for a long time, extensive characterization of coal-derived soot has not been performed. Chen [48] performed coal pyrolysis experiments in an inductively heated radiant drop-tube furnace (DTF) in an inert atmosphere over the temperature range from 1480 to 1740 K. He found that the yields of tar/oil plus soot in the secondary pyrolysis experiments were constant and were equal to the tar plus oil yields obtained at the longest residence time in primary pyrolysis experiments. For a highly volatile bituminous coal at higher temperatures, more than 25% of the coal mass (dry ash free mass) was converted to soot. The effect of O/C ratio on soot formation in partial gasification of biomass and coal was investigated by Chen et al. [49] in a laboratory-scale atmospheric fluidized bed using air and steam as the gasification medium. They observed that the concentration of soot decreases by increasing the O/C ratio.

Nenniger [50] also observed similar results during the pyrolysis of coal in an argon atmosphere in an electrically heated DTF from 1300 to 2200 K. The high soot yields reported by these researchers were probably due to the inert

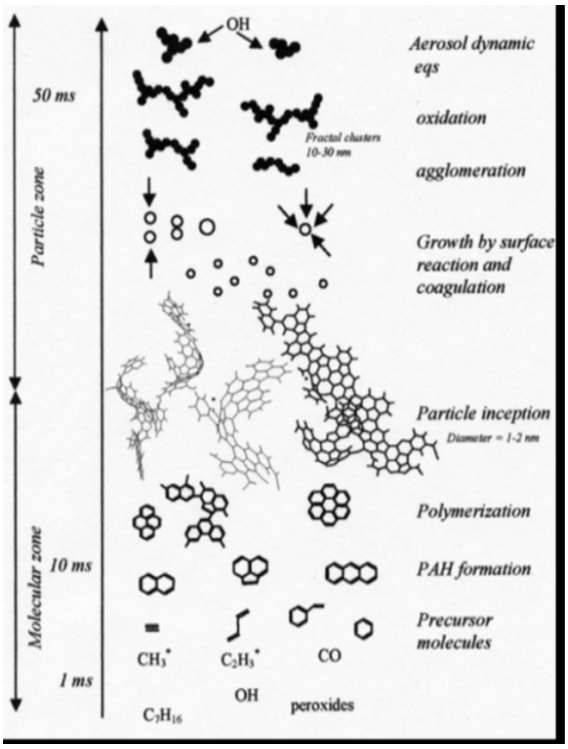

Figure 2.11: Scheme of soot formation process [52].

conditions, since no destruction of aromatic compounds by oxygen-containing species occurred. The profiles of soot yield versus temperature in these coal pyrolysis experiments were not bell-shaped; the soot yields monotonically increased with temperature. Shurupov [51] concluded that the pyrolysis temperature, reactant residence time and the feeding concentration of the fuel are the main parameters that govern soot formation during pyrolysis of any fuel. The induction periods of nucleation of the soot particles for different hydrocarbons may be different.

2.5 Mechanism of Soot Formation

Soot formation is a complex process, which involves many chemical and physical steps as shown in Figure 2.11 [52]. The soot particles from various sources, i.e., from different fuels and combustion conditions tend to be similar in size and composition, which indicate that the same formation processes and growth

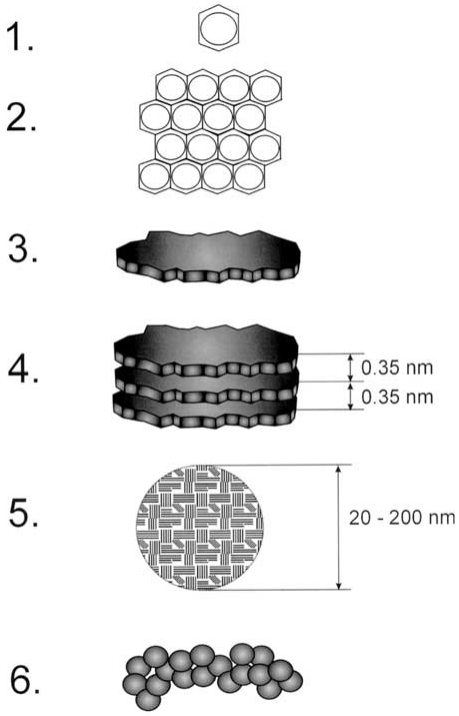

Figure 2.12: Diesel soot formation mechanism [19].

constraints apply but because of its complexity, a number of uncertainties still remain. While significant progress has been made in relation to the determination of its physico-chemical characteristics, significant uncertainty still exists concerning the formation, growth, and conversion under different conditions. In particular, the formation of soot indicates a number of complex physico-chemical processes that are not well-known at present.

The soot formation mechanism shown in Figure 2.12 [19] is divided into six steps. In the first step, the fuel is reformed into aromatic compounds. These aromatic compounds react together in step 2 to form polyaromatic substances: the carbon to hydrogen ratio increases further. These polyaromatic compounds form a flat micro-cells in which hydrogen is almost absent. Therefore, such carbon flat structures bond themselves in a graphite like lattice. These microstructures are then stacked onto one another to generate an elemental soot particle of size 20–200 nm. In these particles some polyaromatic compounds

are still present and the van der Waals forces, beyond the hydrogen bonds, can lead to particle agglomeration to become a chain-like structure.

The most accepted theory for soot formation is well described by Haynes and Wagner [52] in which the pyrolysis of hydrocarbons produces smaller hydrocarbons, acetylene in particular. The initial step is the formation of the first aromatic species from the aliphatic hydrocarbons, followed by the addition of other aromatic and alkyl species to give higher species, i.e. PAHs. The continued growth of these PAHs results into the generation of the smallest soot particles with diameters of the order of 1 nm and a mass of around 500–2000 amu. It is believed to follow the H-abstraction-C_2H_2-addition (HACA) route [41].

The major challenge of studying soot is that it forms in very short time scales (in the order of milliseconds) and in this time period most of the mass growth takes place forming particles of 1 to 10 nm size range. It is assumed that PAHs are important precursors in soot formation. Soot formation is approximated by four stages as follows [52], [53]:

1. Nucleation of soot particle (inception and growth of PAHs)
   Nucleation is the first step in which first soot particle is formed from pyrolysis products. Such products typically include different unsaturated hydrocarbons, particularly acetylene and its analogues, PAHs, and ionic species. These species have been often considered as the most likely precursor of soot in flames and have important role in the soot particle inception. The molecular fragments form closed ring aromatic species by HACA mechanism proposed by Frenklach [41] or propargyl recombination reactions proposed by Miller and Melius [54].

2. Particle coagulation
   Once soot particles are formed, the nascent soot particles collide and coalesce with each other forming larger new particles. Experimental studies

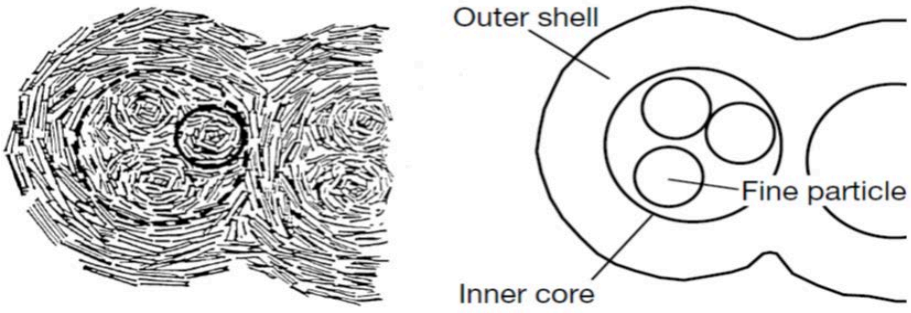

Figure 2.13: Coagulation of soot particles [55].

observed that initially the particles look spherical and later acquire a fractal shape. At low pressures the coagulation is said to be in the free-molecular regime, and at high pressures in the continuum regime ($d_p >$ 200 nm).

3. Particle surface reactions (Growth and surface oxidation)

   The carbon mass accumulated in soot is determined primarily by surface reactions—growth and oxidation. Acetylene is the principal gaseous species that reacts at the particle surface (based on experimental studies of laminar premixed flames). This carbon deposition process follows first-order kinetics. Species other than acetylene as possible surface growth precursors are aromatics. Counterbalancing the surface growth is the oxidation of soot particles, which occurs predominantly by O atom, OH radicals and O_2 molecules.

4. Particle agglomeration

   Soot agglomeration is taking place in the late phase of soot formation when, due to lack of surface growth, coagulation is no longer possible and when soot particles 'mature' (or 'age'). At some point, soot particles are observed to agglomerate, i.e., stick to each other forming chain-like structures, containing 30–1800 spherules. The chain-like structure has been analyzed in terms of fractal geometry.

Particle inception is a gas phase homogeneous process occurring at a spe-

cific molecular weight above which a PAH is interpreted as solid particles than molecules [55]. The initial soot particles are almost spherical in shape and have a C/H ratio of roughly 2. Particle inception or growth of PAH is delayed by an induction time which is specific for different hydrocarbons. During induction time PAH is transformed to particles of soot. Once a PAH monomer attains a certain size, it will collide with another PAH monomer and form PAH dimers. Subsequently the dimers stick to each other and form tetramers and finally the PAH clusters evolve into a solid soot particle [56]. Coagulation takes place when two relatively small particles stick together by a common outer shell generated by deposition as shown in Figure 2.13 [55]. The rate of sticking depends upon the rate of collision of particles. Most of the soot particles are formed by surface growth than particle inception and is similar to the PAH formation [55]. Surface growth is a heterogeneous process where adsorption and desorption reactions take place. Particle agglomeration takes place in the last phase of soot formation when coagulation is no longer possible [55]. As a result, aggregates containing 10 to 100 primary particles form long open structure with a log-normal size distribution.

2.6 Metals in Asphaltene

Considerable amount of literature on low heating rate pyrolysis and coking behaviour of asphaltenes exist [57, 58, 59, 60]. However, very limited work has been reported on pyrolysis and gasification of asphaltenes at entrained flow gasification conditions. The slag or ash chemistry of coal and biomass gasification also studied in detail. But ash composition of coal and biomass is generally Ca, Fe, Si, Al, K, Na, and Mg while asphaltene ash is mainly composed of vanadium and nickel. The large difference that exists between the ash compositions of these fuels may lead to unpredictable slagging problems in the conventional coal-fired gasifiers, because the transformation of V and Ni are quite different from the general ash composition at high temperatures. Table 2.2 [61] shows the principal ash-forming elements in fuel oil. The inorganic type

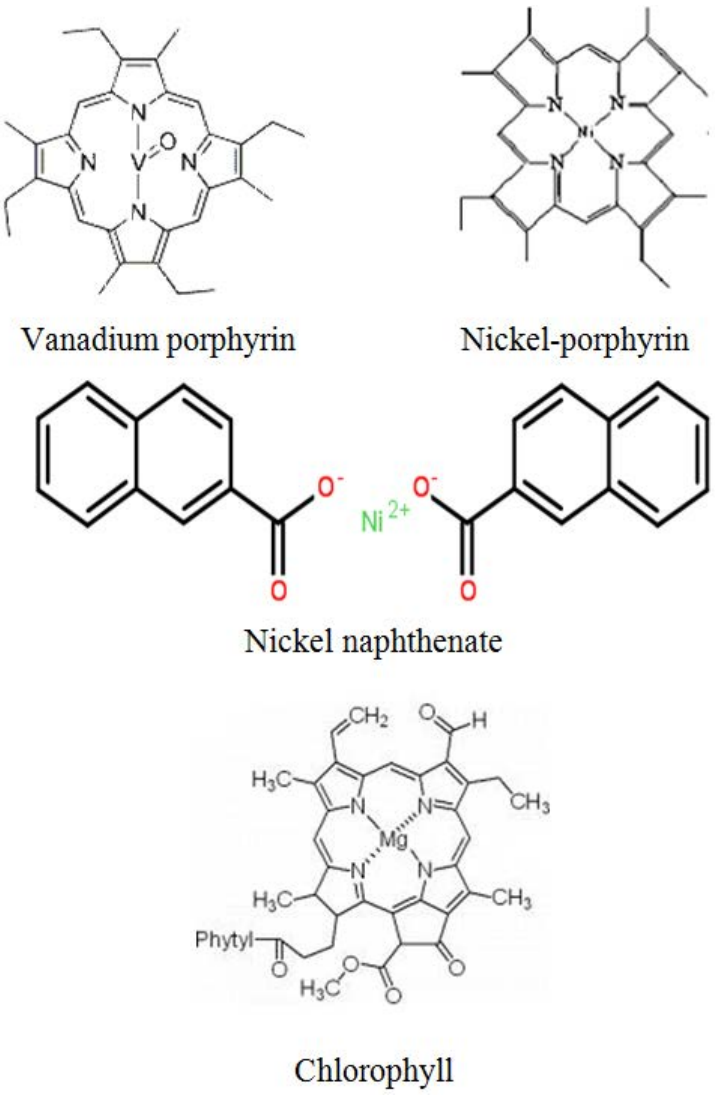

Figure 2.14: Main existence forms of vanadium and nickel in asphaltene. [61].

of elements present in the fuel can be readily eliminated during the refining process, while the organic type can be hardly removed which results in high concentration in the final product of asphaltene.

The main existence forms of vanadium and nickel in asphaltene are shown in Figure 2.14 [61]. These forms of organic minerals have the similar structure like chlorophyll. Vanadium exhibits triple valences V^{3+}, V^{4+}, and V^{5+} at different atmospheres at high temperatures [62]. V_2O_3 is stable under reducing

Table 2.2: Element type and chemical form in fuel oil [61]

Element	Type	Solubility in Oil	Probable chemical form
Aluminum	Inorganic	Insoluble	Complex aluminosilicates in suspension
Calcium	Organic	Soluble	Not identified
	Inorganic	Insoluble	Calcium minerals in suspension, calcium salts in suspension or dissolved in emulsified water
Iron	Organic	Soluble	Possible iron porphyrin complexes
	Inorganic	Insoluble	Finely sized iron oxides in suspension
Magnesium	Organic	Soluble	Not identified
	Inorganic	Insoluble	Magnesium salts dissolved in emulsified water or in suspension in microcrystalline state
Nickel	Organic	Soluble	Probably porphyrin complexes
Silicon	Inorganic	Insoluble	Complex silicates and sand in suspension
Sodium	Inorganic	Insoluble	Largely sodium chloride dissolved in emulsified water or in suspension in microcrystalline state
Vanadium	Organic	Soluble	Vanadium porphyrin complexes
Zinc	Organic	Soluble	Not identified

atmosphere, and transforms to V_2O_5 in oxidizing atmosphere. Meanwhile, Ni exists in a wide range of oxidation states as Ni, Ni^{2+}, and Ni^{3+} in high temperature range. The fate of V and Ni in the thermal conversion calculation of coal was investigated by Frandsen et al. [63]. In standard reducing conditions ($\lambda = 0.6$), solid V_2O_3 was present at lower than 1477 °C and Ni was formed at 772 °C and present below 1427 °C. The operating pressure, long residence time, and complex chemistry of the system make bench-scale testing and thermodynamic calculations very difficult, especially without knowing the actual mineral species forming in the gasifier.

It was shown in previous publications that metals such as vanadium are bound with organic matter in the form of organometallic compounds. These compounds are decomposed by heat-treatment into V_2O_3, microcrystals remaining trapped inside of the carbon pores (inert gas/heating rate 4 °C/min to 20 °C/min /temperature up to 1000 °C) [64, 65]. After the heat treatment of the fuel, char fragments with a high concentration of metal are found in some areas while other areas are nearly free of metal. This indicates that after pyrolysis process the distribution of vanadium in the char is not even, implying the vanadium could accumulate together in certain areas. In real gasification case, initially, vanadium forms V_2O_5. The low melting point makes it vaporize very fast in the heating zone. With the consumption of oxygen, the V_2O_5 will be gradually reduced into V_2O_3. With combustion of the carbonaceous matrix, vanadium is released to the atmosphere as fine fly ash with a long atmospheric residence time. About 80% of the vanadium-containing particles have a mass median aerodynamic diameter smaller than 0.5 μm at the exit of the chimney of a combustion unit [66].

Liu et al. [67] employed $VO(Ac)_2$, $VOSO_4$, NH_4VO_3, and V_2O_5 as precursors and reduced them with ethanol. It was found that the reduced vanadium oxides with irregular shape were formed, as shown in Figure 2.15 a–d. Interestingly, when V_2O_5 was mixed with ethanol and CO_2 keeping other experimental

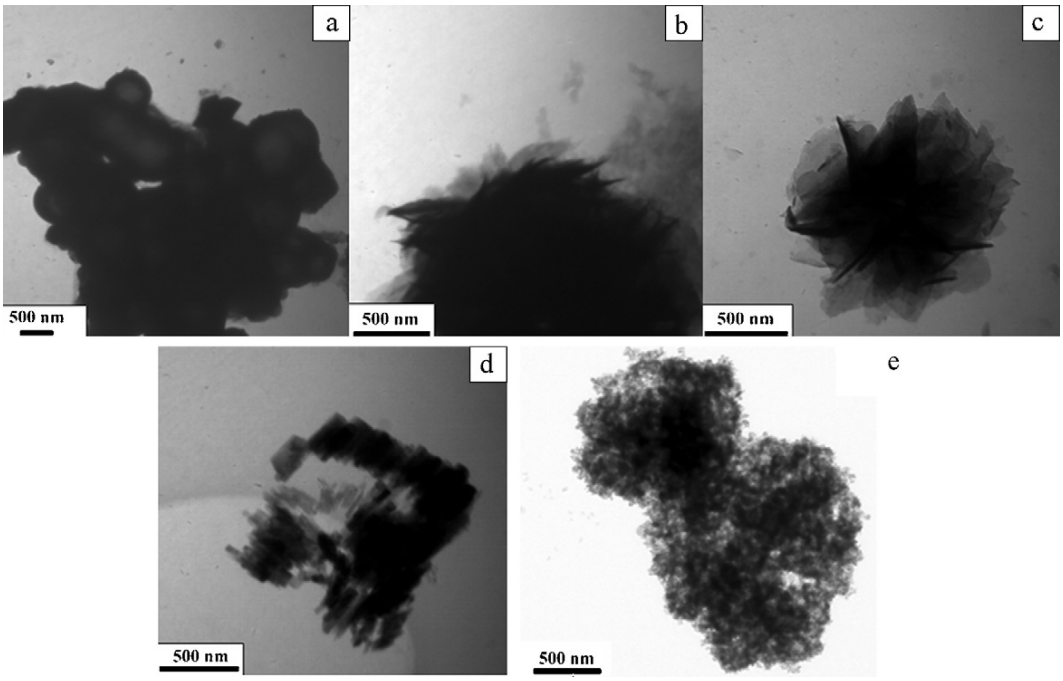

Figure 2.15: TEM images of the obtained vanadium oxides: (a) the $VO(Ac)_2$ as precursor; (b) the $VOSO_4$ as precursor; (c) the NH_4VO_3 as precursor; (d) the V_2O_5 as precursor; (e)the V_2O_5 as precursor and infused carbon oxides before reaction [67].

variables invariant, sphere-like V_2O_3 nanoparticles were prepared (Figure 2.15 e), indicating that carbon oxides could play an important role on the morphology of V_2O_3 nanoparticles. The carbon oxides may be favorable to fabricate the V_2O_3 sphere-like nanoparticles during the reduction. The possible growth mechanism of the sphere-like V_2O_3 nanoparticles is described diagrammatically in Figure 2.16. The reduced V_2O_3 crystal nucleus is surrounded by carbon which could not only prevent V_2O_3 particles from aggregating together but also control the growth morphology of V_2O_3. After that, the sphere-like V_2O_3 nanoparticles are formed by self-assembly on a large scale.

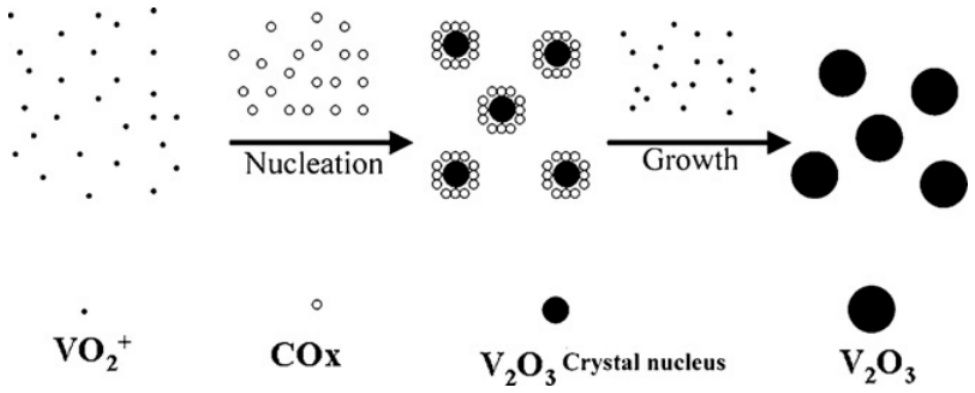

Figure 2.16: Possible growth mechanism of sphere-like V_2O_3 nanoparticle [67].

Chapter 3

Experimental Section

3.1 Experimental Setup

The experiments were carried out in an atmospheric entrained-flow reactor set up. The experimental setup is shown schematically in Figure 3.1. The reactor furnace consisted of an electrically heated vertical core housing a mullite tube (63.5 mm i.d., 1546 mm height). The maximum working temperature of the reactor was limited by the mullite tube (McDanel MV-30) to 1500 °C. The temperature of the reactor was fixed along the tube length using three proportional-integral-derivative (PID) temperature controllers (Omron E5CK) at the top, middle, and bottom of the reactor. A screw feeder (Schenck AccuRate volumetric feeder) with pulsating walls and a flight-free auger with a stirring rod and poly nozzle was used to feed the solid feedstock into the reaction tube through a custom-designed feeder probe. The nominal capacity of the feeder ranged from 8 to 150 g/h. The screw feeder used for the entrained-flow reactor is shown in Figure 3.2. A primary flow of nitrogen was used to entrain the particles into the reaction tube. The nitrogen having a 99.998% purity was supplied from a compressed gas cylinder through a mass flow controller (Alicat Scientific, Inc.) with a 0–30 L/min range. Pyrolysis products were collected through a jacketed air-cooled collection probe. Following the collection probe, the cooled stream was passed through a Dekati cyclone where char and ash samples were removed from the sample particle stream. The nominal gas flow through the cyclone was 10 L/min with a cut diameter of 10 μm.

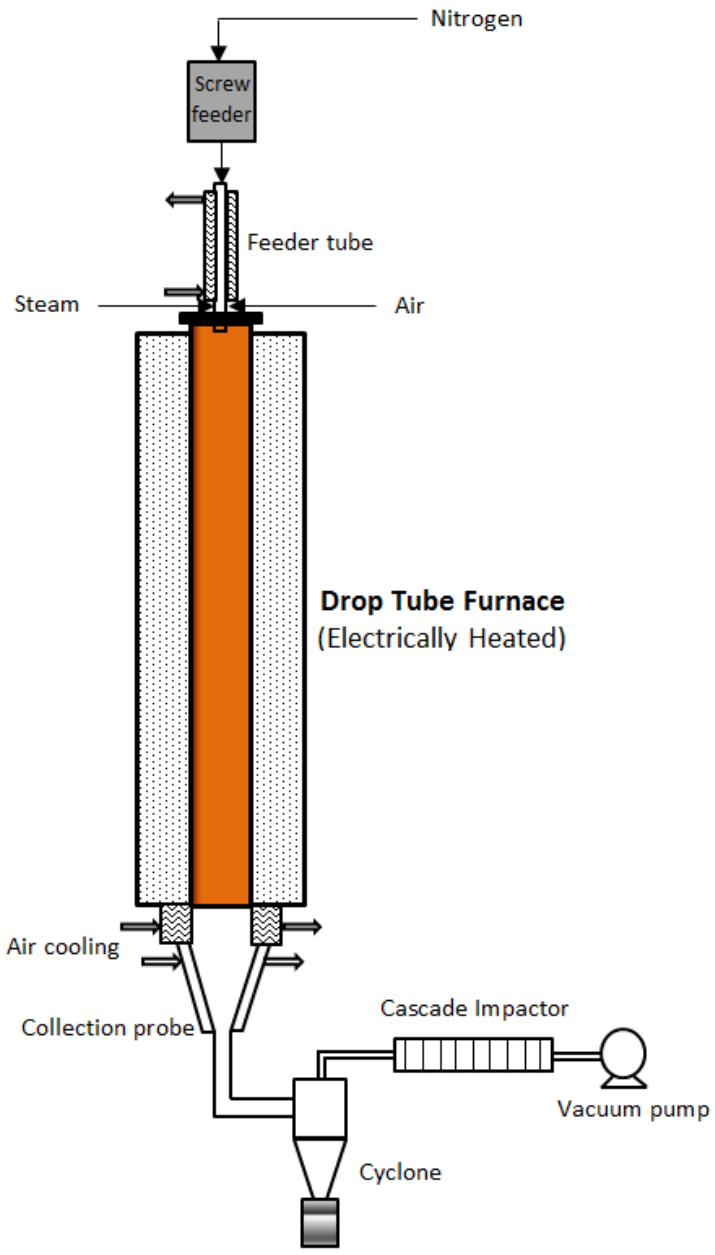

Figure 3.1: Schematic diagram of the entrained-flow reactor.

Figure 3.2: Schenck AccuRate volumetric feeder.

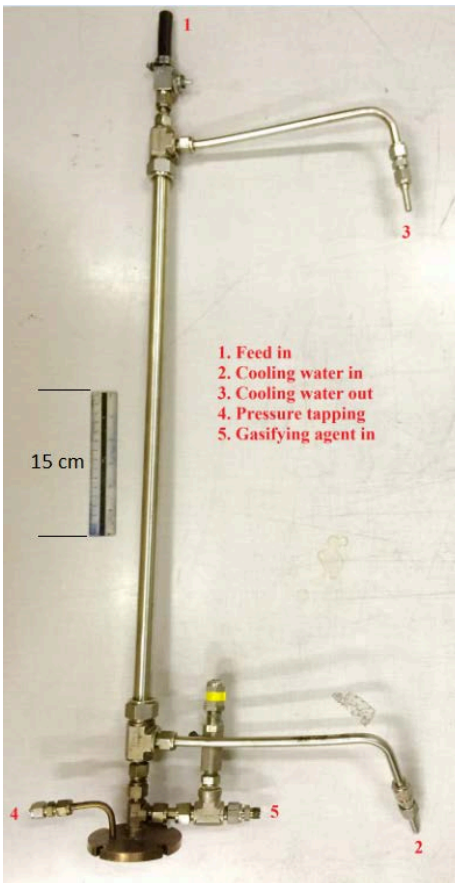

Figure 3.3: Design of feeder tube.

The maximum operating temperature for the cyclone is around 600 °C, but the gas temperature in the cyclone for the present experiments did not exceed 100 °C.

The original feeding system to the reactor was of liquid mode in which the asphaltene fine particles are heated to around 300–350 °C in a stainless steel vessel using heating tapes. Thermocouples of K-type are used to control the temperature and a magnetic stirrer is used to mix the molten asphaltene properly. The molten asphaltene is fed to the reactor using a heat traced tube. Because of the continuous problems in the coking and blockage of the feeding system, the feeder was redesigned to feed asphaltene in solid form using a solid feeder. The feeding tube connected the volumetric feeder to the reactor. Since

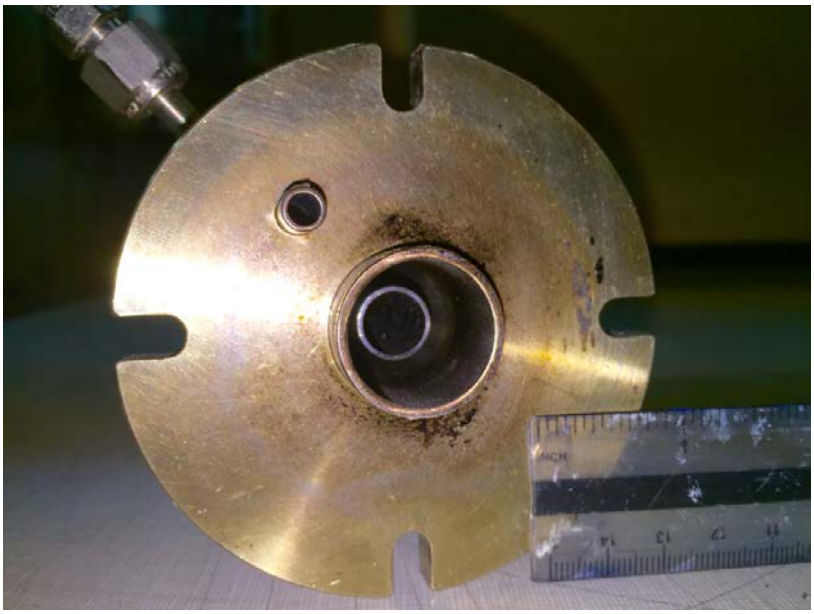

Figure 3.4: Drop tube furnace header with feeder tube.

the feeding tube was very close to the hot furnace, the inner wall of the tube became hot enough to cause sticking of fine asphaltene particles. The heat transferred from the hot surface to the feeder tube due to natural convection. To avoid this occurrence, the feeding tube was designed as a double-walled tube with cooling water passed through the annulus. The custom designed feeder arrangement is shown in Figure 3.3. An external air cooling system was also provided to the feeder end connecting to the hot reactor, where the temperature was still high. A flange of 0.5 cm thickness attached to the feeder tube was used as the header to cover the top end of the mullite tube. The tip of the feeding tube was protected from over heating by extending the outer annular tube by 2 cm below the flange as shown in Figure 3.4. For pyrolysis experiments only one inlet was available for the supply of nitrogen, whereas, two gas inlets were used for air and nitrogen separately. Similar arrangement was used for the steam gasification with steam and nitrogen inputs. A custom designed low-pressure steam generator in combination with a high precision water metering pump (Eldex, Opto series with a flow range of 0.002-80 mL/min) was used to supply the steam for the setup.

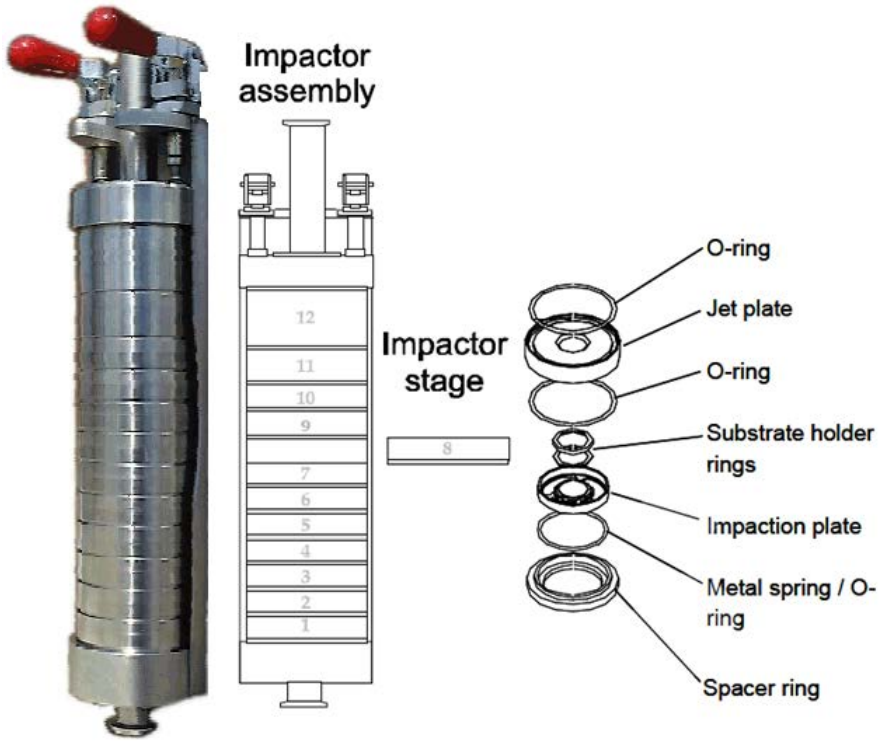

Figure 3.5: Cascade impactor [68].

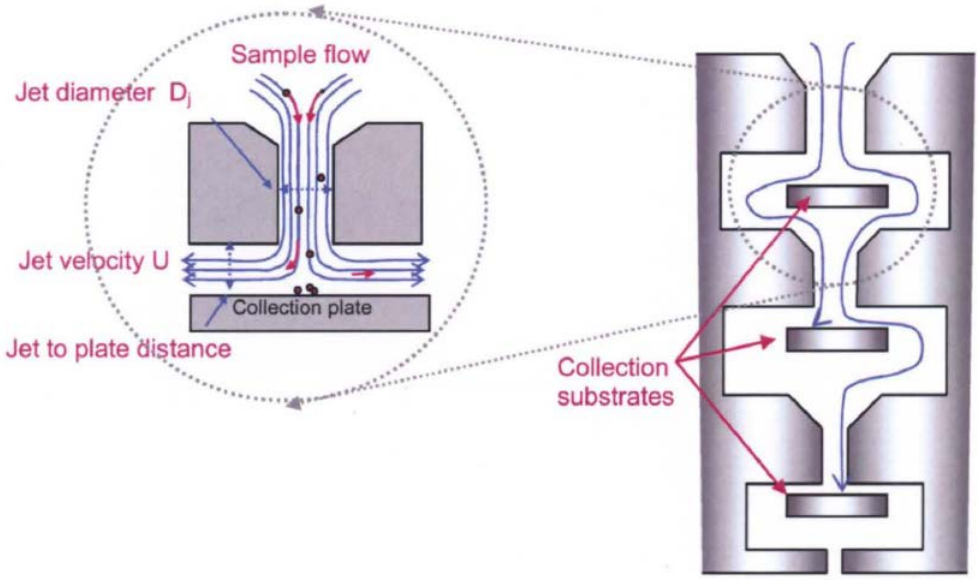

Figure 3.6: Particle collecting mechanism of cascade impactor [68].

Table 3.1: Cascade Impactor Stage Data [68]

Stage	13	12	11	10	9	8	7	6	5	4	3	2	1
D_{50} (μm)	10	7	4.3	2.7	1.8	1.1	0.7	0.4	0.3	0.2	0.1	0.06	0.03

The exit gas from the cyclone was then passed through a Dekati low pressure impactor (DLPI) to collect the fine soot particles, with sizes ranging from 0.03 to 10 μm, in 13 channels (Figure 3.5) [68]. The DLPI measures airborne particle size distribution and the measurement range could also be extended to particle sizes below 0.03 μm by using a total filter stage at the end of the impactor. The cut particle sizes for different stages of the cascade impactor are shown in Table 3.1. The impactor is an inertial device that classifies particles according to their aerodynamic diameters. The operation principle of the impactor is based on inertial classification and gravimetric analysis of the aerosol particles. Aluminum foil of 25 mm diameter is used as collection substrate which is fixed on a substrate holder. The cascade impactor is a simple device with two co-linear plates of which the other has a small nozzle in it. The plate having nozzles is called the jet plate and the other is the collection plate. Aerosol passes through the nozzles of the jet plate with high speed and makes a sharp turn to flow between the plates as shown in Figure 3.6 [68]. Particles larger than a certain size characteristic to the dimensions of the impactor cannot make the sharp turn and impact on the second plate. Several successive impactor stages like this with decreasing cut diameters collect the particles according to their size.

The nominal gas flow rate through the cascade impactor is 10 L/min. The gas flow and pressure are maintained with the help of a vacuum pump (115 V/60 Hz IA-906 Dekati) with a recommended flow rate of 14 m^3/h at 100 mbar. A positive gauge pressure close to zero at the top of the reactor is set using the needle valve connected in between the cascade impactor and

Table 3.2: Proximate and Ultimate Analysis of Asphaltene.

Proximate Analysis (wt%)		**Ultimate Analysis (wt%)**	
Moisture	0.1	C	82.68
Ash	0.6	H	8.34
Volatile	63.0	N	1.2
Fixed Carbon	36.3	S	7.75
		O	0.03

the vacuum pump. The residence time of the pyrolysis experiment in the entrained-flow reactor was varied by varying the flow of nitrogen that carried the reacting fuel particles through the hot furnace. The residence time was calculated by considering complete entrainment and using the ideal gas law. The residence time could be decreased by increasing the flow of nitrogen. The GasAlertMicroClip gas detector of BW Technologies by Honeywell is used for detecting any CO and H_2S leakage during experiment. After each experiment the sample is kept overnight before collecting to allow cooling and escape of any entrapped poisonous gases.

3.2 Feed Asphaltene

The feed asphaltene for this study was obtained from a deasphalting unit similar to that depicted in Figure 1.2 at Fort McMurray in northern Alberta, Canada. These asphaltenes were solid at room temperature and dark brown in color (Figure 3.7). Dry grinding of asphaltenes was carried out in a Retsch Planetary Ball Mill PM 100. The grinding at speeds of 450 rpm for 10 minutes produced intermediate sized particles and subsequently, it was manually ground to finer particle sizes. Longer grinding to get fine sized particles is not recommended due to the sticking of asphaltene particles together and also with

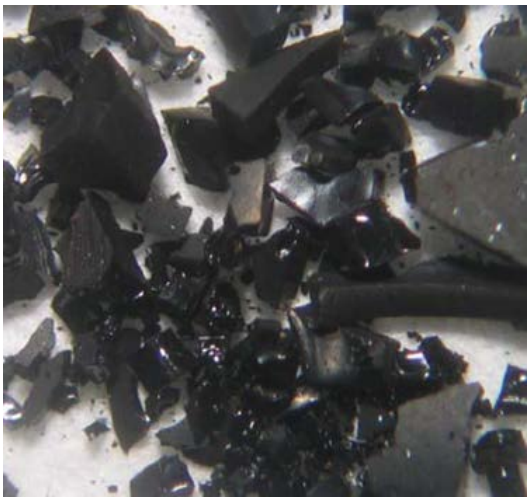

Figure 3.7: Feed asphaltenes as received.

the balls of the mill. The heat generated during grinding causes the sticking or melting of the asphaltene particles. Pulverized asphaltenes were sieved to various cut sizes such as 53-106 μm, 106-150 μm and 150-212 μm. The effect of feed particle size on the properties of soot formed was investigated using these different feed sizes.

Asphaltenes are the heaviest and most polar molecular component of any carbonaceous material such as crude oil, bitumen, or coal. Asphaltenes consist mainly of carbon, hydrogen, nitrogen, oxygen, and sulfur with trace amounts of vanadium and nickel. The proximate analysis of asphaltene was carried out in accordance with ASTM D7582, standard test methods for proximate analysis of coal and coke by macro thermogravimetric analysis using LECO 701 TGA and the ultimate analysis including oxygen was carried out by elemental analyzer (Carlo Erba EA 1108). To get an acceptable experimental error less than 5%, sulfanilic acid was measured as a standard sample for at least five times before the measurements. The proximate and ultimate analyses of the asphaltene are shown in Table 3.2 [69]. It can be seen that asphaltene contains low ash (less than one percent), but is high in volatile matter and fixed carbon. The sulfur content in asphaltene is rather high compare to traditional fuels

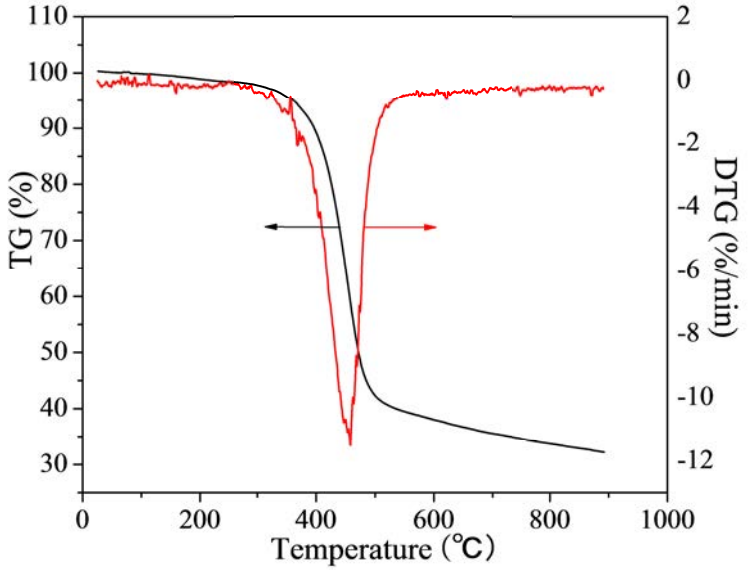

Figure 3.8: TG and DTG curves for asphaltene from 25 and 900 °C in N_2 atmosphere with a heating rate of 15 °C/min.

such as coal and biomass, and the H/C mole ratio is around one due to being composed of mostly aromatic components. The trace elements present in the asphaltene were mainly vanadium and nickel. It has been reported in the literature [70] that Athabascan asphaltene contains 1763 ppm vanadium and 671 ppm nickel.

3.3 Thermal Analysis of Asphaltene

Thermogravimetric analysis (TGA) is extensively used to study the thermal behavior of carbonaceous fuels in which changes in mass are recorded over both temperature and time to analyze the physical and chemical changes of the sample. Figure 3.8 shows the thermogravimetric (TG) and differential thermogravimetric (DTG) curves for asphaltene between 25 and 900 °C in N_2 atmosphere with a heating rate of 15 °C/min. The rupture of chemical bonds and release of volatile materials from asphaltene cause a continuous weight loss with increasing temperature. Due to the low content of moisture in asphaltene

and storage in drying oven at 105 °C, the initial weight loss corresponding to the loss of physically adsorbed water occurring between 25 and 200 °C is slight. As temperature increases, the largest weight loss is observed at around 400–550 °C corresponding to the release of volatiles by devolatilization reactions. The maximum weight loss rate is 11.5%/min at 458 °C. The result is in accordance with Ritchie et al., [71] who employed the pyrolysis products to reflect the complex physical and chemical changes during non-isothermal pyrolysis in the temperature range up to 927 °C. They found that the peaks for most volatiles released from asphaltene appeared around 427 °C. These results indicate that aliphatic side chains and heteroatoms are released in this temperature range, further promoting the aromatization of asphaltene. Afterwards, a slight weight decrease from 39.48 to 32.2% is observed when the pyrolysis temperature increases to 900 °C. The minor weight loss can be attributed to the degradation of the macromolecular structure in the solid matrix.

Chapter 4

Analysis of Pyrolysis Soot*

4.1 Introduction

Pyrolysis is the thermal cracking of chemical bonds in the fuel in an inert atmosphere to produce gaseous, liquid and solid components and the yield of it mainly influenced by the temperature, heating-rate and residence time. The initial step of gasification is pyrolysis, during which the fuel devolatilizes to form char, primary gases, and tar. This char undergoes various heterogeneous reactions to form syngas, while tar undergoes cracking and polymerization reactions to form secondary gases and soot. Soot is one of the main pollutants in any combustion or gasification process. Soot is a carbonaceous solid material that is formed during pyrolysis and flame combustion. Soot formation is a complex process that involves many chemical and physical steps. Soot particles from various sources (i.e., from different fuels and combustion conditions) tend to be similar in size and composition, which indicates that the same formation processes and growth constraints apply, but because of the complexity, a number of uncertainties still remain.

Different soot formation mechanisms are described in chapter 2. All of these mechanisms explain the formation of soot; some represent the formation of soot from light gaseous fuels or from light products of combustion of other fuels.

*A version of this chapter has been published as "Analysis of Soot Formed during the Pyrolysis of Athabasca Oil Sand Asphaltenes"in *Energy and Fuels*, 2015, 29, 6823–6831.

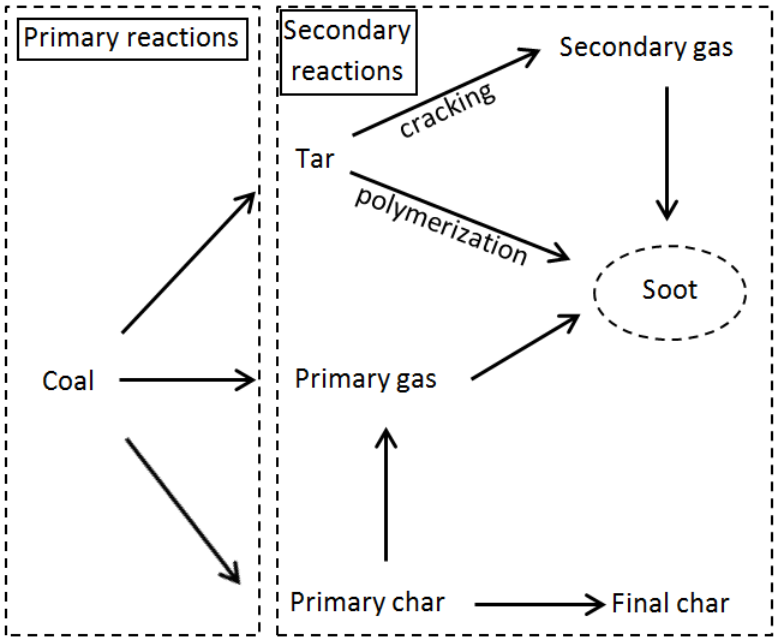

Figure 4.1: Presumed pathways for soot formation.

It is clear that soot formation pathway and mechanism are very complicated. The feed for the present study is more comparable to coal rather than gaseous fuels, so a mechanism of soot formation and soot morphology with reaction pathways similar to that of coal is needed. Zhang [72] suggested an improved comprehensive soot formation mechanism, based on the mechanism suggested by Ma [45] that is more relevant to the present study (Figure 4.1). The coal initially devolatilizes to liberate tar (which is liquid at room temperature), light primary gases, and primary char. The tar undergoes cracking or polymerization reactions to form secondary light gases or soot, respectively, according to the reaction atmosphere. These secondary light gases may contribute to the surface growth reactions of the primary soot formed by polymerization. Soot can also be formed from the primary light gases formed during devolatilization. The primary char produces some primary gases before it becomes final char. According to Howard [73] the addition of small molecules to the soot nuclei is the principal pathway for soot formation in hydrocarbon flames. Soot nucleation also involves the growth of heavy PAH by reactive coagulation. PAH also contributes significantly to the post-nucleation growth of soot particle;

however, most of the mass of the soot system appears to come from C_2H_2. Wornat et al. [74] suggested that during coal combustion, large tar molecules attach to soot nuclei directly, rather than breaking up into small acetylene molecules, followed by addition of acetylene to soot nuclei.

Pyrolysis experiments were conducted in a nitrogen atmosphere at temperatures of 1000, 1200, and 1400 °C. The temperatures mentioned are the set temperatures of the electrically heated furnace. The asphaltene particles are fragmented during pyrolysis to form char and soot at the same time, and both are collected in the cyclone separator and cascade impactor, respectively, and are then analyzed. The residence time of the entrained-flow reactor can be varied by varying the flow of gas stream that carries the reacting fuel particles through the hot furnace. The residence time was calculated considering the ideal gas law. By increasing the flow of carrier gas, we could decrease the residence time.

4.2 Results and Discussion

The fine soot particles flowed through a cyclone separator and were collected on the 13 stages of the cascade impactor according to their size distribution. Figure 4.2 shows the soot particles collected on the aluminum substrate holder fitted on impaction plates of stages 1–6 for the pyrolysis experiment conducted at 1200 °C. The amount of soot collected was minimal on the first stage, which corresponds to a cut particle size of 0.03 μm. Greater amounts of soot were collected on the subsequent stages. Usually the top few stages of the cascade impactor (stages 9–13) were contaminated with the carryover of char particles with diameters less than 10 μm. The cut particle size of the cyclone separator used to collect the char particles was 10 μm. The morphological and structural characteristics were examined by field-emission scanning electron microscopy (FE-SEM) using a JEOL 6301F scanning electron microscope, which provides high-resolution digital images of surface textures and microstructures at mag-

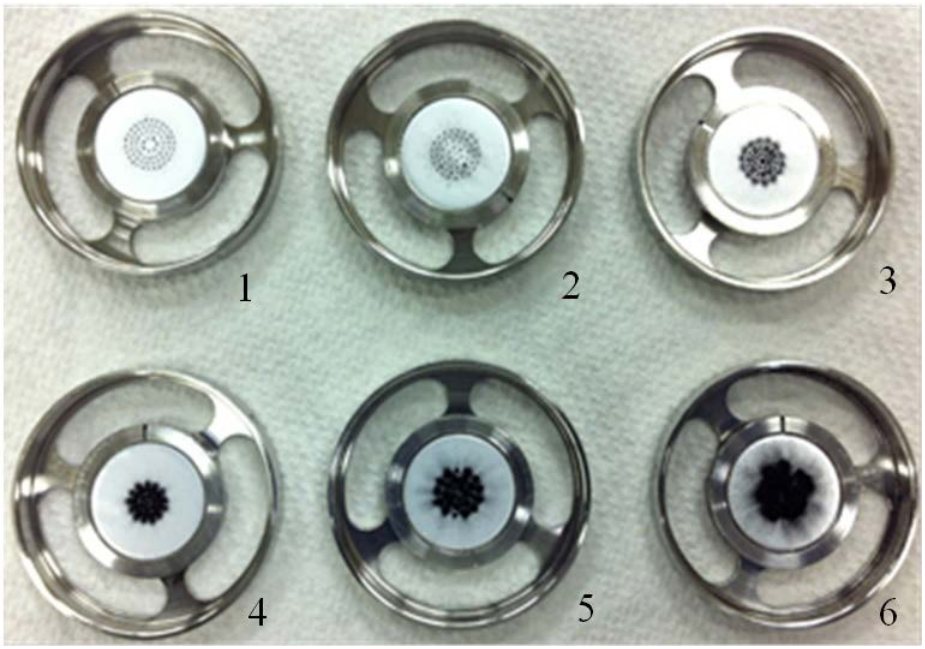

Figure 4.2: Soot on stages 1–6 of the cascade impactor.

nifications ranging from 20X to 250000X. SEM is an optical analysis method for solid samples in which a focused electron beam is pointed to the sample surface to create the surface images. Because of the interaction between the electron beam and the atoms at the surface of the sample, the electrons in the top layers of the sample leave their discrete energy level in the matrix of the solid. The detection of these secondary electrons (SE) gives the topography and morphology details of the sample. The SEM results confirmed the presence of large char particles in the soot collected on the top stages (stages 9–13). This was important when we characterized the soot. Thus, before carrying out any detailed analysis, we had to make sure that the soot was not contaminated with char particles. The SEM image of contamination of the soot on the 11^{th} stage of the impactor is shown in Figure 4.3. The spherical char particles with diameters of 5–10 μm are surrounded by very fine soot.

Soot particles collected on different stages of the cascade impactor were analyzed using SEM. Though the impactor was intended to separate particles on the basis of size, the SEM images showed that the separation was not per-

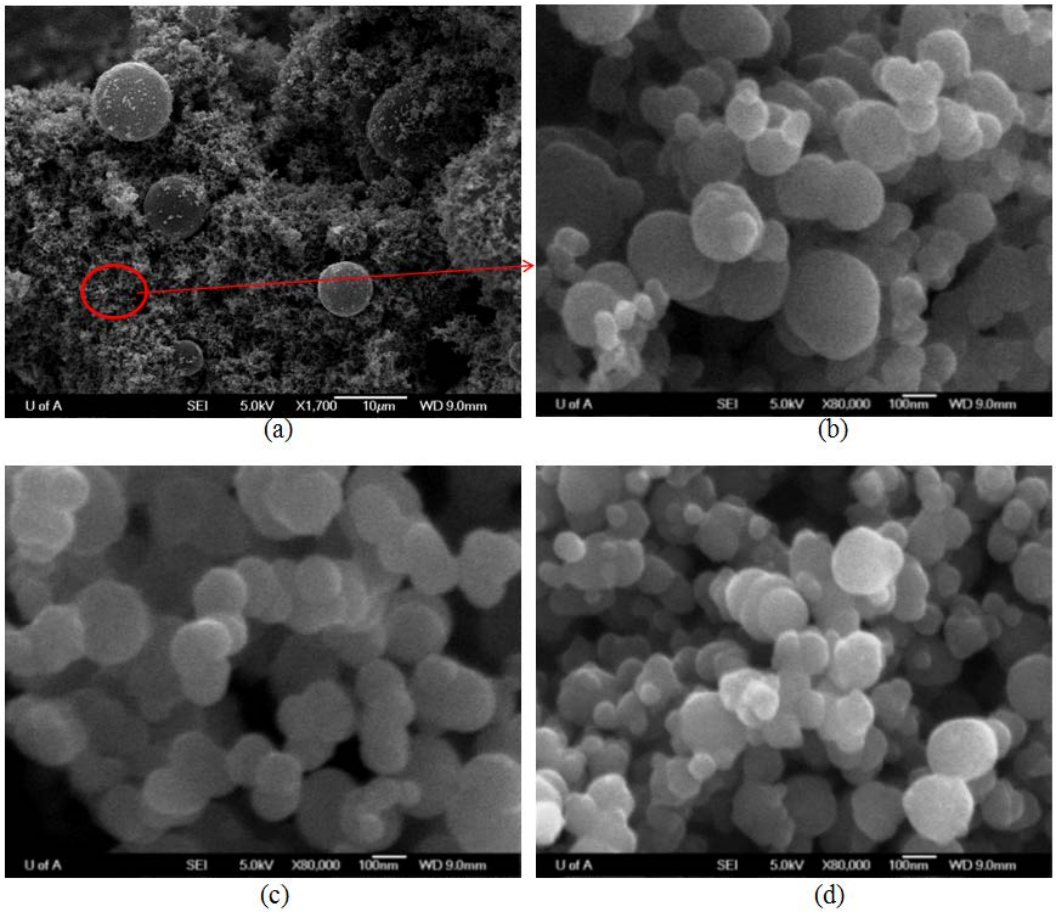

Figure 4.3: SEM images of soot collected on different stages of the cascade impactor during pyrolysis at 1200 °C: (a) stage 11; b) magnified image of the circled portion in (a); (c) stage 3; (d) stage 8.

Table 4.1: Ultimate Analysis of the Soot Collected for Different Feed Particle Sizes

Feed size	C (wt%)	H (wt%)	N (wt%)	S (wt%)
53–106 μm	95.04	0.56	0.47	3.93
106–150 μm	95.42	0.50	0.46	3.62
150–212 μm	95.17	0.53	0.49	3.81

fect. This would be due to the existence of agglomerates in the original gas stream. When the soot agglomerates pass through the perforated stages of the cascade impactor, the loosely bound agglomerates break easily, pass through the top stages, and get deposited on the lower stages. The larger strong agglomerates could break into intermediate-sized agglomerates and tended to get deposited on the middle stages. Thus, a clear classification of primary soot particles in the size range between 50 and 200 nm could not happen. The primary soot particles collected on different stages appeared to be similar in shape and structure, as shown by the SEM images (Figure 4.3b–d). Even though the soot particles were collected on stages 3, 8, and 11, all of these stages had a primary particle size between 50 and 200 nm. The soot particles look like densely packed agglomerates in all of the SEM images in this study. This is because they were deposited by impaction on the aluminum substrates. Earlier literature reported the size of primary soot particles formed from different hydrocarbon flames as 25–50 nm [36]. In most of these cases, the soot volume fraction in the combustion gas was very low, so particle coagulation and agglomeration were limited to a certain extent and the agglomerates were sparsely distributed in the grid. In this study, the amount of soot formed in all of the experiments was high because of the inert atmosphere and the absence of any soot-destructing reactant in the gas stream.

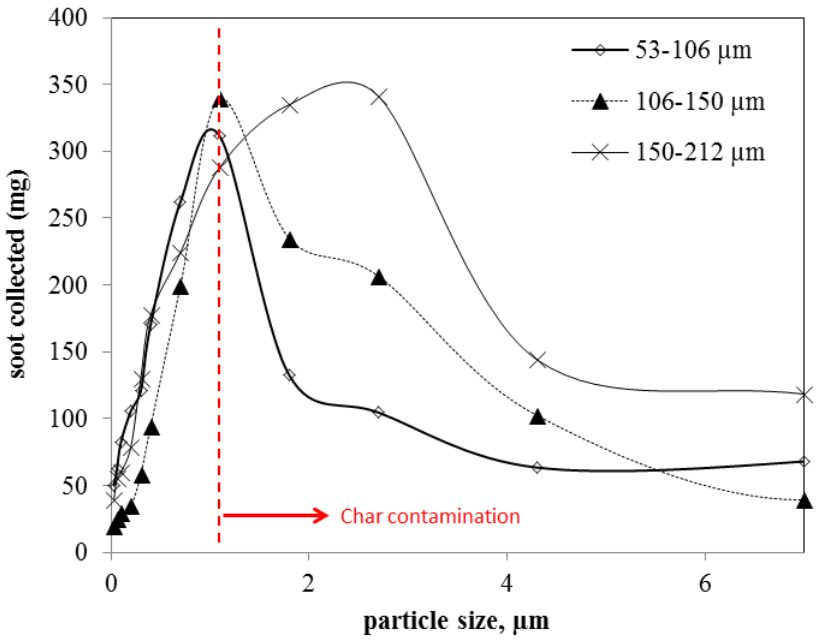

Figure 4.4: Particle size distribution of soot collected for different feed particle sizes.

4.2.1 Effect of Feed Particle Size

Pyrolysis was carried out with different feed particle sizes, and the effect of the feed particle size on the structure and characteristics of the resulting soot was investigated. The asphaltene particle sizes considered were (1) 53–106 μm, (2) 106–150 μm, and (3) 150–212 μm. Because of the very narrow size range for the feed asphaltenes, we did not perform particle size distribution measurements. The pyrolysis temperature was kept constant at 1200 °C and the residence time for all the experiments was maintained at 8.4 s for a better comparison of the results. Soot was collected on the 13 stages of the cascade impactor. The relative mass distribution of soot on each stage is plotted in Figure 4.4, and all of the feed particle sizes had a similar trend for the soot collected on stages 1–8, corresponding to a size range of 0.03 μm to 1.1 μm. The majority of the soot was collected on the stages corresponding to cut sizes of < 1 μm. Soot collected on stages 9–13 of the cascade impactor had char contamination as shown in Figure 4.3, and this caused a variation in the particle size distribution of the entire soot from stages 9 to 13. The soot from

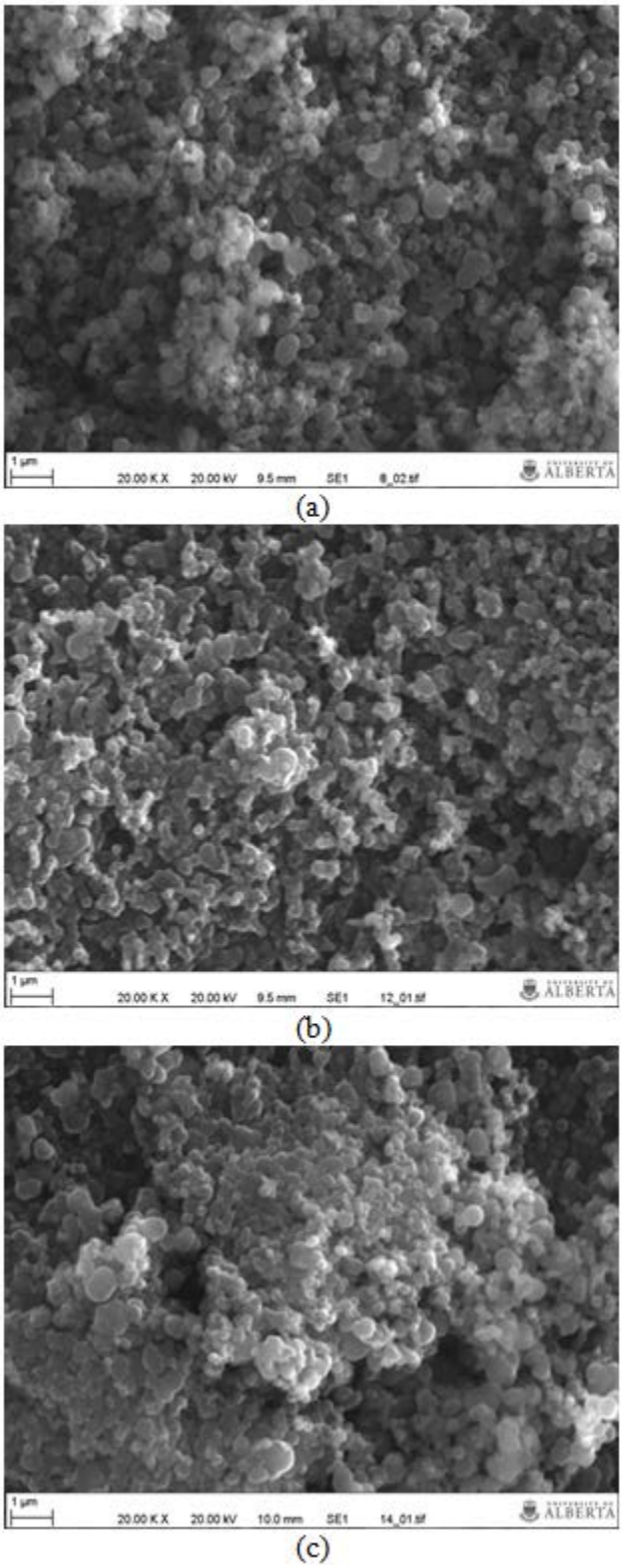

Figure 4.5: SEM images (at same magnification) of soot collected for different feed particle sizes on stage 5 of the cascade impactor: (a) 53–106 μm; (b) 106–150 μm; (c) 150–212 μm.

these stages was analyzed by SEM using the JEOL 6301F microscope. For consistency of the comparison, the soot used for SEM analysis was taken from the same stage number of the cascade impactor in all of the experiments. The morphology of the soot particles collected looked similar in all three cases. The particles appeared densely packed as a result of their deposition on the aluminum foil substrate with a low flow velocity. The SEM images are shown in Figure 4.5. The ultimate analyses of the soot obtained for different feed particle sizes showed similar compositions with respect to the amounts of carbon, hydrogen, nitrogen, and sulfur. The ultimate analyses were conducted using a Carlo Erba EA 1108 elemental analyzer, and the results are shown in Table 4.1. It was found that the feed particle size has a negligible effect on soot characteristics such as the particle size distribution, morphology, and elemental composition. Therefore, for the remaining pyrolysis experiments, the asphaltene feed particle size was fixed at 150–212 μm considering the higher yield from grinding and sieving operations and also its proximity to the industrial atomization range of asphaltenes fed to the gasifier.

4.2.2 Effect of Pyrolysis Temperature

The second objective was to investigate the effect of temperature on the properties of soot obtained from pyrolysis of asphaltene. The experiments were carried out at temperatures ranging from 800 to 1400 °C in the entrained-flow reactor. The temperature mentioned was the set temperature of the mullite tube. At low temperatures, such as 800 °C, a mixture of tar and soot was collected in the cascade impactor. The mixture was very sticky and was deposited on the walls of the cyclone separator and the tubes in the downstream portion of the reactor. Ma et al. [75] observed similar unstable liquid tar during high-temperature coal devolatilization. They found these droplets only at low and intermediate residence times, as the liquid tar droplets evaporated at higher temperatures. The morphology of this soot sample was very different from the soot formed at higher temperatures (Figure 4.6 (a)). According to

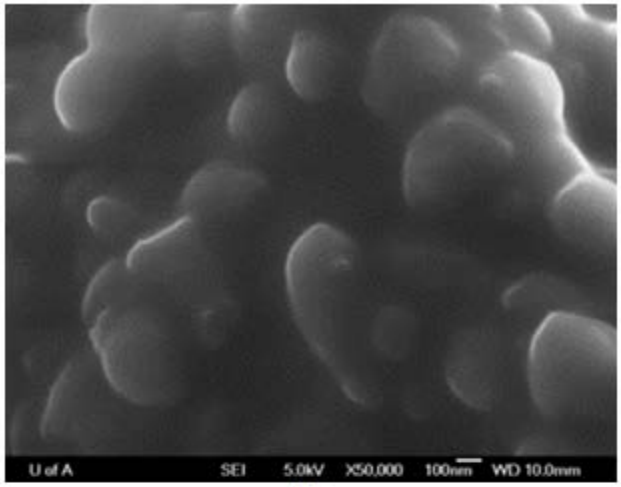

(a)

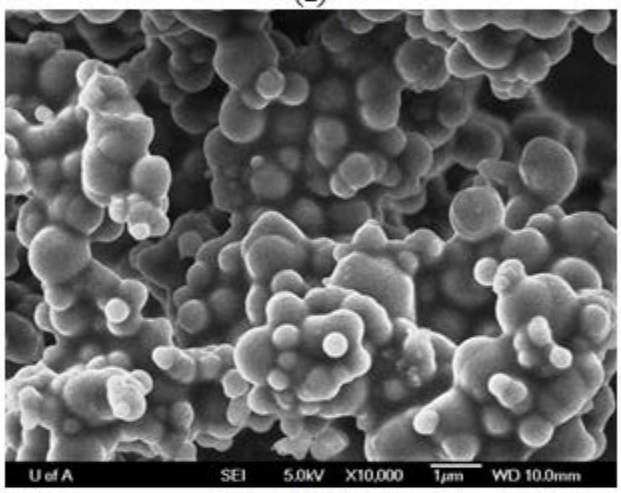

(b)

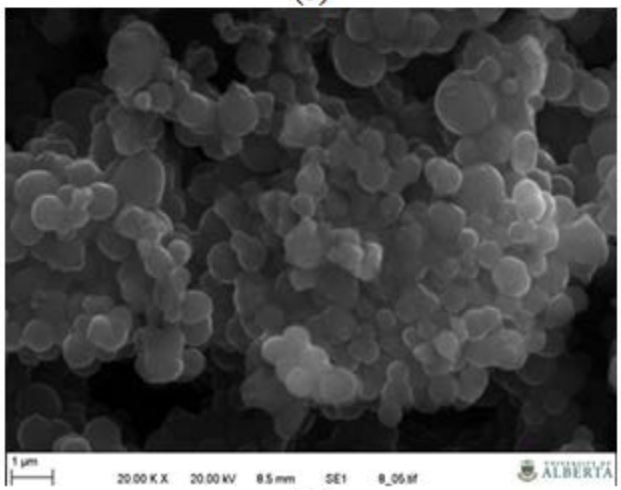

(c)

Figure 4.6: (a) & (b) Morphology of the mixture of tar and soot collected at 800 °C (c) Morphology of dried soot separated from the tar mixture formed at 800 °C.

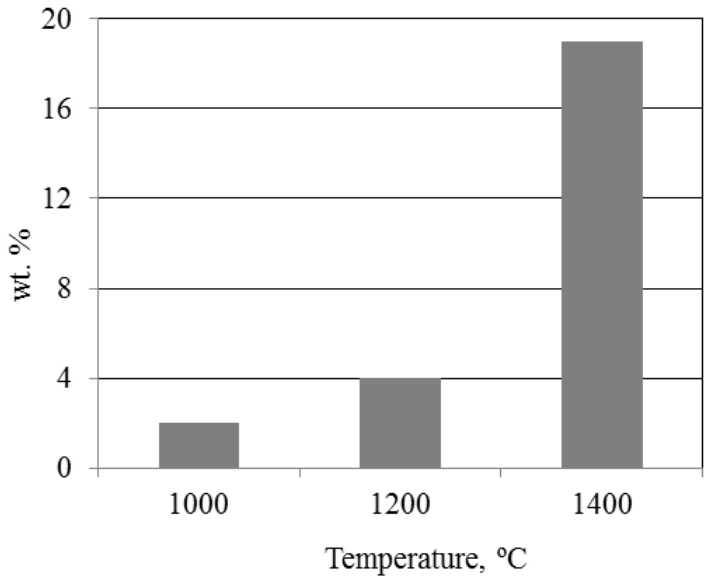

Figure 4.7: Soot yields at different pyrolysis temperatures.

the presumed pathway for soot formation (Figure 4.1), the fuel devolatilizes to release the char, light gas, and tar. The glue like material collected in the cascade impactor was the tar formed from the primary devolatilization reaction. Because of the absence of high temperature, this tar was not converted by tar gasification or soot formation reactions and was condensed in the downstream portion of the reactor. To confirm whether tar was partially converted to soot, the mixture of soot and tar was separated by the following method. The collected mixture was mixed with toluene to dissolve only the tar in the mixture, and the fine soot particles were then separated by filtration. The filtered soot was dried at 115 °C for 2 h. The SEM analysis of the dried soot is shown in Figure 4.6 (b). The average size of the soot particles was about 500 nm. The analysis showed that some soot was formed even at 800 °C, but it was mixed with tar. Estimation of the quantity of soot formed at 800 °C was not possible because of its association with sticky tar.

The yields of soot formed at 1000, 1200, and 1400 °C are shown in Figure 4.7. The observed soot yield increases with increasing temperature, which is in good agreement with the results reported in the literature (17, 19, 26). The high

soot yields reported by Chen [48], Nenniger [50], and Wornat et al. [76] were all obtained under inert conditions. All three of these groups reported that the sum of tar plus soot remained constant in their experiments; increases in the soot yield coincided with decreases in the tar yield. The profiles of soot yield versus temperature in these coal pyrolysis experiments showed no decreases at increased temperatures; the soot yields either increased with temperature monotonically or reached an asymptotic value. Chen [48] reported that more than 25% of the coal mass (dry ash-free mass) was converted to soot for a highly volatile bituminous coal at higher temperatures. Wornat et al. [76] also observed for a similar coal that about 20 wt% of the coal was converted to soot at high temperatures and long residence times. The maximum soot yield obtained during this asphaltene pyrolysis was nearly 20% at 1400 °C. This yield is comparable to the reported soot yields for coal pyrolysis.

Tar deposition was not observed at temperatures higher than 900 °C, perhaps as a result of the transformation of tar to soot or light gases according to the soot formation mechanism already discussed. Thus, it was confirmed that the soot formation mechanism for asphaltene is similar to that of coal as described by Zhang [72]. The size of the soot particles varied with changes in the operating temperature. The average size of most of the primary soot particles decreased with increasing temperature, as shown in Figure 4.8. These samples were taken from stage 3 of the cascade impactor from each experiment for a better comparison. We still have a combination of small and large primary soot particles in each stage due to the lack of good classification. The size variation is due to the change in the extent of surface growth of primary soot particles. There are two secondary reactions of tar during pyrolysis (Figure 4.1). Cracking of tar to form secondary light gases is predominant at temperatures of 1000–1300 K [77, 78]. Thus, the soot formed by tar polymerization (which is the minor reaction at low temperatures) is exposed to high concentrations of light gases such as acetylene. These light gases cause the surface growth reactions for the mass addition of soot particles [56]. On the other hand, at

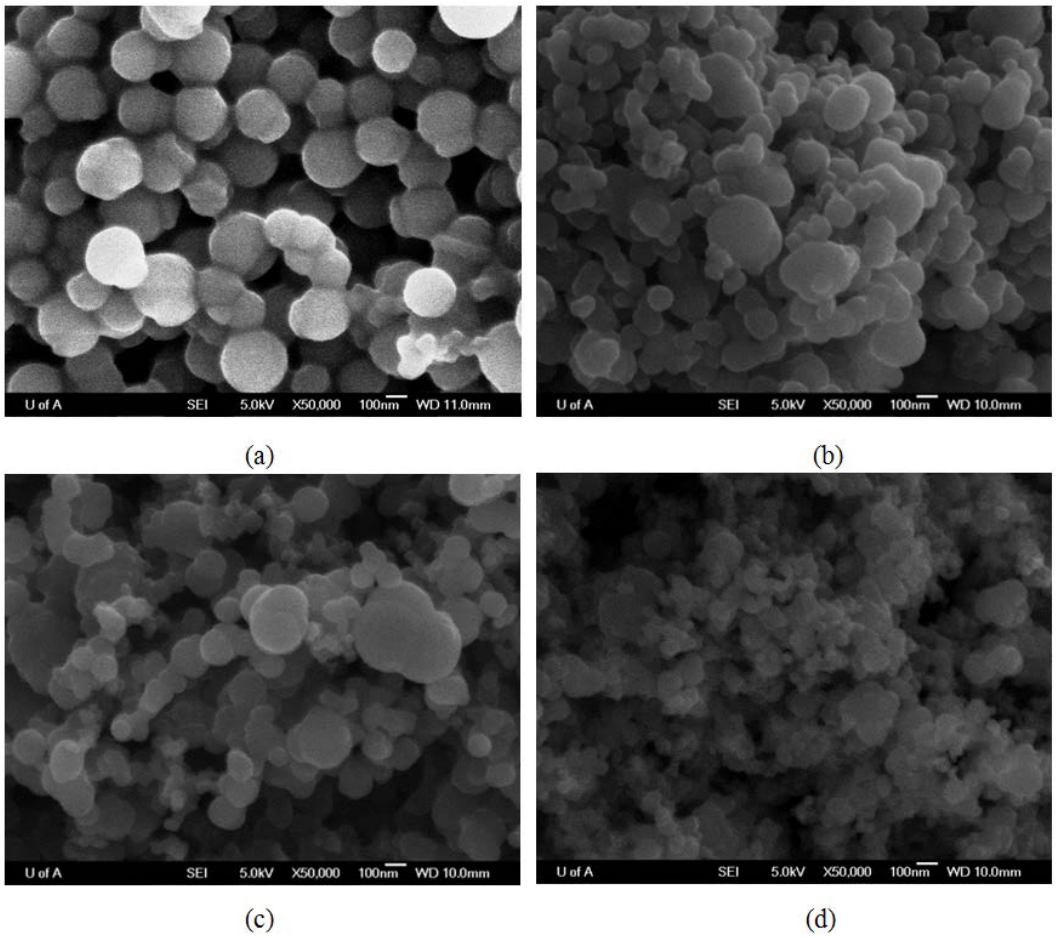

Figure 4.8: SEM images of soot particles collected at (a) 800 °C, (b) 1000 °C, (c) 1200 °C, and (d) 1400 °C on stage 3 of the cascade impactor. All images are at the same magnification.

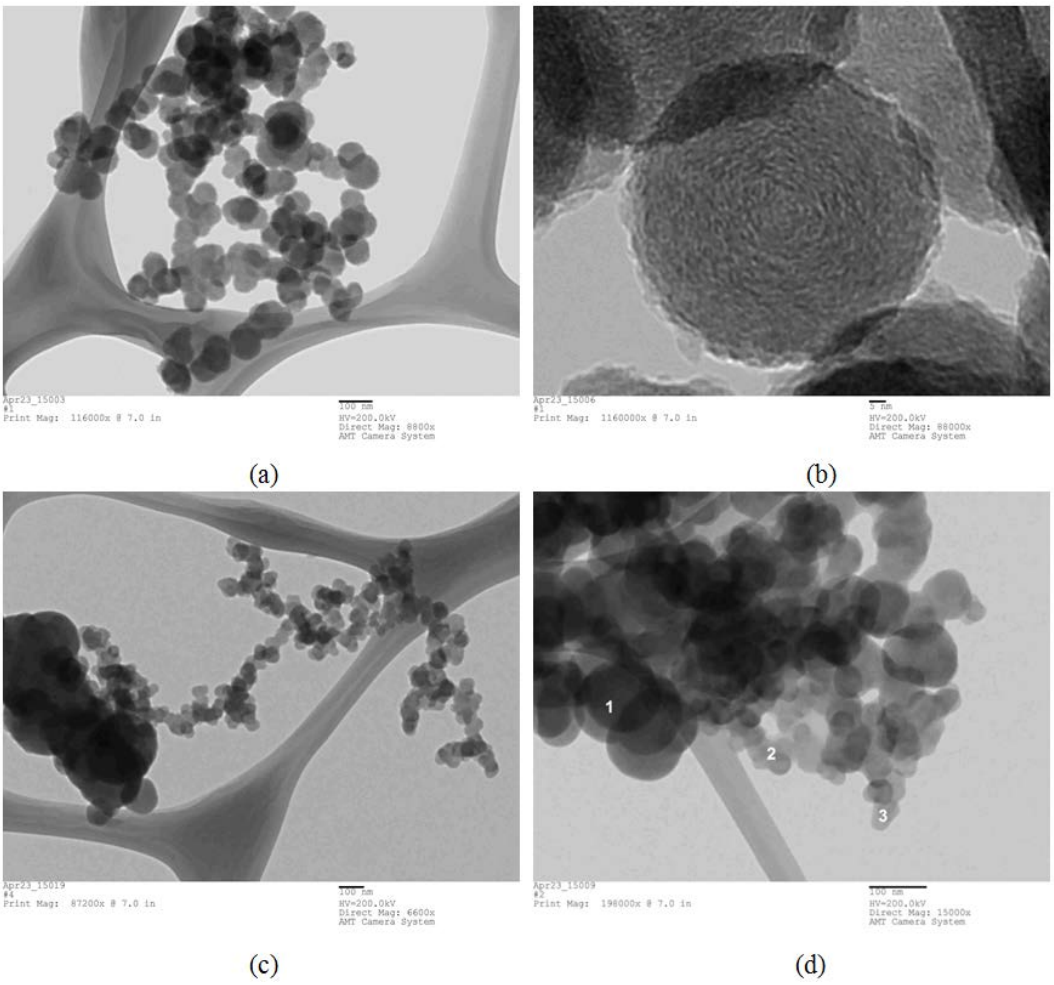

Figure 4.9: TEM images of the soot formed at 1400 °C.

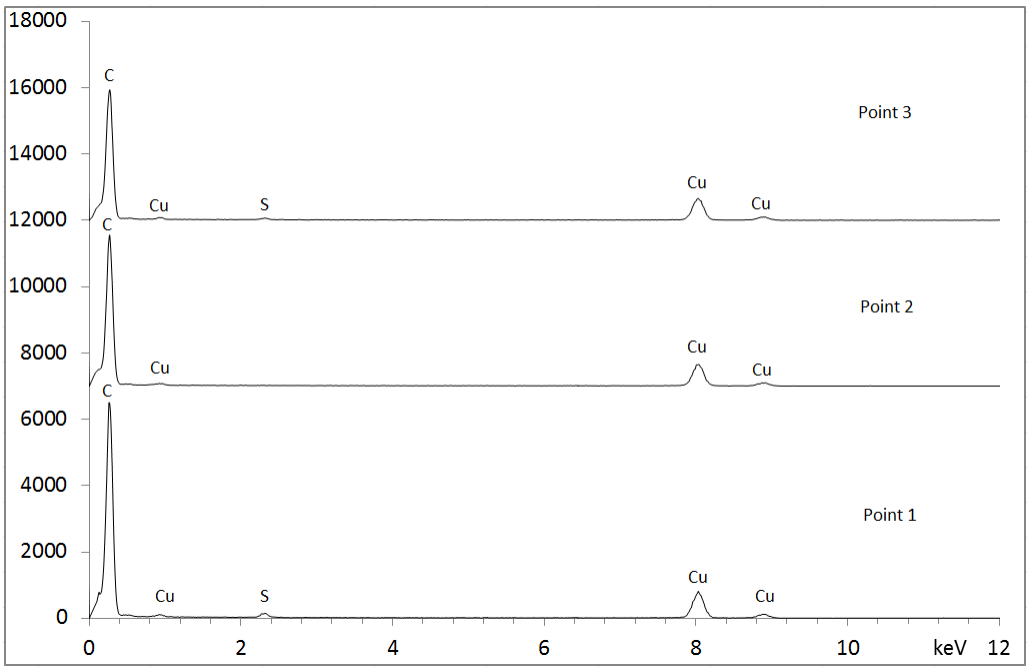

Figure 4.10: EDX analysis of points marked in Figure 4.9.

higher temperatures the tar cracking reaction is minor compared with primary soot formation from tar. Thus, the decrease in the concentration of light gases around primary soot particles lowers the rates of the surface growth reactions, and as a result, the soot particle size is lower at higher temperatures. Thus, the observed soot morphology is consistent with the soot inception and surface growth mechanism described in Figure 4.1.

Figure 4.9 shows transmission electron microscopy (TEM) images of the pyrolysis soot. Figure 4.9 shows the typical chain like agglomerates of soot particles collected at 1400 °C. The magnified image of a single spherule (Figure 4.9 (b)) is similar to nanocrystalline primary particles of Palas soot and diesel soot having the typical onion-shell structure [79]. The size of asphaltene soot is much larger than that of diesel soot, which is on the order of < 10 nm. Figure 4.9 shows two different particle sizes for primary soot or spherules. One of those spherules, with a size of < 50 nm, is bound together by chain like structures, whereas spherules with sizes of almost 200 nm are agglomerated

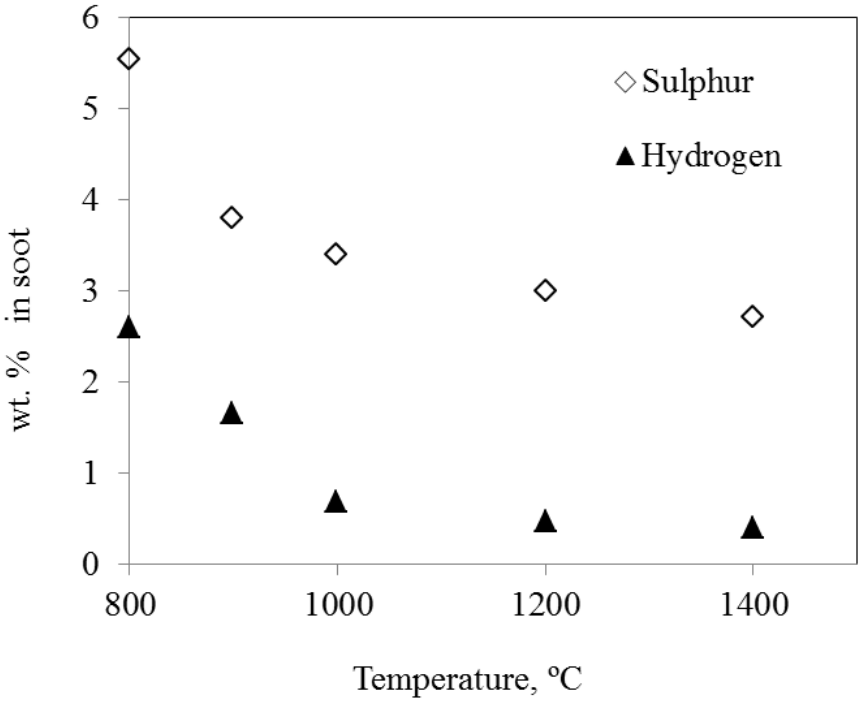

Figure 4.11: Sulfur and hydrogen contents in soot formed at different temperatures.

to form clusters with sizes of nearly 1 μm. Figure 4.9 also shows vigorous agglomeration of spherules of different sizes. The difference in spherule sizes may be due to the different mechanisms of soot formation, one from tar and another from light gases, and also to the surface growth reaction from acetylene as well as heavy PAHs. Energy-dispersive X-ray (EDX) spectroscopy of spherules of different sizes was conducted to confirm their compositions. In EDX a highly energetic electron, proton, or X-ray beam is directed to the sample where energy is partially absorbed by electrons of the sample atoms that temporarily jump to a higher energy level before returning to their original energy level emitting a photon that corresponds to the chemical composition. It is used as a comprehensive elemental analysis. The EDX results for the spherules marked in Figure 4.9 are shown in Figure 4.10. Both the large- and small-sized spherules mainly contained carbon. The copper shown in the EDX scans is from the TEM grid. The ultimate analysis shows a decrease in the percentages of sulfur and hydrogen in the soot with increasing pyrolysis

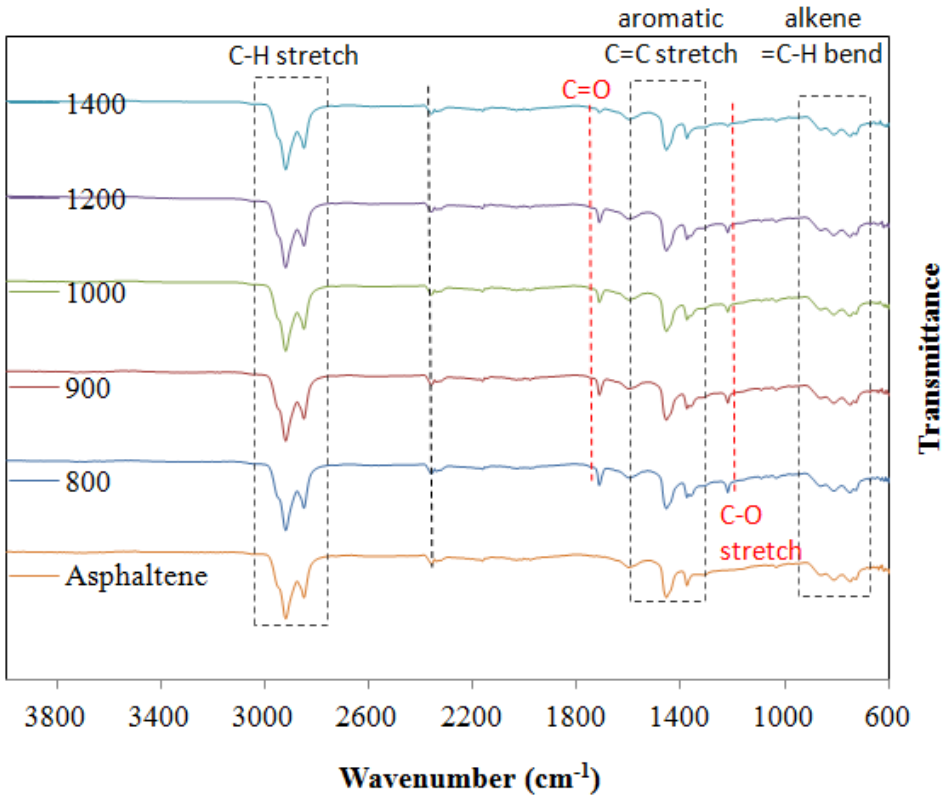

Figure 4.12: FTIR spectrum of asphaltenes and soot collected at different temperatures.

temperature. This is due to the liberation of sulfur as hydrogen sulfide during the pyrolysis reactions. This is more predominant at high temperatures, and accordingly, the sulfur content in the soot decreased with increasing pyrolysis temperature, as shown in Figure 4.11.

The Fourier Tranform Infra-Red (FTIR) spectroscopy spectra of soot formed at different pyrolysis temperatures are similar as shown in Figure 4.12. Infrared spectra of soot and asphaltene were recorded using ABB MB 3000 FTIR Spectrometer (detector gain 81, ZnSe beam splitter material). The IR transmittance spectra were obtained with a 4 cm^{-1} resolution between 400 and 4000 cm^{-1} and blank calibration was performed to ensure accuracy. Steps were also taken to ensure similar quantities of samples during each run. All the soot samples and asphaltene showed the –C–H stretch at a wave number

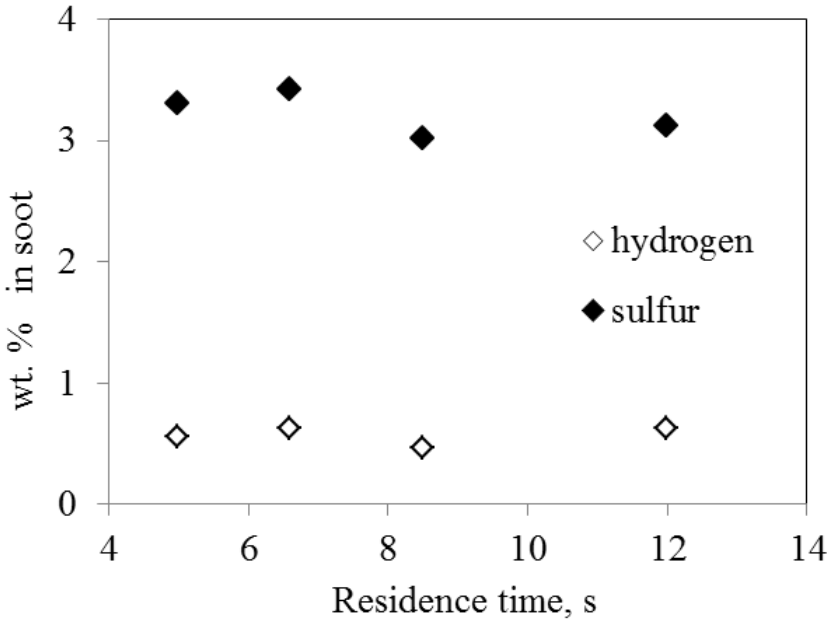

Figure 4.13: Sulfur and hydrogen contents in soot formed at different resident times.

of about 2850–3000 cm^{-1}. The aromatic C=C stretch and alkene =C–H bend also showed by asphaltene and all soots analyzed. The main differences between asphaltene and soot samples observed was in the case of carbonyl C=O bonds and C–O stretch. Asphaltene did not show any of these bonds. At the highest temperature of 1400 °C the peaks for these carbonyl bonds and C–O stretch were very weak. So the aromatic bond structures of soot collected at different temperatures were similar in nature except that of 1400 °C.

4.2.3 Effect of Residence Time

The residence times of the experiments in this study were in the range of 5–12 s, and all of the experiments were conducted at a constant temperature of 1200 °C. Ultimate analysis of the soot showed no significant change in the contents of sulfur and hydrogen with respect to the variation in residence time (Figure 4.13). As per the SEM images shown in Figure 4.14, at a constant temperature the size of soot particles increased with increasing residence time. The increase in primary soot particle size with residence time was reported by

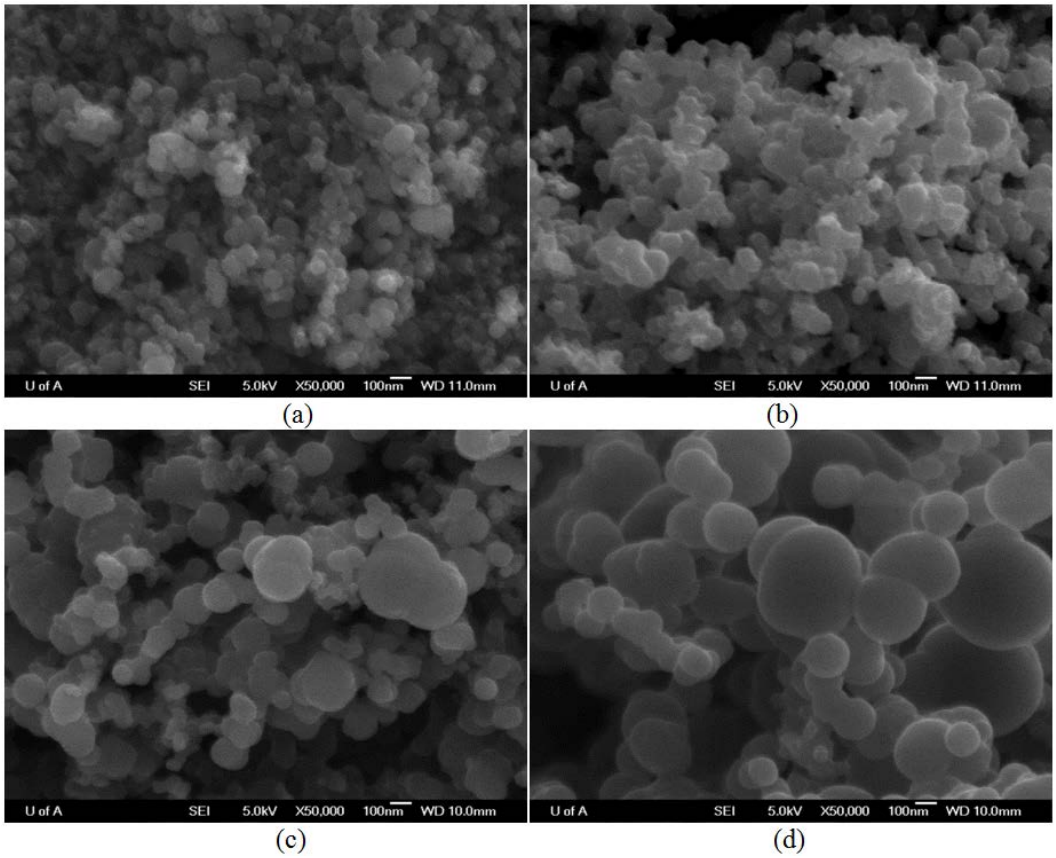

Figure 4.14: SEM images of soot particles formed at residence times of (a) 5 s, (b) 6.6 s, (c) 8.5 s, and (d) 12 s on stage 3 of the cascade impactor at 1200 °C.

Ma et al. [75] for coal-derived soot. They reported that the size of primary soot particles increased from 25 to 60 nm and that at high residence times the soot particles agglomerated to form clusters with sizes of 800 nm. However, Figure 4.14 shows that primary soot particles with sizes of around 25 nm were formed at a residence time of 5 s and that at the maximum residence time of 12 s the size increased to a maximum of around 300 nm. With an increase in the residence time, the primary soot particles had more time for surface growth and mass addition via reactions with acetylene and PAHs. The inert atmosphere also helped in the formation of larger soot particles.

4.3 Conclusions

In this work, the properties of the soot formed under different operating conditions by the pyrolysis of oil sand asphaltenes were analyzed. The important operating parameters were the feed particle size, pyrolysis temperature, and residence time. According to the particle size distribution, morphology, and elemental composition, it was clear that there was no effect of feed particle size on the characteristics of the soot formed. Temperature plays a major role in determining the yield, morphology, and hydrogen and sulfur contents of the soot. The yield of soot increased with increasing temperature over the range of temperatures examined. At low temperatures, tar was found to be mixed with soot, but the soot separated from tar had the same morphology as the soot formed at higher temperatures. At higher temperatures the tar was converted to soot or light gases. The presence of tar at low temperature confirmed that asphaltenes have a soot formation mechanism similar to that of coal. The size of the primary soot particles decreased with increasing temperature. The observed soot morphology is consistent with the soot inception and surface growth mechanism described. The hydrogen and sulfur contents in the soot decreased with increasing temperature as a result of the release of hydrogen sulfide. The size of primary soot particles increased with increasing pyrolysis residence time because of the extra time available for spherules to undergo

surface growth with acetylene and PAHs. Increasing the residence time had no effect on the hydrogen and sulfur contents of the soot. These experiments and analyses could have applications in designing industrial asphaltene gasification systems, where the gasification temperature is > 1300 °C and residence time is around 10 s.

Chapter 5

Metal Distribution in Soot*

5.1 Introduction

Removal of asphaltenes can greatly reduce problems associated with production, transportation and refining of crude oil [80]. Asphaltenes and oil sand coke have significant quantities of vanadium, nickel [United States Environmental Protection Agency (U.S. EPA) regulated elements] and sulfur which prevents their direct combustion. Most metals in bitumen are concentrated in asphaltene, mainly vanadium and nickel. Filby and Strong [81] observed that the majority (76.1%) of vanadium in the Athabasca bitumen is present in the asphaltene fraction. During combustion of asphaltene, vanadium present in fuel leads to the formation of vanadium pentoxide, which is toxic [82, 83] if emitted to the atmosphere, corrosive [84] for turbines when used in power generation, or a fouling concern [85] in asphaltene gasifier downstream equipment. Nickel present in asphaltene forms nickel sulfide during gasification and causes fouling in the downstream of the gasifier.

Pyrolysis of liquid droplets produces particles that are carbonaceous and/or metallic, whose typical sizes are comparable with those of the parent feed droplets [86]. Most of these particles appear as hollow riddled spheres, called cenospheres, which become fragmented as a result of thermal stresses and

*A version of this chapter has been published as "Distribution of Vanadium, Nickel, and Other Trace Metals in Soot and Char from Asphaltene Pyrolysis and Gasification" in *Energy and Fuels*, 2016, 30, 1605–1615.

attrition. However, some authors have also reported the presence of denser compact particles having sizes of the order of a few micrometers in the fly ashes produced during coal combustion [87, 88]. Larger particles with a micrometer size range can be captured more easily than those into the sub-micrometer range, which escape without any obstacle to the atmosphere.

The ash from asphaltene gasification is different as a result of the presence of V and Ni compared to ash containing Ca, Fe, Si, Al, K, Na, and Mg from coal and biomass gasification. Dunning and co-workers [89] reported that from 3 to 10% of vanadium in most vanadium-rich oils is present as vanadium-porphyrin complexes. Their studies of total vanadium and vanadium in the vanadyl form and as metal-porphyrin complexes show that from 1/3 to 1/2 of the volatile vanadium appearing in gas oils is both vanadyl and porphyrin in nature. Allouis et al. [90] investigated particulates emitted by two different heavy oil flames and revealed the presence of small full/solid particles, called plerospheres, whose composition is directly correlated to their dimensions. The metal concentration (Fe + V + Ni) increases as the plerosphere dimension decreases. The correlation between the particle size and its metal concentration is explained by the atomization process of a parent droplet with a high percentage of asphaltenic mesophase. Most parts of the metals are bound to this asphaltenic mesophase [91]. Thus, the metals could concentrate during the carbon oxidation, devolatilization, and depletion of the droplet itself.

During the fuel pyrolysis, the devolatilization takes place and the gases evolved may contain some trace metals in gaseous form at high temperatures. Part of the trace metals or inorganic matter associated with the fuel, mainly metal porphyrins, remains in the char itself. The trace metals liberated with light gases during pyrolysis may take part in the soot formation process, or they will associate with the soot particles formed during the cooling of these product gases in the downstream of the reactor. The trace metals retained in the char are liberated during the char oxidation/char gasification reactions.

If these trace metals are not covered or captured by the formed soot, then they may cause the fouling/erosion downstream of the gasifier. Ben et al. [85] investigated the deposition of layers on syngas cooler tubes downstream of the asphaltene gasifier. The fouling layers include a condensation layer of Ni_3S_2 and subsequent fouling layers composed of V_2O_3 and Ni_3S_2. The condensation layer consisted of about 80% Ni_3S_2, and the fouling layer consisted of about 70% V_2O_3. The major part of the deposit layer was compounds of V and Ni. Therefore, in the present study, the fate of V and Ni during the high-temperature process is also investigated in detail. It is important to characterize the particles evolved during the combustion or gasification of different fuels, with particular emphases on the particle morphology and the size distribution of potentially toxic elements. We should also try to concentrate the metals inside those particles that are easily captured, instead of being dispersed as finer aerosols. Understanding the trace metal distribution in char and soot during pyrolysis, partial oxidation, and gasification will help in increasing the efficiency of the entire asphaltene gasification process.

The asphaltene used for this study is resourced from a deasphalting unit that upgrades bitumen from Athabasca basin in northern Alberta, Canada. Asphaltenes consist of trace amounts of V and Ni in addition to carbon, hydrogen, sulfur, nitrogen, and oxygen. The proximate and ultimate analyses of asphaltenes are shown in Table 3.2. The presence of trace elements in asphaltene was determined using the inductively coupled plasma mass spectrometry (ICP-MS) technique with a Thermo Scientific iCAP Q. In this analysis, 50 mg of sample was digested in 3 mL of nitric acid in a microwave digester. After digestion, the contents were diluted with nanopure water and then mixed with 1% HNO_3 before it is analyzed. The quantities of major elements (>2 ppm) and the quantities of minor elements (<2 ppm) are shown in Figure 5.1 separately. Iron, phosphorus, calcium, and aluminum appear in noticeable amounts after V and Ni. Asphaltenes were solid at room temperature and start melting at around 300 °C. The milled and sieved solid asphaltene was

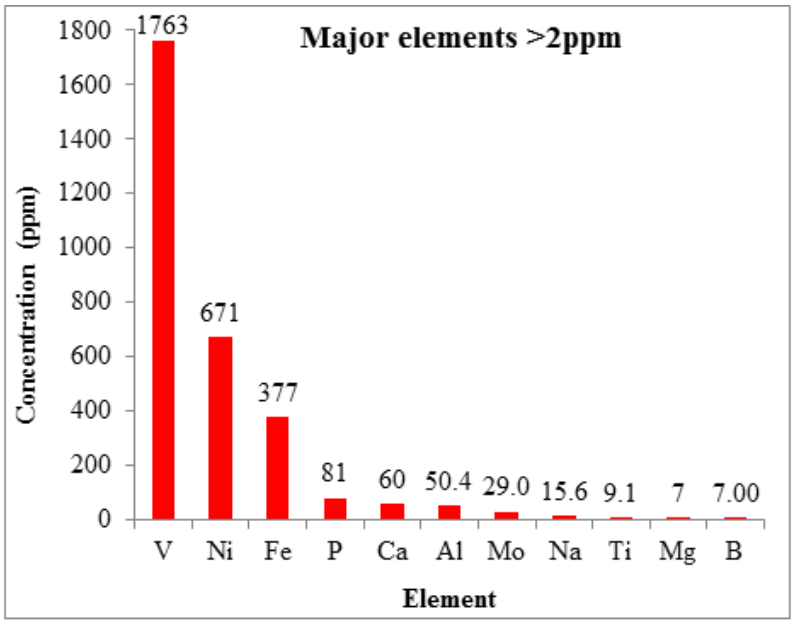

(a)

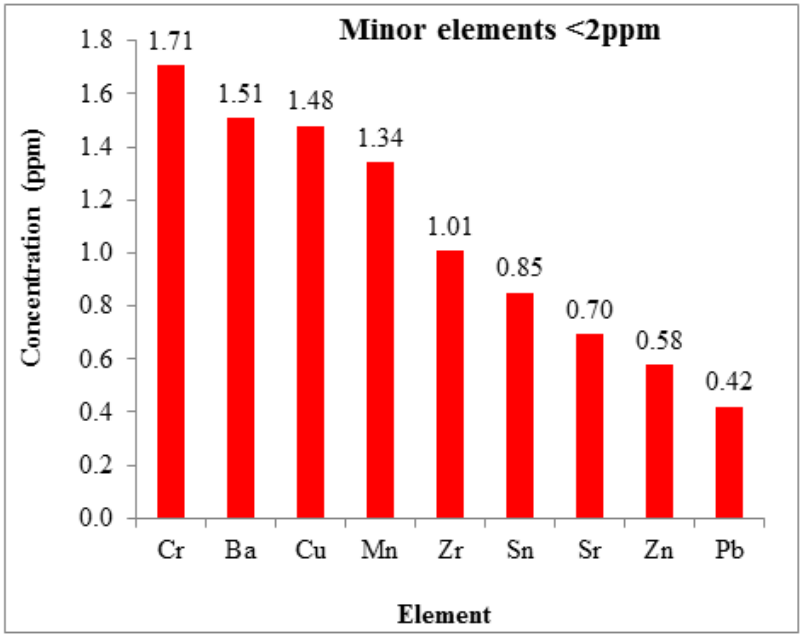

(b)

Figure 5.1: Trace metals present in asphaltene analyzed using ICP-MS.

fed to the reactor. The feed size range used for all of the experiments was between 150 and 212 μm, which was in the same range as that of the industrial atomizer.

Unlike pyrolysis experiments, which are conducted with only nitrogen as the carrier gas, partial oxidation experiments are conducted with a mixture of air and nitrogen as the carrier gas. Nitrogen was needed for maintaining the total carrier gas flow constant to keep the same residence time as that of the pyrolysis experiments. The amount of air is varied to vary the percentage of stoichiometric oxygen available for the combustion reaction. Lastly, steam gasification is carried out to check the effect of reactant steam on the trace metal behavior in char and soot formed. Here, the carrier gas nitrogen was also sent through the feeder line to carry the particles to the reactor. A mixture of air and steam was introduced to the end of the feeder tube close to the reactor.

5.2 Entrained-flow Reactor Experiments

5.2.1 Pyrolysis

During the high-temperature pyrolysis, the feed asphaltene particles are fragmented to smaller particles during the liberation of volatile species. The average char particle size is around 50 μm as seen in the SEM image of char formed at 1400 °C in Figure 5.2. The morphological and structural analyses of the char formed during pyrolysis are explained in a previous study [70]. The fundamental unit of soot agglomerates is called spherules, which are 10–50 nm in size [36]. Some of the soot particles are deposited on the surface of the char particles, as shown in panels b and c of Figure 5.2. A big char particle and its magnified top surface with fine soot particles on it, individual as well as agglomerates, are clearly visible. Soot agglomerates consist of clusters or chains of spherules. Various analysis techniques were used to quantify the trace metal distribution in char and soot, including SEM-energy-dispersive X-ray spectroscopy (EDX), X-ray fluorescence (XRF), X-ray diffraction (XRD),

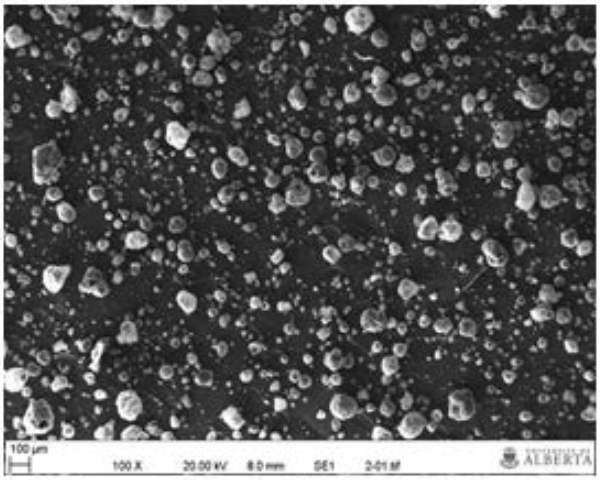

(a)

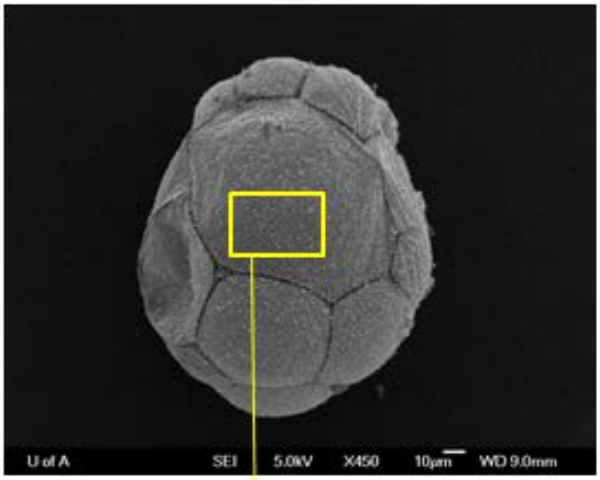

(b)

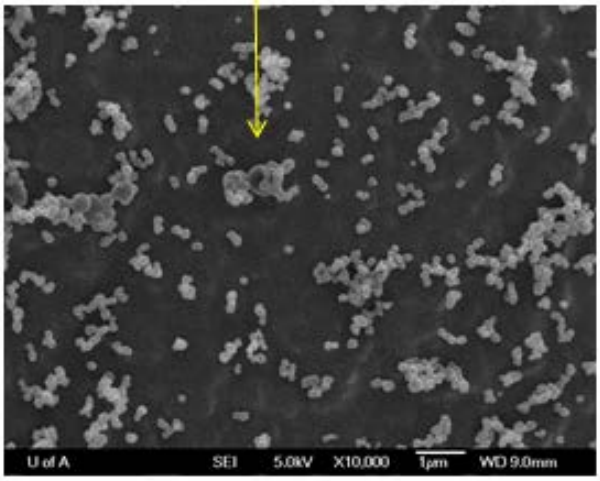

(c)

Figure 5.2: (a) Pyrolysis char fragmented at 1400 °C and (b and c) soot observed on the top surface of the char particle formed at 1000 °C.

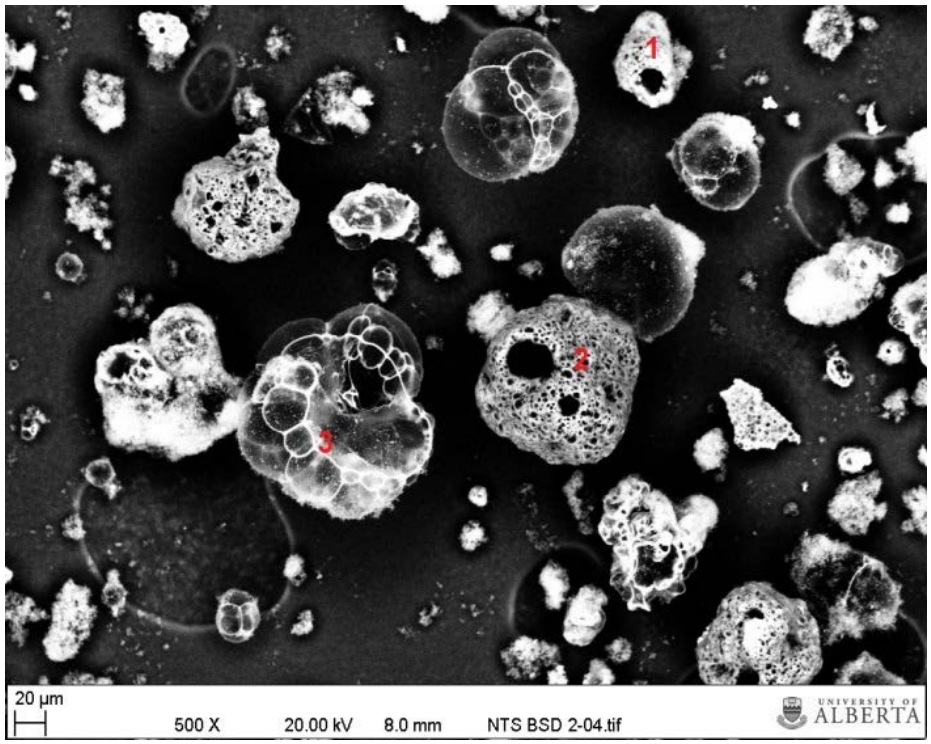

Figure 5.3: Back-scattered image of the char from pyrolysis at 1400 °C.

X-ray photoelectron spectroscopy (XPS), ICP-MS, and transmission electron microscopy (TEM). The XRD results were having a lot of noise as a result of the high concentration of amorphous carbon present in the sample, and the XPS results were not quite useful because of the very low concentration of the elements of interest. Therefore, the XRD and XPS results are not discussed in the section.

The morphological and elemental analyses of char and soot particles were first examined using field emission scanning electron microscopy (FE-SEM, JEOL JSM-6301F). The JSM-6301F is a high-performance general purpose field emission scanning electron microscope with a high resolution of 1.5 nm (6.0 nm at 1 kV). Along with a variety of auto functions, the JSM-6301F is also an analytical scanning electron microscope with the addition of a back scatter detector and an EDX detector by Princeton Gamma-Tech. The back-scattered images of the char and soot formed during the pyrolysis at 1400 °C are shown

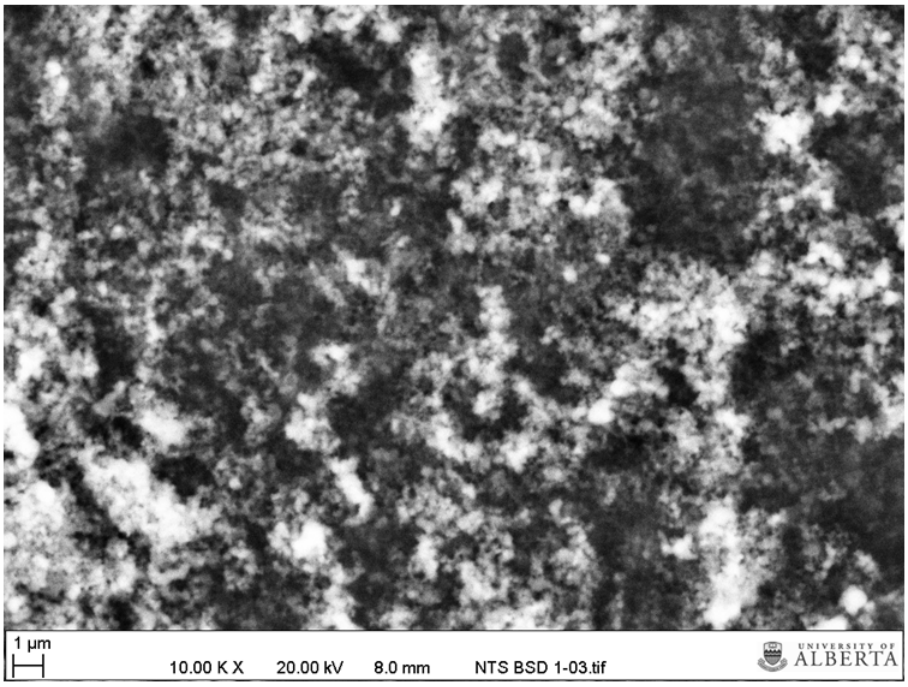

Figure 5.4: Back-scattered image of soot from pyrolysis at 1400 °C.

in Figure 5.3 and Figure 5.4, respectively. EDX is used to check the trace metal content present. Three points in the char image with different particle morphologies were identified for the EDX analysis, and the results are shown in panels a–c of Figure 5.5. All three points analyzed confirmed the presence of V and Ni, which are the main trace metals present in the feed asphaltene. The values of Si might be over predicted as a result of contamination from an insulation material used to seal the reactor at the top during the experiments. Because the soot shown in Figure 5.4 appears uniform in the entire area of the image, an area analysis is conducted with EDX for the inorganic content, and the results are shown in Figure 5.5. Interestingly, the EDX analysis of soot particles did not show any V and Ni. This absence may be due to either the large quantity of amorphous carbon present in the sample or the V and Ni present as organometallic form in the soot. The TEM analysis of the pyrolysis soot, as shown in the previous chapter also could not detect V or Ni in the soot collected from the pyrolysis experiment.

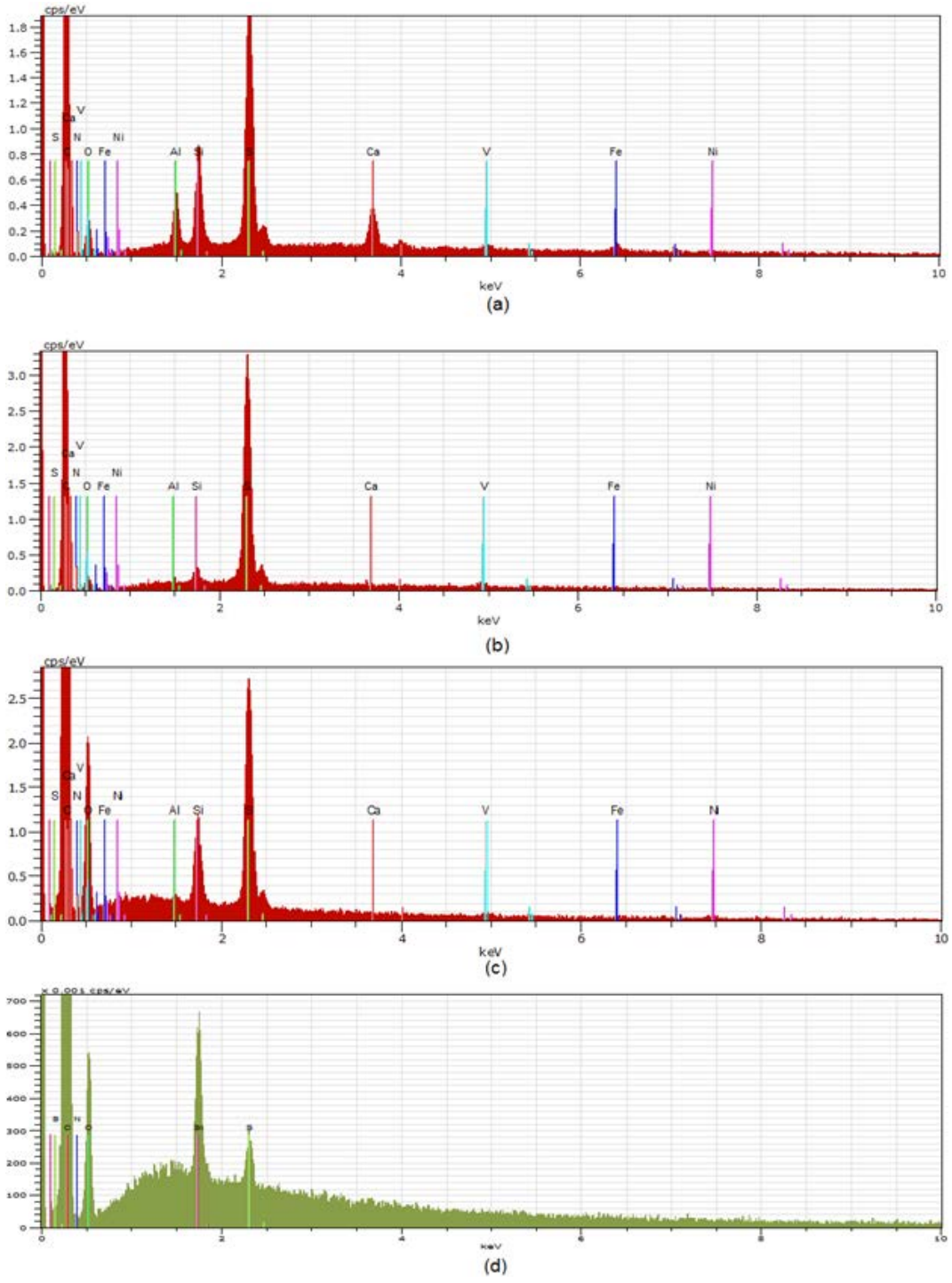

Figure 5.5: EDX elemental analysis: (a) char point 1 of Figure 5.3, (b) char point 2 of Figure 5.3, (c) char point 3 of Figure 5.3, and (d) soot entire area of Figure 5.4.

Because the EDX analysis of soot did not show any trace metal content, ICP-MS is expected to be a better technique for soot. However, in the case of char, the point analysis showed the presence of trace metals, which is a semi-quantitative result. However, this is not the bulk analysis. Therefore, Thermo Scientific iCAP Q ICP-MS was used for the analysis of char and soot collected at three different pyrolysis temperatures. As the temperature increases, the quantity of major trace metals, such as V and Ni, decreases for both char and soot, as shown in Figures 5.6 and 5.7. This decrease may be due to more liberation of V and Ni elements/compounds in the gas phase during the high-temperature pyrolysis. The increased liberation of these metals from the feed asphaltene is expected at higher temperatures, but the inability of soot to capture these more available metals is interesting. The trace metals that are associated with soot may escape from the soot at higher temperatures, and they may be deposited on the reactor walls or downstream tube walls, causing fouling/erosion. Zinc, which is a minor element in the feed asphaltene (0.58 ppm), is detected as a major element in the char (Figure 5.7), and it varies with the temperature in a different trend compared to other elements. Also considering the fact that Zn is not detected in soot (Figure 5.6), Zn obtained in the ICP-MS analysis of the char could be neglected, expecting some kind of contamination. Figure 5.8 shows that, at 1000 and 1200 °C, soot contains more V and Ni compared to char but, at 1400 °C, char contains more. This inverse change is also related to the decrease in V and Ni with respect to the temperature. At higher temperatures, such as 1400 °C, the liberation of elements, such as V and Ni, from the char particle is high and the soot is not able to capture these efficiently.

To determine the elemental composition of the ash present in asphaltene, soot, and char, the excess carbon present was burned in a thermogravimetric analyzer to decrease the carbon content. The set temperature for the burning was 500 °C, and the heating rate was 10 °C/min. The collected ash of asphaltene, soot, and char was analyzed with XRF. The Ametek EDAX Orbis PC

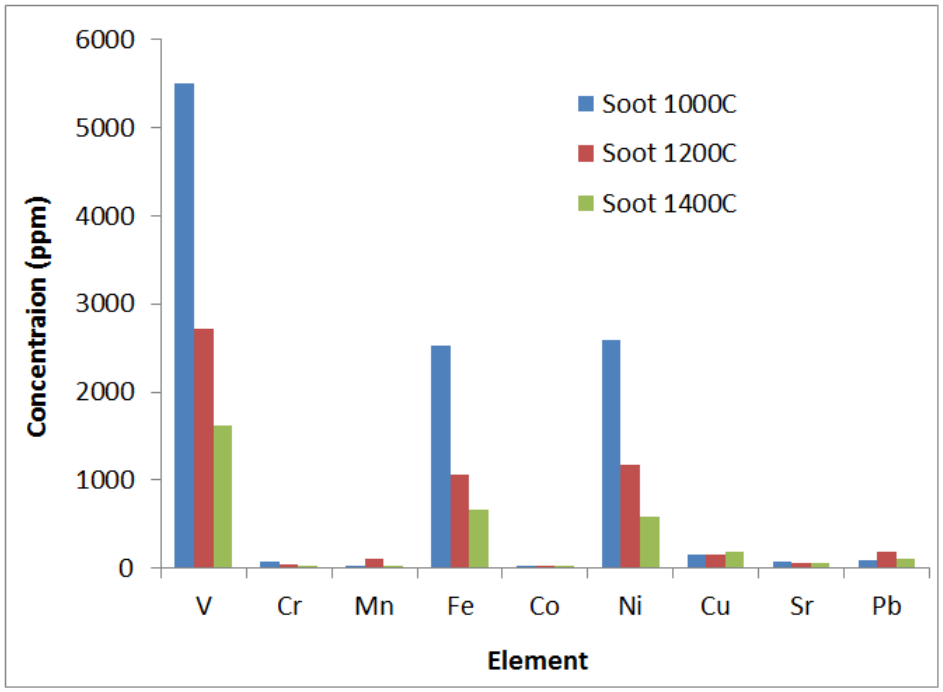

Figure 5.6: Trace metal content of soot formed during pyrolysis at 1000, 1200, and 1400 °C.

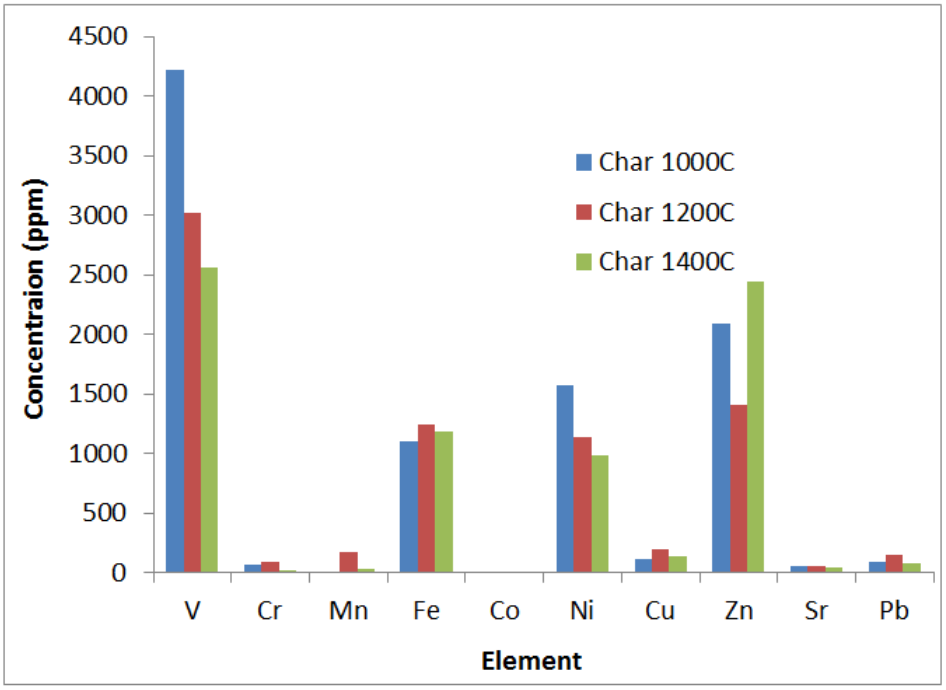

Figure 5.7: Trace metal content of char formed during pyrolysis at 1000, 1200, and 1400 °C.

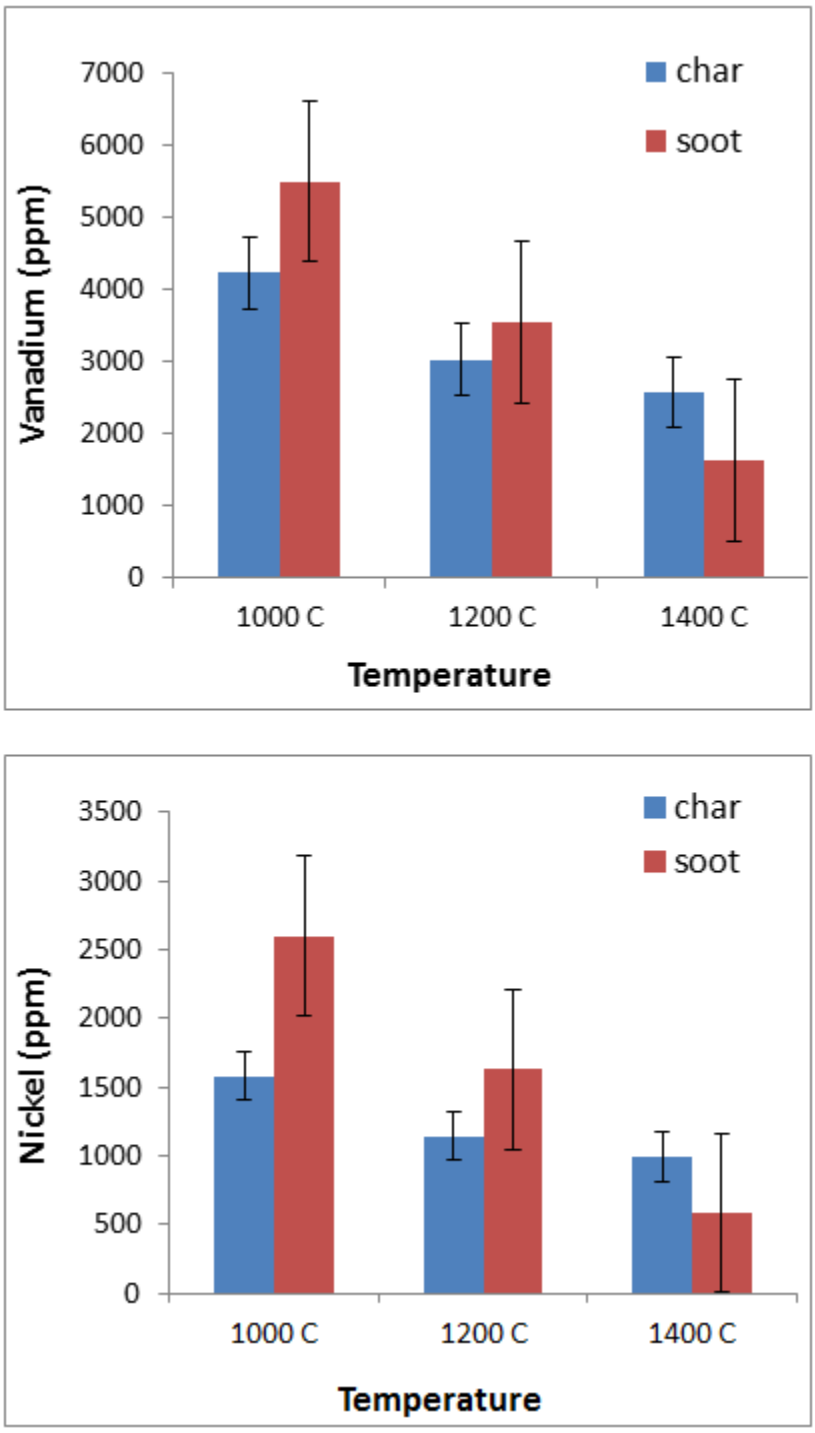

Figure 5.8: Vanadium and nickel contents of soot and char formed during pyrolysis at 1000, 1200, and 1400 °C.

Table 5.1: XRF Elemental Analyses of Asphaltene Ash and Pyrolysis Char Ash

Element	**Asphaltene Ash** wt%	**Char Ash 1000 °C** wt%	**Char Ash 1200 °C** wt%	**Char Ash 1400 °C** wt%
Al	0.26	0.35	0.44	0.42
Si	0.86	1.16	1.46	1.38
P	0.17	0.74	9.16	0.99
S	6.49	13.93	15.21	15.73
K	0.27	1.21	5.14	3.03
Ca	1.63	8.69	6.23	14.05
Ti	0.64	1.40	2.48	1.89
V	60.93	50.22	32.36	35.28
Cr	0.47	0.34	1.75	0.63
Fe	1.68	5.51	6.27	11.52
Co	0.13	0.09	0.56	0.14
Ni	26.05	15.42	12.67	12.91
Cu	0.25	0.54	1.24	1.72
Zr	0.18	0.42	5.03	0.30
Total	100	100	100	100

Table 5.2: XRF Elemental Analysis of Pyrolysis Soot Ash

Element	**Soot Ash 1000 °C wt%**	**Soot Ash 1200 °C wt%**	**Soot Ash 1400 °C wt%**
Al	0.48	0.35	0.51
Si	1.2	1.14	1.70
P	2.0	1.52	1.43
S	28.56	20.97	14.27
K	1.23	0.82	1.35
Ca	10.82	18.98	8.22
Ti	0.85	1.56	1.31
V	41.29	39.96	51.81
Cr	0.21	0.07	0.23
Fe	4.88	3.67	4.83
Co	6.71	9.88	13.68
Ni	1.34	0.77	0.40
Cu	0.11	0.10	0.06
Zr	0.32	0.21	0.22
Total	100	100	100

energy-dispersive-instrument with 2 mm collimators was used for XRF. In this technique, powder samples were sandwiched between layers of ultra thin mylar film, which is then secured in a sample cup. This securing allows for drawing a vacuum required for accurate analysis. Table 5.1 shows the XRF results of asphaltene ash and ashes of pyrolysis chars formed at three different temperatures. Table 5.2 shows the XRF results of pyrolysis soot ash. The results of asphaltene ash clearly show that the major constituents of asphaltene ash are V and Ni. Even after burning the sample at 500 °C, a good amount of V and Ni stays in the ash. That confirms the strong association of these elements in the core of the asphaltene molecule as metal porphyrins. For char ash, the amount of V and Ni decreases with an increase in pyrolysis temperatures similar to the results of ICP-MS. The quantity of V and Ni might have been affected by some contamination of the samples too. The results of the soot ash clearly show the escape of Ni during the burning of soot at 500 °C, and Ni quantities are nearly 1%. The V element is still the major part in the soot ash similar to the char ash. Therefore, it is clear that Ni present in char and soot is of different types. The char may contain Ni as metal porphyrins, and it is not becoming liberated easily during the ashing process, whereas the soot may contain some Ni compounds, such as sulfides, which become condensed on top of the soot particles. In the case of V, it is organically bound to the char as well as the soot structure and not easily evolved from it. V in the char is liberated during the char gasification reactions in the gasifier and may or may not associate with soot in the downstream of the reactor.

5.2.2 Partial Oxidation

The partial oxidation experiments were carried out with 10% stoichiometric oxygen and 34% stoichiometric oxygen. The set temperature of partial oxidation experiments was kept constant at 1300 °C. The mass balance for the partial oxidation experiments (Figure 5.9) shows that an increase in the stoichiometric oxygen content decreases the soot yield from 8.73 to 6.72%, which

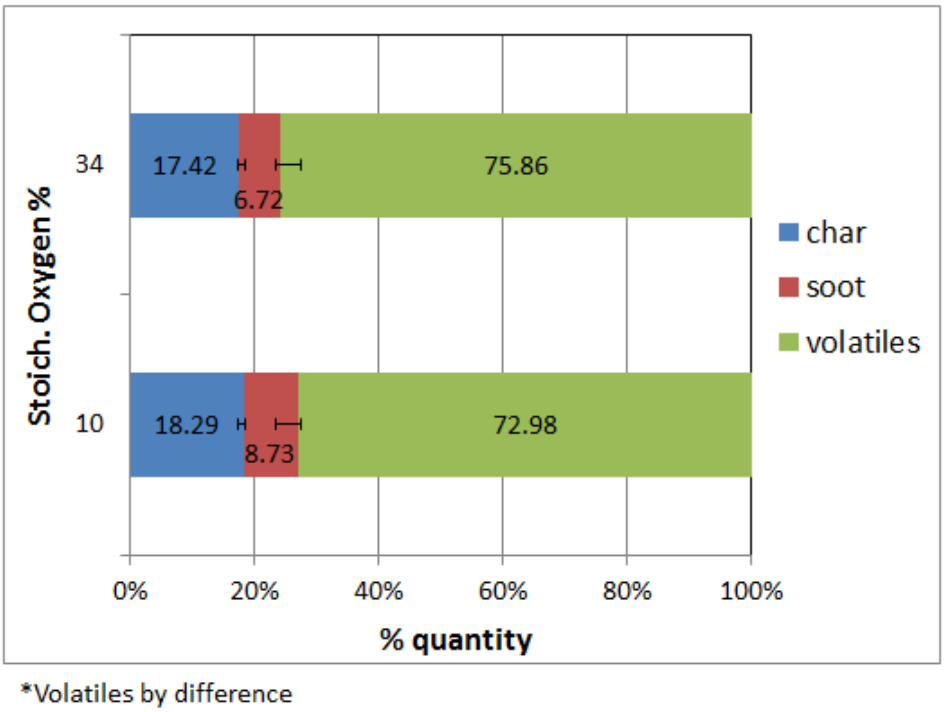

Figure 5.9: Mass balance of partial oxidation experiments.

is expected as a result of the increase in the oxygen/carbon ratio. Chen et al. [49] also observed a decrease in the concentration of soot with an increase in the O/C ratio during the gasification of the coal-biomass blend in an atmospheric fluidized bed. Similar to the pyrolysis soot, partial oxidation of soot was also first analyzed with SEM. Two back-scattered images of the soot shown in Figure 5.10 look uniform, and the absence of any brighter spots for trace metals is clear. An EDX analysis of a major area in Figure 5.10 did not show any presence of V or Ni. This absence may be due to the very low concentration of V and Ni and also may be due to the association of V and Ni in the soot as organometallic form.

TEM analysis of the soot showed two different size ranges for the soot particles, one with an average spherule size of 10 nm and another with that of 100 nm (Figure 5.11). As a result of the presence of two different morphologies for the soot particles, the association of trace metal micro crystals is expected.

Table 5.3: XRF Elemental Analyses of Partial Oxidation Char Ash and Soot Ash

	Char Ash		**Soot Ash**	
Element	**10% O2**	**34% O2**	**10% O2**	**34% O2**
	wt%	**wt%**	**wt%**	**wt%**
Al	0.33	0.39	1.52	0.71
Si	1.08	1.30	5.03	2.36
P	0.54	1.45	2.22	0.99
S	17.63	36.97	7.19	70.75
K	1.46	1.38	7.42	2.79
Ca	10.96	13.76	2.05	1.70
Ti	1.38	1.24	0.29	0.25
V	41.99	27.98	61.66	15.39
Cr	0.51	0.64	0.35	0.44
Fe	7.41	6.14	2.22	1.26
Co	0.16	0.05	0.18	0.14
Ni	15.17	6.81	8.59	2.05
Cu	1.16	1.55	0.41	0.27
Zr	0.21	0.35	0.88	0.90
Total	100	100	100	100

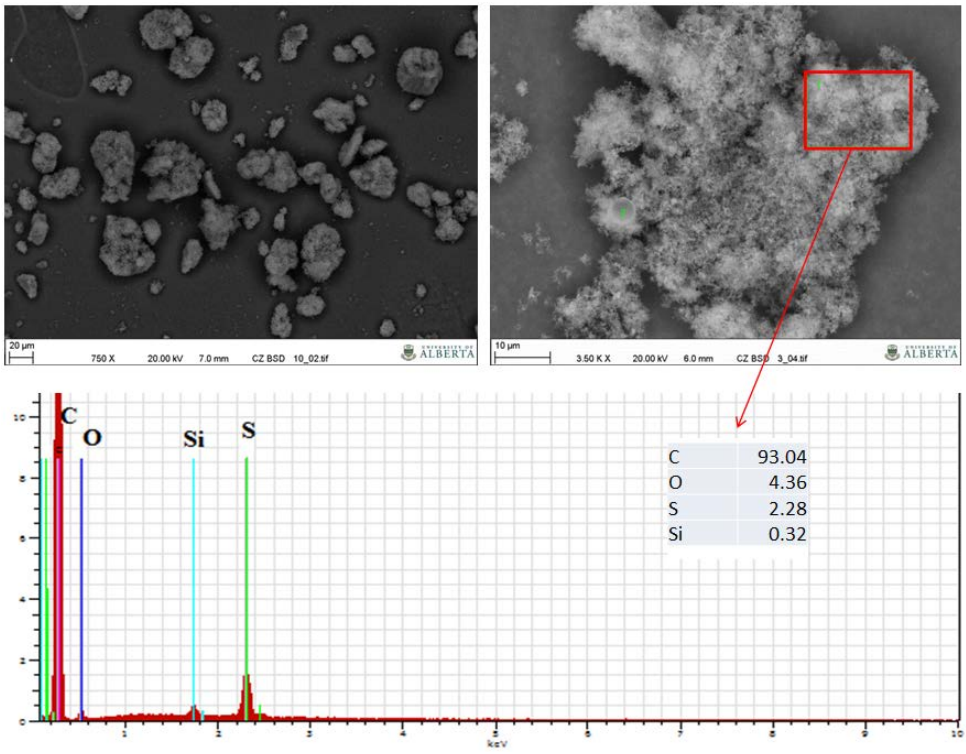

Figure 5.10: Back-scattered SEM image.

However, the EDX analysis of both the areas did not show any presence of V and Ni (Figure 5.12). The soot and char formed during the partial oxidation did not show any trace metal content as a result of its low concentration as well as high carbon concentration. To avoid this excess carbon present and to check the other elements present, soot and char are burned in a thermogravimetric analyzer to decrease the carbon content. The set temperature for the burning was 500 °C, and the heating rate was 10 °C/min. After burning out the excess carbon, the remaining material was ash. A back-scattered image (Figure 5.13) of this soot ash showed many bright areas, which are confirmed to contain V and Ni with EDX analysis, as shown in Figure 5.14. Similar to soot ash, char ash was also analyzed with back-scattered SEM (Figure 5.15) and EDX analysis (Figure 5.16), which confirmed the presence of trace metals in it. Because the ICP-MS analysis was time-consuming and more costly, it is not undertaken for partial oxidation char and soot. For composition analysis, XRF is used for the ash made from soot and char. The results of the elemental

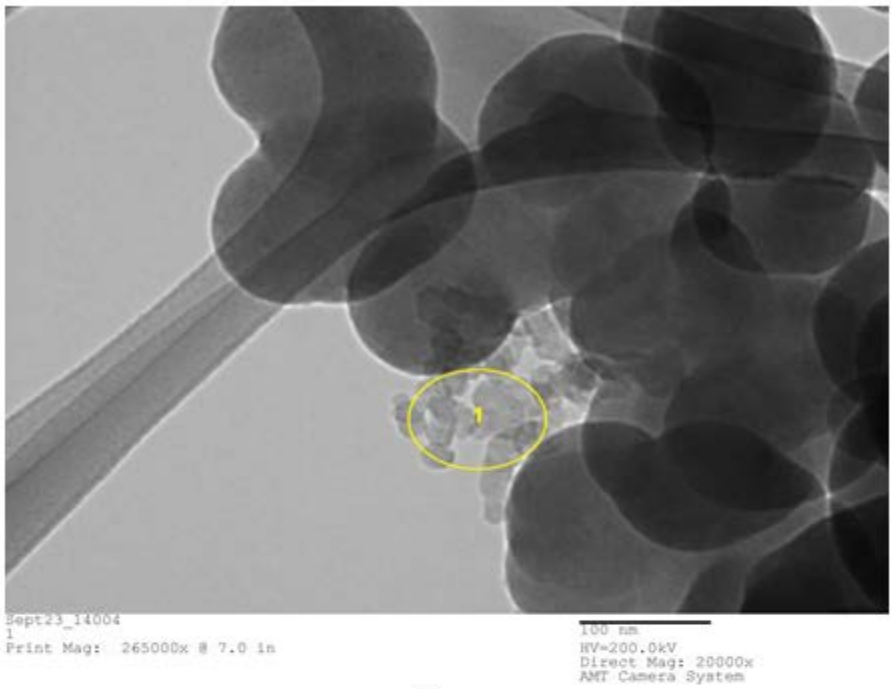

(a)

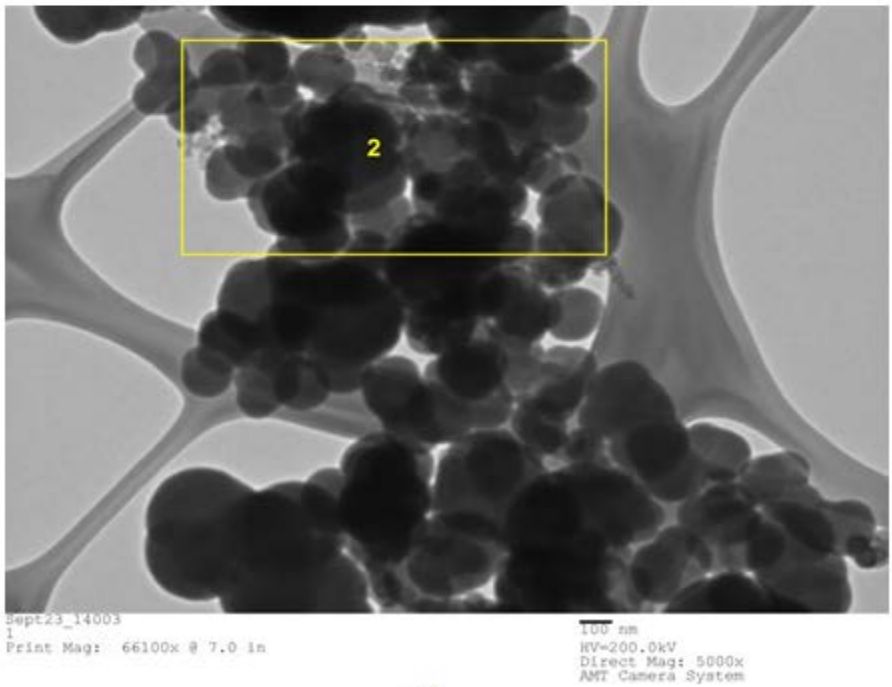

(b)

Figure 5.11: TEM analysis of the soot from partial oxidation.

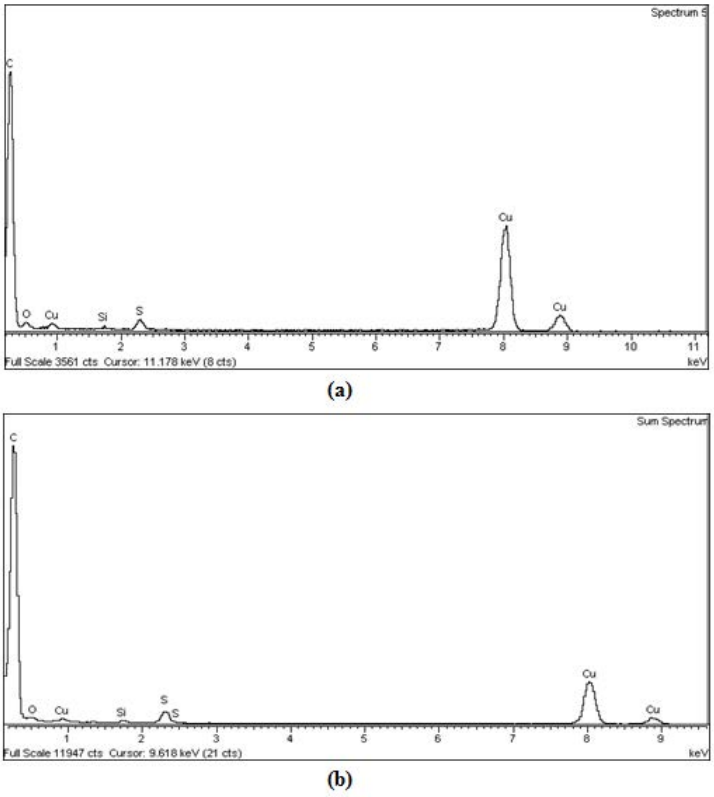

Figure 5.12: EDX analysis of areas 1 and 2 marked in Figure 5.11.

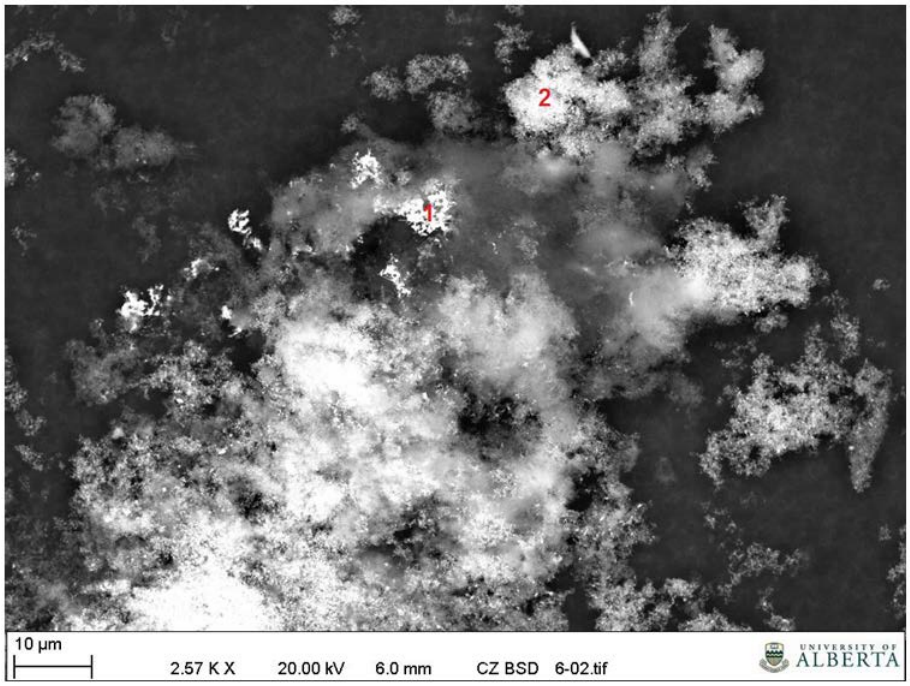

Figure 5.13: Back-scattered image of the partial oxidation soot ash.

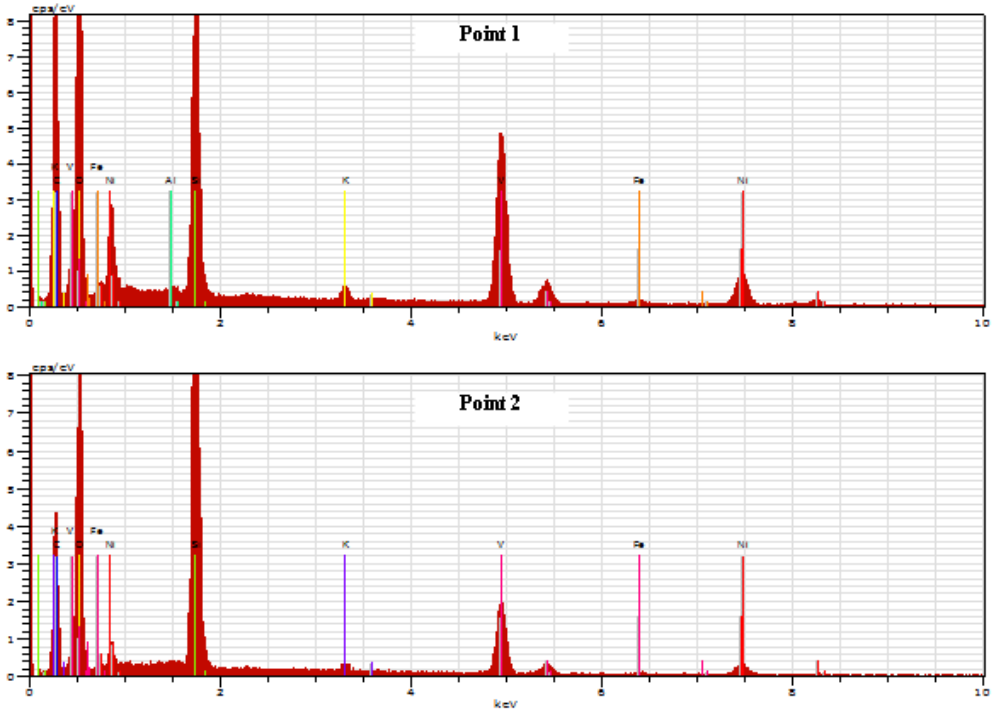

Figure 5.14: EDX analysis of the partial oxidation soot points marked in Figure 5.13.

XRF analysis are shown in Table 5.3. It is found that the V and Ni contents in both the char ash and soot ash decrease with an increase in stoichiometric oxygen in the feed. With higher content of oxygen available for reaction, the asphaltene react more with oxygen resulting in liberation of more metals. However, the extra metals liberated from char is not captured successfully by soot. Therefore, the metal content in soot also decreasing In addition, the condensation of some elements might not take place on the surface of the soot as a result of the oxygen atmosphere.

5.2.3 Steam Gasification

The steam gasification experiments were conducted at 1300 °C because that temperature is close to the industrial gasifier operating temperature. The weight percentages of steam to fuel used were 22 and 41%. The soot collected from the steam gasification experiments contained moisture, which is the un-

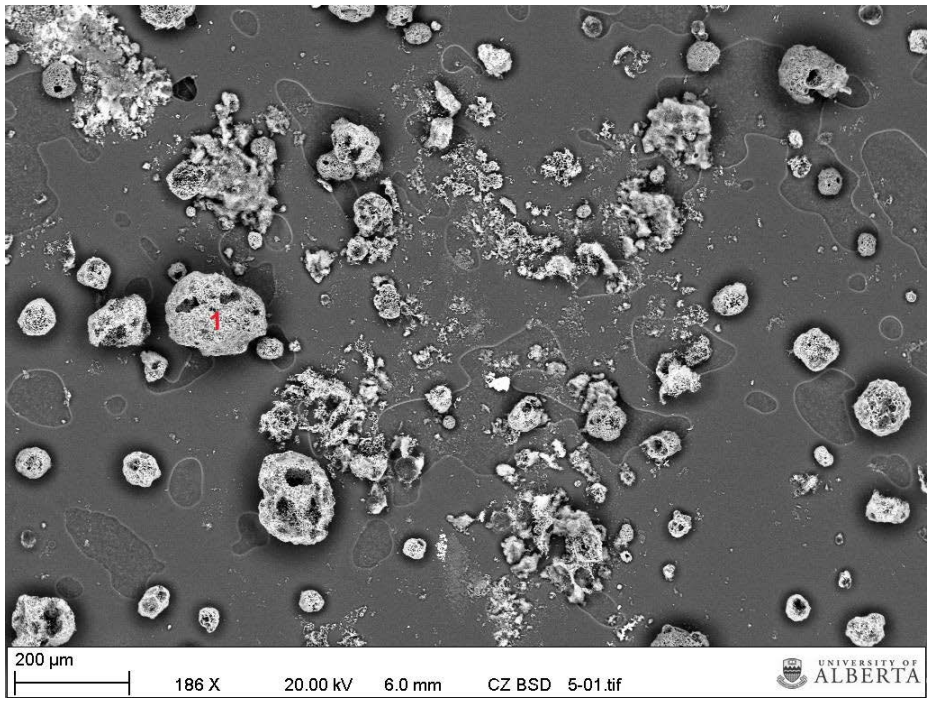

Figure 5.15: Back-scattered image of the partial oxidation char ash.

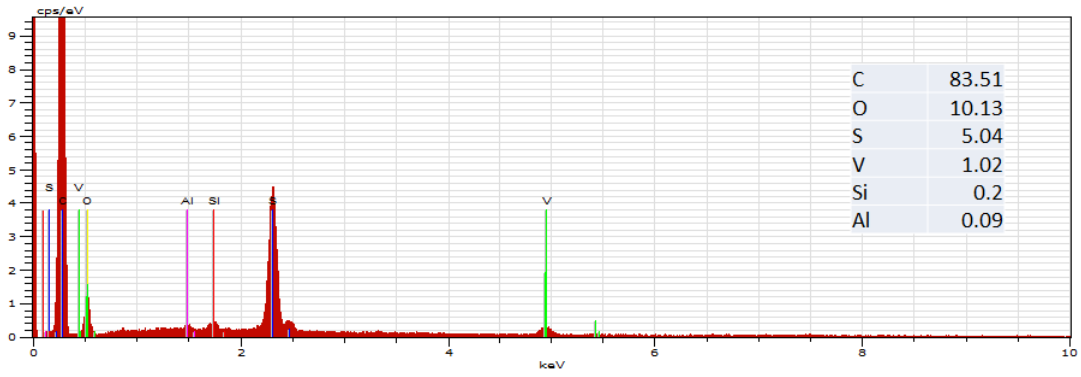

Figure 5.16: EDX analysis of the partial oxidation soot points marked in Figure 5.15.

Table 5.4: XRF Elemental Analyses of Steam Gasification Char Ash and Soot Ash

	Char Ash		**Soot Ash**	
Element	**22% steam**	**41% steam**	**22% steam**	**41% steam**
	wt%	**wt%**	**wt%**	**wt%**
Al	0.35	0.46	0.77	0.55
Si	1.17	1.51	2.55	1.81
P	1.01	1.51	6.39	4.28
S	11.16	13.82	35.09	19.17
K	0.91	1.57	2.21	2.91
Ca	6.68	7.08	7.34	9.63
Ti	1.35	1.32	0.43	0.60
V	46.37	52.39	31.83	44.21
Cr	0.56	0.16	0.77	0.31
Fe	12.98	4.93	6.56	5.73
Ni	16.95	14.65	4.01	9.08
Cu	0.28	0.34	0.73	0.38
As	0.05	0.06	0.27	0.30
Zr	0.18	0.19	1.07	1.04
Total	100	100	100	100

reacted steam condensing at the downstream of the reactor. The presence of moisture in the soot may alter the original morphology of the particles. Therefore, SEM and TEM were not used for the analysis. Mainly XRF analysis of the ash of soot and char was conducted for steam gasification experiments. The ashing of the char and soot to remove the excess carbon is already mentioned in the previous sections. Table 5.4 shows the XRF analysis results of the char ash and soot ash. The V content of both char ash and soot ash increases with the increase in the steam/fuel weight ratio. The Ni content slightly decreases in char with the increase in the steam/fuel ratio, but the Ni content increases to more than double in soot ash with the increase in the steam/fuel ratio. The increase in the Ni content for higher steam percentage may be due to the extra condensation on the surface of soot particles in the presence of steam in the reactor atmosphere.

5.3 Soot Formation in an Industrial Gasifier

Through the upgrading and gasification processes that convert the heavy bitumen hydrocarbons to more useful forms, the metals in the crude become concentrated in the gasifier feed and subsequently in the gasifier soot. The bitumen in the Canadian oil sands contains vanadium, nickel, and other metals in significantly larger quantities than occur in most other oils. Duing gasification, both petcoke and heavy oils produce particulate matter which is entrained and must be removed from the raw syngas product. The entrained particular matter contains unconverted carbon, fused ash from solid feedstocks, and fused trace metals found in heavy oils. The syngas from the gasifier passes through a syngas cooler for recovering sensible heat to produce steam. The volatile species, such as sodium, potassium, chlorine, fluorine and sulfur, pass through the gasifier with the syngas. The particulate matter evolved during the gasification process causes fouling in the syngas cooler tubes with other inorganic matter present in it over a long operational period.

The removal of the particulate matter from the syngas is normally accomplished using a water scrubber attached to the downstream of the syngas cooler. The resultant soot slurry from the scrubber is delivered to filter presses for recovery and recycling of the scrubber water, and solids concentration of the soot. Soot slurry does not dewater easily, and exhibits very high viscosities at very low (e.g. $< 5\%$) solids concentrations. Typical Shell gasification process units exhibit around 17–20% solids content in soot cake from filter press. Higher carbon conversion efficiency is achieved by recovering and recycling unconverted carbon to the gasifier. The soot-metal cake recovered can be sold into the metals reclamation industry for the recovery of metals.

The samples analyzed here includes the fouling deposit from the syngas cooler and soot cake and soot water samples collected from the industrial asphaltene gasification set up. The feedstock for this gasifier is the same asphaltene which is used for the lab scale entrained-flow reactor experiments. The gasification occurs by partial oxidation using pure oxygen and steam. The weight ratio of oxygen to asphaltene is 1:1, and the weight ratio of steam to asphaltene is around 0.5. The process pressure is 6.5 MPa, and the produced syngas has a temperature exceeding 1300 °C. The syngas cooler is of the fire-tube type, having multiple coils spiraled upwards while submerged in a water bath. The tubes have a number of size reductions to maintain a velocity, so as to ensure that soot and ash particles are conveyed through the coils with manageable fouling and acceptable erosion/corrosion. First half of the cooler tube length was affected by high temperature corrosion, whereas the second half was covered with fouling deposits of different layers. Fouling deposit from the second half of the syngas cooler was collected as samples for the purpose of examination.

5.3.1 Syngas Cooler Fouling Deposit

The fouling deposit containing tubes were dipped in epoxy and hardener to stabilize the deposit. These set samples were cross sectioned into slices with

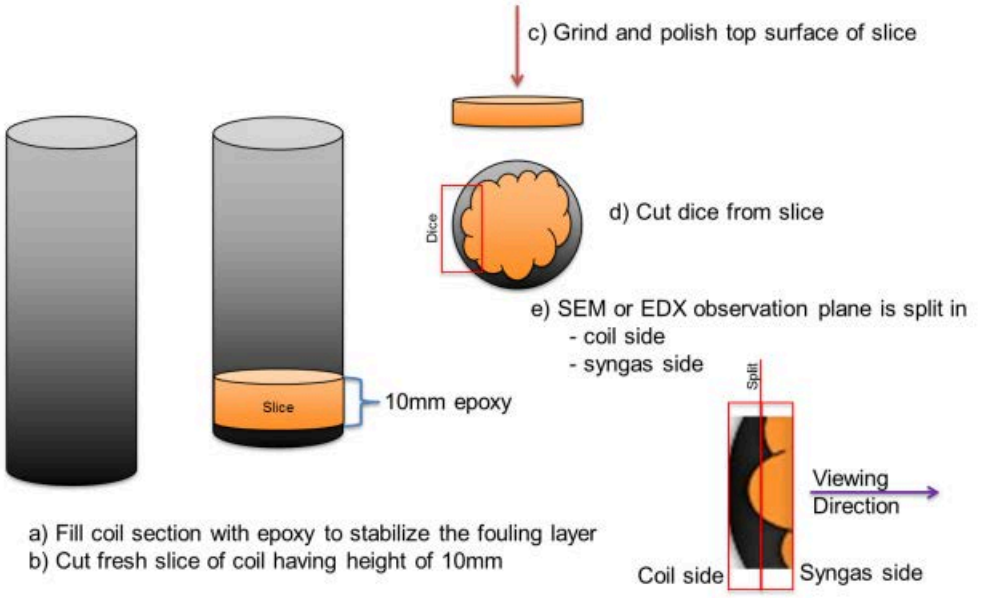

Figure 5.17: Fouling deposit sample preparation procedure for SEM.

a 10 mm height and finely polished using standard reflective light polishing procedures, then cut into small dices as shown in Figure 5.17 [85]. The polished sample prepared using epoxy is analyzed using scanning electron microscopy (SEM) and energy-dispersive X-ray spectroscopy (EDX) mapping to determine the deposit character morphology and chemistry. It is done by field-emission scanning electron microscopy (FE-SEM) using a JEOL 6301F scanning electron micro-scope, which provides high-resolution digital images of surface textures and microstructures at magnifications ranging from 20X to 250000X.

The deposit is of larger thickness and difficult to complete the EDX mapping in a single stretch. Therefore, the total thickness is divided into four parts and later the results were attached together for better understanding. The EDX mapping colors represent different elements defined in the legends. Figure 5.18 shows the BSE and EDX mapping of first, second, third and fourth part of deposit from left to right. The left yellow area represents the tube material followed by the black spalling which occurs due to the formation of an inter-

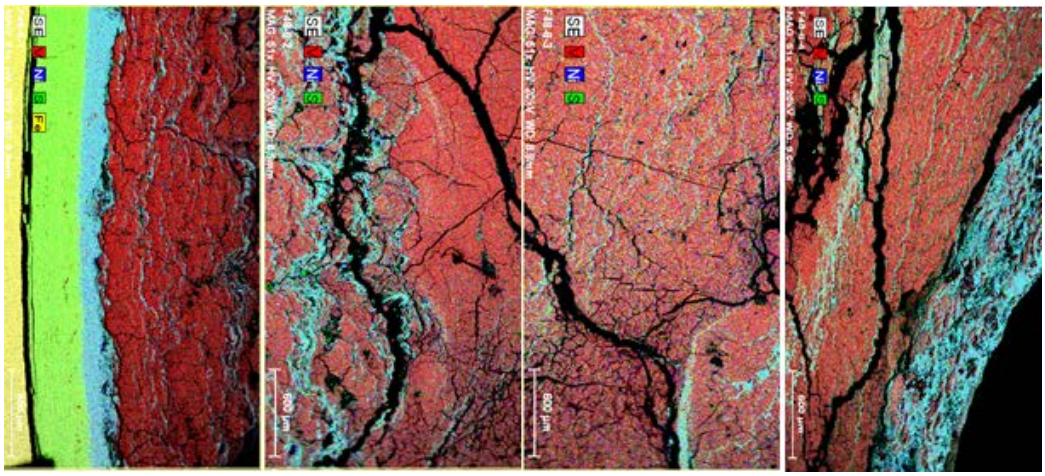

Figure 5.18: BSE and EDX mapping of first, second, third and fourth part of deposit (from left to right, leftmost being the tube material).

facial product, which may possess a different crystal structure with a distinct density change and/or a substantially different thermal expansion coefficient from the matrix. The greenish layer represents the corrosion layer and the blue color represents the Ni_3S_2 layer. Ni and V seem to be uniformly distributed on the outer section of deposit. The molecular formulas mentioned here are calculated by weight ratio of elements - in reality, these might be present, but not necessarily in this stoichiometric ratio shown. The fouling deposit contained 3-4 percent of carbon and the rest is mainly Ni_3S_2 and V_2O_3/V_2O_5.

5.3.2 Soot Water and Soot Cake

Ultimate analysis of the soot cake showed that it contains 50.6 % carbon, 1.17 % hydrogen, 0.77 % nitrogen and 3.47 % sulfur. The ash content of the soot cake was found to be around 30% dry basis. Table 5.5 lists the XRF results of soot cake which shows the soot cake has lower content of Ni and comparable V when compared to the fouling samples. This indicates most Ni_3S_2 condenses and deposits in the syngas cooler because of its low melting point and high viscosity. As for V_2O_3, it shows less preference to deposit on the tube or carried away by syngas. The higher concentration of sulfur in soot cake can be ascribed to the absorption of sulfurous gases by the soot.

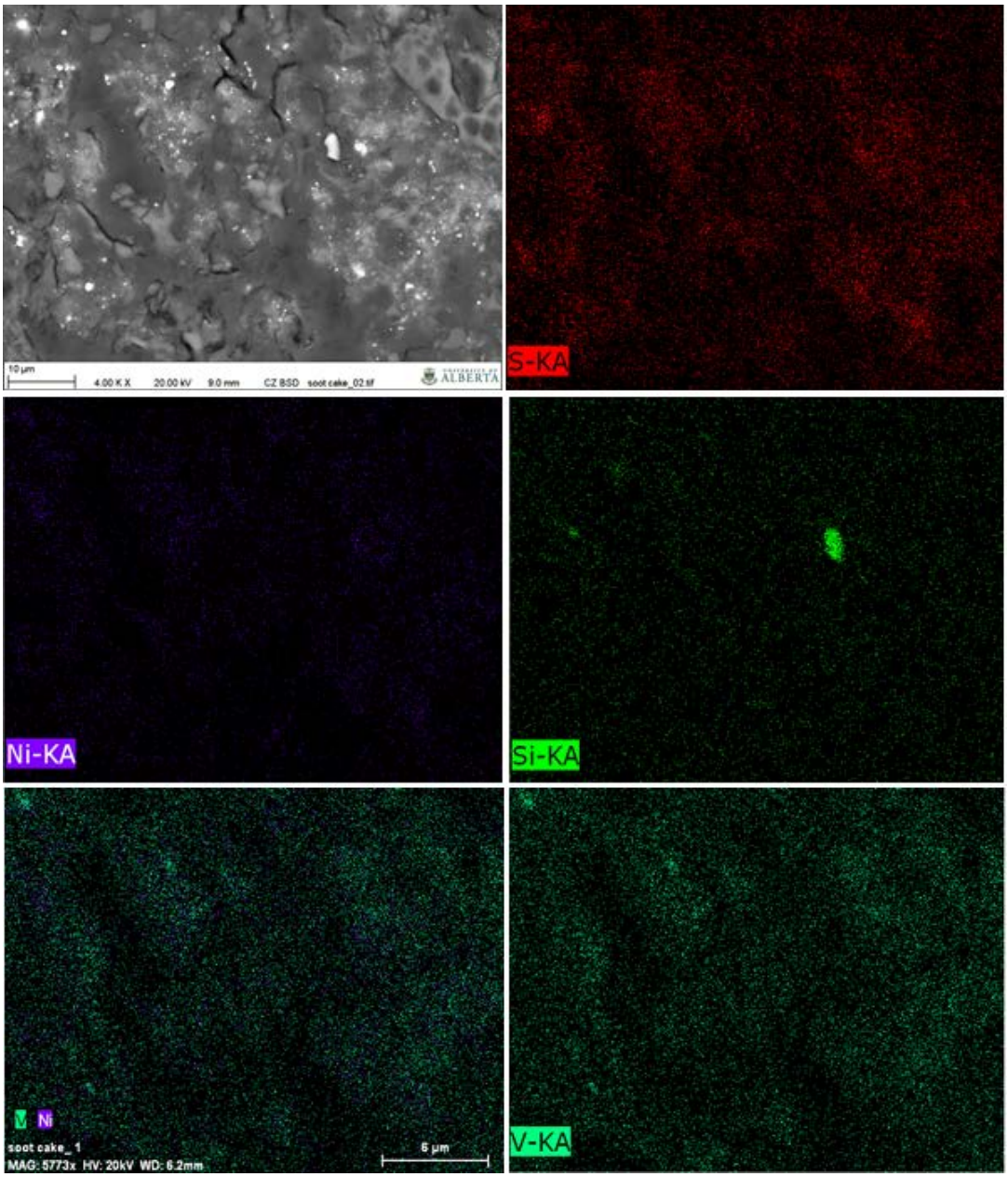

Figure 5.19: BSE image and EDX mapping of the cross-section of soot cake.

Table 5.5: XRF Elemental Analyses of soot cake

Element	**Weight%**
Ni	15.97
Si	0.38
P	0.25
S	18.74
Ca	0.61
Ti	0.51
V	52.4
Fe	0.67
Cr	0.25
Mo	0.62

The sample for SEM characterization is prepared by mounting a piece of soot cake chunk in the epoxy then ground and polished to get the cross-section surface. The back scatter images in Figure 5.19 (a) of the soot cake have three distinguished components. There are dark areas, light grey areas and shining particles. EDX mappings in Figure 5.19 (b)–(f)show different element mappings for S, Ni, Si, V-Ni, and V.

5.3.3 TEM of Soot Water and Soot Cake samples

The soot-water was dried for 24 hrs at 70 °C and then ground to facilitate transmission electron microscopy. The soot powders obtained were placed on copper wire mesh for TEM examination. Figure 5.20 shows the soot micrograph at 6600X magnification. As highlighted in the image, four morphological

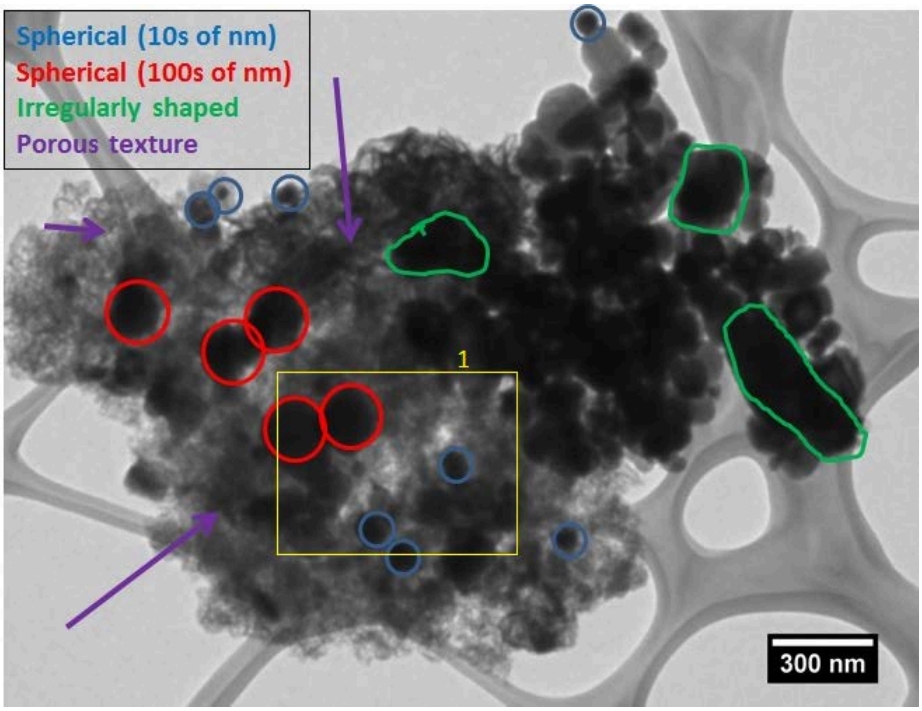

Figure 5.20: Soot particles and textures observed by TEM.

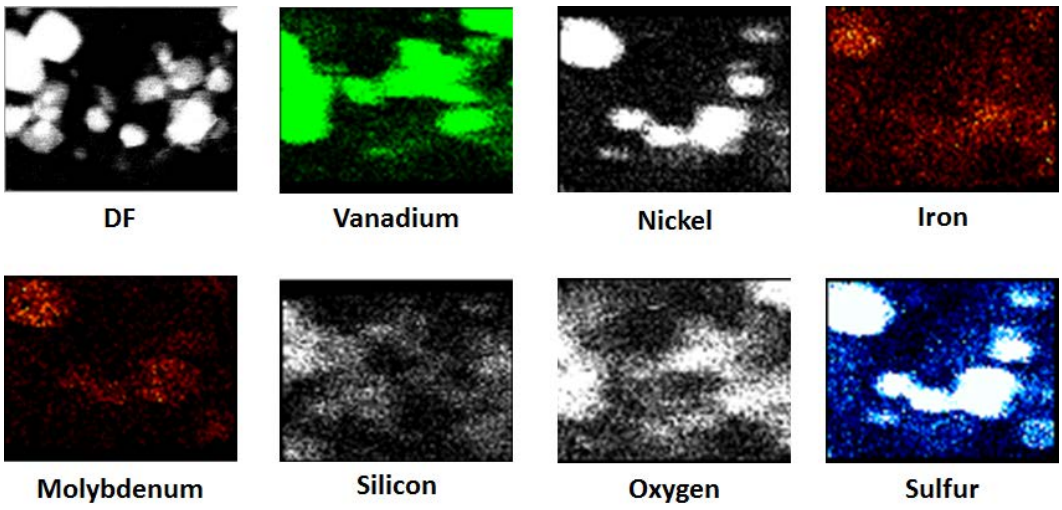

Figure 5.21: EDX map of area 1 of soot, TEM micrograph (DF = dark field image).

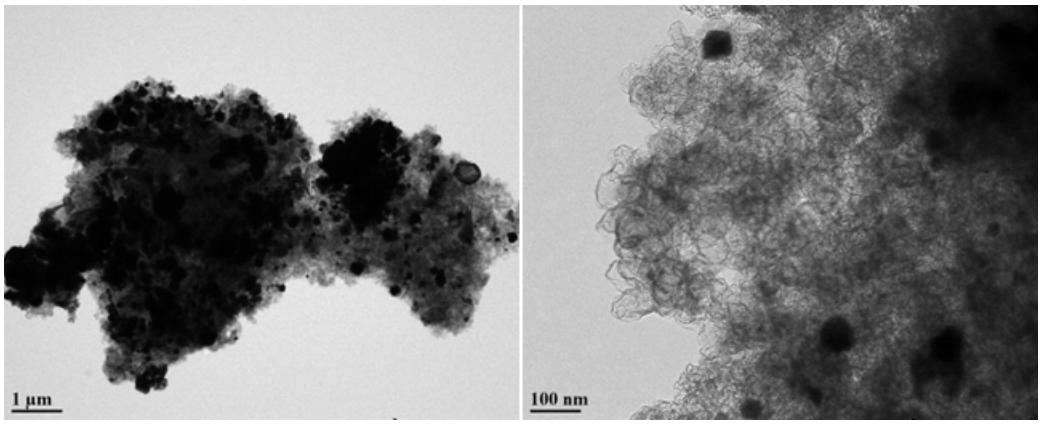

Figure 5.22: TEM Micrographs of soot cake.

features are observed in the micrograph: Spherical and irregularly shaped particles in the submicron range and a fibrous texture with very fine features. The area marked as 1 was scanned to produce EDX maps of observed elements. Figure 5.21 shows the EDX maps. In EDX maps, the overlap of nickel with sulfide and vanadium with oxygen reveals the presence of Ni_3S_2 and V_2O_3 in the soot particles and given the high magnification of these images, the fine size of these particles is confirmed. This has important consequences in the formation of fouling layers in the syngas cooler. The soot-cake samples were also investigated using TEM. Figure 5.22 shows images collected at different magnifications. The micrographs show similar features compared to those observed in the dried soot-water samples. Presence of fine particles in a fibrous matrix and irregularly shaped particles is related to the extent of the gasification.

5.4 Conclusions

In this work, the soot and char were collected and analyzed from pyrolysis at different temperatures, partial oxidation at a fixed temperature for different stoichiometric ratios of oxygen, and steam gasification at a fixed temperature for different steam/fuel ratios, with asphaltene as the fuel feed. The pyrolysis temperature plays a major role in the trace metal content of the char

and soot. At 1000 and 1200 °C, soot contains more trace metals, such as V, Ni, Fe Al, Mg, and Ca, compared to char. At 1400 °C, however, char contains more trace metals compared to soot. With an increase in the pyrolysis temperature, the V and Ni contents decrease for both char and soot. The excess liberation of the organically bound trace metals at higher temperatures is the reason for char to have less concentration of trace metals at high temperatures. However, the inability of soot to capture the excess available trace metals in the reactor results in less value at high temperatures. Some condensed trace metal particles on the surface of the soot also evaporate at high temperatures. An increase in the stoichiometric oxygen content decreases the soot yield during partial oxidation of asphaltenes as a result of the increase in the oxygen/carbon ratio. It is found that the V and Ni contents in both the char ash and soot ash decrease with an increase in stoichiometric oxygen in the feed. The metals in the char react with the available extra oxygen present in the reactor, and that reaction causes the decrease in V and Ni contents in char. For soot, however, the trace metals present react with oxygen. In addition, the condensation of some elements might not take place on the surface of the soot as a result of the oxygen atmosphere. During asphaltene gasification with steam, the V content increases with an increase in the steam/fuel weight ratio for both char and soot. The Ni content slightly decreases in char with an increase in the steam/fuel ratio, whereas the Ni content increases in soot with an increase in the steam/fuel ratio. An understanding of the decomposition of asphaltenes, the subsequent formation of soot, and the interaction of inorganic matter with char and soot will help in solving post-gasification fouling and erosion problems.

Vanadium and nickel are the major metallic components present in soot-water and soot-cake samples collected from the syngas cooler. Presence of other components like calcium, silicon, iron, molybdenum and titanium is also noteworthy as these are the common elements in low fusion temperature components. The studies performed so far do not reveal the type of compounds

these elements formed; therefore, further investigation is required to characterize the type of compounds present in soot samples. The high metallic content in the soot-water and soot-cake shows that collection of metallic species, the act for which soot blowing is intended, has been to some extent successful in preventing slag formation in the gasifier. But the formation of fouling in the SEC should have a different mechanism for which soot blowing has not had a very positive effect. The fouling deposits contain less carbon (2-3 % soot). The metal species evolved during gasification is of different types and the major part of it is captured or associated with soot formed that exits the gasification system as soot-water and soot-cake. But a minor quantity of metals which are not associated with soot are getting deposited when cooled in the syngas cooler. From the entrained-flow reactor experiment results and industrial gasifier soot analysis, we developed a mechanism for soot formation including the pathway for Ni and V as shown in Figure 5.23. The primary soot particles formed from tar polymerization and condensation reactions undergo surface growth reactions with secondary gas products in the presence of primary gases and the metal species liberated during pyrolysis. These metal species may attach to the soot particles during surface growth to get embedded in it. The gasification reactions of the char formed liberate the Ni and V in it and these will be in gas phase. A part of these metals may condense on the surface of the soot particles as shown in the figure and the rest may leave the gasifier as gas phase itself.

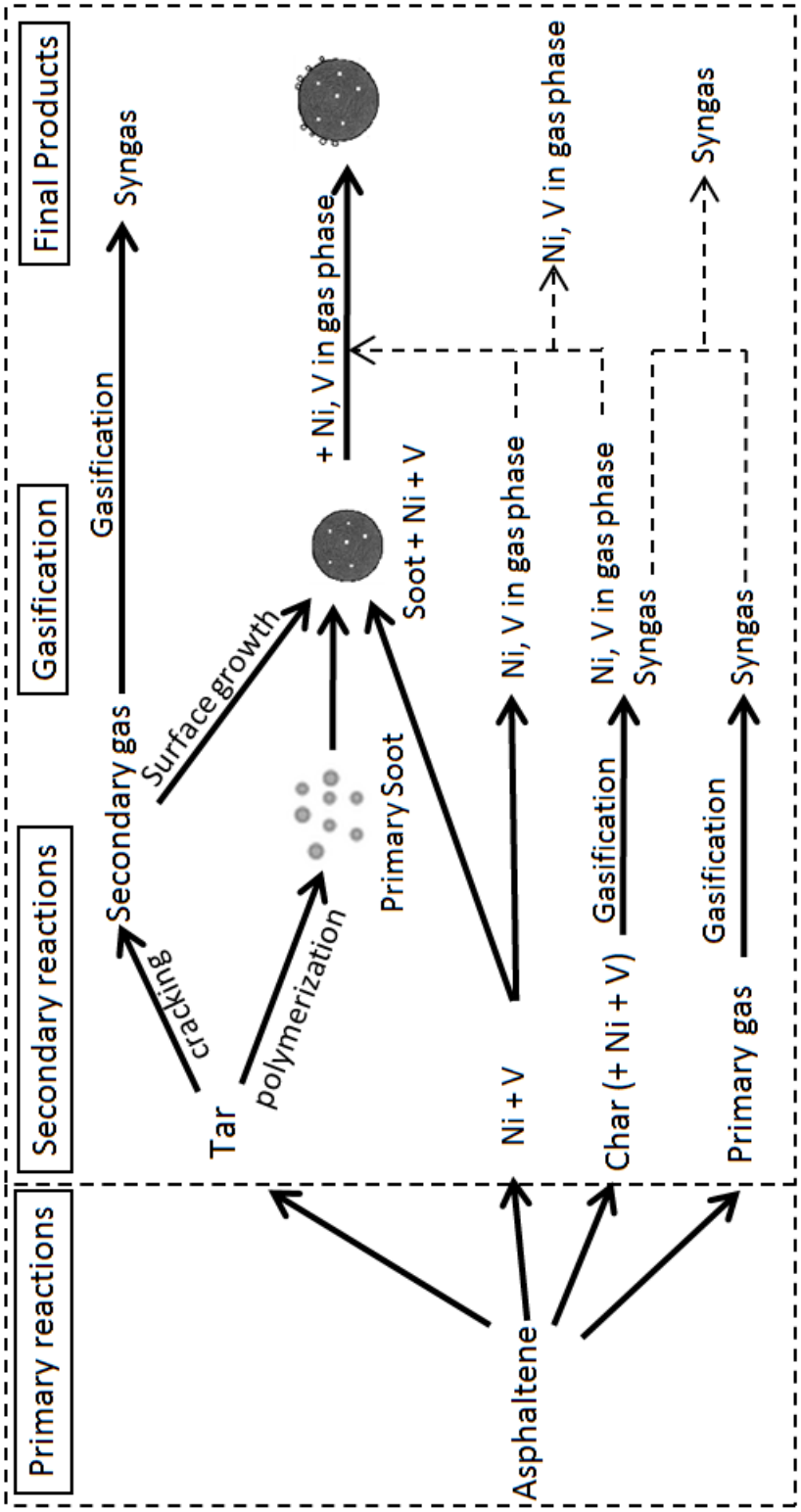

Figure 5.23: Pathways for Ni and V during soot formation.

Chapter 6

CFD Modeling of Soot Formation*

6.1 Introduction

Frenklach et al. [56] modeled the soot particle nucleation and growth in laminar premixed hydrocarbon flames. The simulation of soot particle formation included fuel pyrolysis, polycyclic aromatic hydrocarbon formation and its planar growth, coagulation into spherical particles and also the surface growth and oxidation of particles. The three parts of the model were: (1) initial PAH formation, with detailed chemical kinetic description of acetylene pyrolysis and oxidation, formation of the first aromatic ring, and its subsequent growth to a prescribed size; (2) planar PAH growth, with replicating-type growth of PAHs beyond the prescribed size; and (3) spherical particle formation and growth, consisting of coagulation of PAHs formed in part (2) followed by the growth of the resulting particles by coagulation and surface reactions.

Brown and Fletcher [92] proposed a semi-empirical model for predicting coal-derived soot. The main feature of the model is a transport equation for soot mass fraction. Tar prediction options include either an empirical or a transport equation approach, which directly impacts the source term for soot

*A version of this chapter is accepted for presentation at 8^{th} International Freiberg Conference on IGCC & XtL Technologies, 12–16 June 2016, Cologne, Germany and is to be submitted to the journal *Fuel*.

formation. Also, the number of soot particles per unit mass of gas may be calculated using either a transport equation or an assumed average. Kinetics used was based on Arrhenius rates taken from literature data. Radiative properties are calculated as a function of averaged optical constants, predicted gas temperatures, predicted gas densities, and the soot mass fractions. This model has been incorporated into a comprehensive coal modeling code and evaluated based on comparisons with soot, temperature, and NO_x measurements for three experimental cases. They achieved accurate predictions of soot yields for both laminar and turbulent coal flames. Larger scale turbulent predictions illustrated that inclusion of a soot model changed the local gas temperatures by as much as 300 K and the local NO_x concentration by as much as 250 ppm. These predictions demonstrate the necessity for an accurate soot model in coal combustion systems.

Alam et al. [93] modeled soot formation during coal gasification in a two-stage entrained-flow gasifier using ANSYS FLUENT. A one-step soot formation reaction mechanism is implemented in their study in which an aromatic hydrocarbon molecule like benzene or higher ringed component is considered as a precursor of soot formation and the devolatilization is modeled using the Kobayashi model. They found that formation of soot enhances H_2 production while predicting a low gas temperature in the gasifier. The results showed that soot concentration decreases with an increase in O_2 ratio and CO_2 concentration does not have any effect on soot concentration.

The modeling of soot formation from asphaltene pyrolysis and gasification is carried out in the present study. This basic model includes the devolatilization and soot formation mechanisms to study the effect of temperature and gasification agents on soot formation. Most of the gasification models to predict the syngas composition do not account for the formation of soot. This model can be further extended in future to study the effect of syngas quality when soot formation is also considered.

6.2 Modeling Methodology

Computational fluid dynamics modeling of soot formation during asphaltene pyrolysis and gasification in an entrained-flow reactor is done using ANSYS Fluent 16.0. A two dimensional axi-symmetric model of the entrained-reactor was created using ANSYS workbench and the the meshing was completed using the ICEM CFD software. The model mesh contains 76530 quadrilateral cells with fine cells near the inlet flow regions. The mesh view for the entire reactor as well as the magnified view of the inlet section is shown in Figure 6.1. The fuel asphaltene particles enter the reactor through the inner inlet along with the carrier gas and gasification agent is entering through the annular outer inlet. The inlet region is long enough to allow the inlet profiles to develop. Instead of asphaltene particles, the products of devolatilization are considered as the feed and are represented by the discrete phase model in the FLUENT software. The devolatilization products are assumed to be carbon monoxide, benzene, nitrogen and methane. The flow field of the continuous phase is solved as steady state with two way interaction between the discrete particles. The turbulent flow is modeled using the SST-k-w model. The radiation is modeled using the P1-model. The gas phase is assumed to be an incompressible ideal gas and gravity is enabled. The thermodynamic properties are determined using ideal-gas-mixing-law, the kinetic theory, and the polynomial property function [94].

The simulations were done in different steps, giving the previous results as the initial estimate for the next step and this could improve the convergence. The flow through the reactor is established initially considering the turbulent flow inside the reactor followed by solving energy equation also by imposing the reactor furnace wall temperature as the boundary condition. After the flow through a hot reactor is established, the fuel asphaltene particles are fed with the carrier gas and devolatilization takes place inside the reactor. The Eulerian-Lagrangian approach in ANSYS Fluent is used where the fluid phase

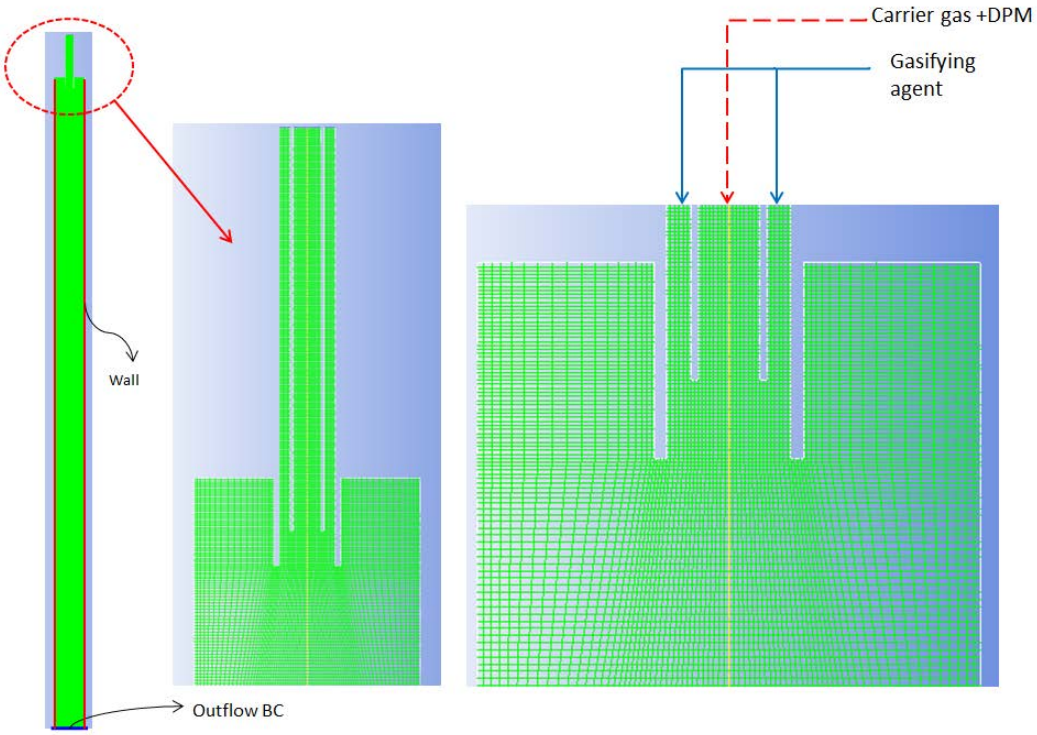

Figure 6.1: Numerical grid of the entrained-flow reactor and the magnified view of the inlet region.

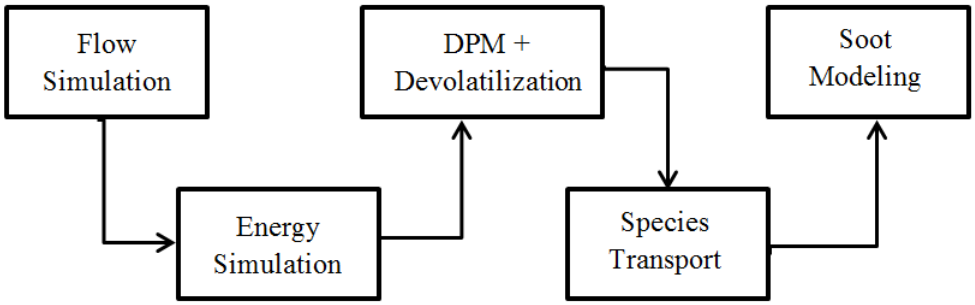

Figure 6.2: Modeling methodology.

is treated as a continuum by solving the Navier-Stokes equations, while the dispersed phase is solved by tracking a large number of particles through the calculated flow field. The dispersed phase can exchange momentum, mass, and energy with the fluid phase. Volumetric species transport reactions are modeled next considering the reaction occurring inside the reactor for different reaction atmospheres. Finally the soot formation is implemented using the Moss-Brooks-Hall model. The modeling methodology block diagram is shown in Figure 6.2.

6.2.1 Governing Equations

Mass conservation equation

The mass conservation or continuity equation for 2D axisymmetric geometries is given by

$$\frac{\partial}{\partial x}(\rho v_x) + \frac{\partial}{\partial r}(\rho v_r) + \frac{\rho v_r}{r} = S_m \tag{6.1}$$

where x is the axial coordinate, r is the radial coordinate, v_x is the axial velocity, and v_r is the radial velocity. The source S_m is the mass added to the continuous phase from the dispersed second phase.

Momentum conservation equations

The axial and radial momentum conservation equations are given by

$$\frac{1}{r}\frac{\partial}{\partial x}(r\rho v_x v_x) + \frac{1}{r}\frac{\partial}{\partial r}(r\rho v_r v_x) = -\frac{\partial p}{\partial x} + \frac{1}{r}\frac{\partial}{\partial x}[r\mu(2\frac{\partial v_x}{\partial x} - \frac{2}{3}(\boldsymbol{\nabla}\cdot\vec{\mathbf{v}}))] + \frac{1}{r}\frac{\partial}{\partial r}[r\mu(\frac{\partial v_x}{\partial r} - \frac{\partial v_r}{\partial x})] + F_x \tag{6.2}$$

and

$$\frac{1}{r}\frac{\partial}{\partial x}(r\rho v_x v_r) + \frac{1}{r}\frac{\partial}{\partial r}(r\rho v_r v_r) = -\frac{\partial p}{\partial r} + \frac{1}{r}\frac{\partial}{\partial x}[r\mu(\frac{\partial v_r}{\partial x} - \frac{\partial v_x}{\partial r})] + \frac{1}{r}\frac{\partial}{\partial r}[r\mu(2\frac{\partial v_r}{\partial r} - \frac{2}{3}(\boldsymbol{\nabla}\cdot\vec{\mathbf{v}}))] - 2\mu\frac{v_r}{r^2} + \frac{2}{3}\frac{\mu}{r}(\boldsymbol{\nabla}\cdot\vec{\mathbf{v}}) + \rho\frac{(v_z)^2}{r} + F_r \tag{6.3}$$

where

$$\boldsymbol{\nabla}\cdot\vec{\mathbf{v}} = \frac{\partial v_x}{\partial x} + \frac{\partial v_r}{\partial r} + \frac{v_r}{r} \tag{6.4}$$

Energy equation

$$\boldsymbol{\nabla}\cdot(\vec{\mathbf{v}}(\rho E + p)) = \boldsymbol{\nabla}\cdot(\sum_j h_j \vec{\mathbf{J_j}}) + S_h + I_{rad} \tag{6.5}$$

Species transport equation

For solving conservation equations for chemical species, ANSYS Fluent predicts the local mass fraction of each species, Y_i, through the solution of a convection-diffusion equation for the i^{th} species. This conservation equation takes the following general form:

$$\boldsymbol{\nabla}\cdot(\rho\vec{\mathbf{v}}Y_i) = -\boldsymbol{\nabla}\cdot\vec{\boldsymbol{J_i}} + R_i + S_i \tag{6.6}$$

where R_i is the net rate of production of species i by chemical reaction and S_i is the rate of creation by addition from the dispersed phase plus any user-defined sources.

Turbulence model

$$\frac{\partial}{\partial x_i}(\rho k u_i) = \frac{\partial}{\partial x_j}\left(\Gamma_k \frac{\partial k}{\partial x_j}\right) + G_k - Y_k + S_k \tag{6.7}$$

$$\frac{\partial}{\partial x_j}(\rho w u_j) = \frac{\partial}{\partial x_j}\left(\Gamma_w \frac{\partial w}{\partial x_j}\right) + G_w - Y_w + D_w + S_w \tag{6.8}$$

Eddy-viscosity is defined as

$$\mu_t = \frac{\rho k}{w} \frac{1}{max[\frac{1}{\alpha^4}, \frac{SF_2}{a_1 w}]} \tag{6.9}$$

Radiation model

The radiation flux is given by

$$q_r = -\frac{1}{3(a+\sigma_s) - C\sigma_s} \boldsymbol{\nabla} G \tag{6.10}$$

where a is the absorption coefficient, σ_s is the scattering coefficient, G is the incident radiation, and C is the linear-anisotropic phase function coefficient.

Devolatilization model

The single kinetic rate devolatilization model assumes that the rate of devolatilization is first-order dependent on the amount of volatiles remaining in the particle

$$-\frac{\mathrm{d}m_p}{\mathrm{d}t} = k[m_p - (1 - f_{v,0})(1 - f_{w,0})m_{p,0}] \tag{6.11}$$

where m_p = particle mass (kg)

$f_{v,0}$ = mass fraction of volatiles initially present in the particle

$f_{w,0}$ = mass fraction of evaporating/boiling material

$m_{p,0}$ = initial particle mass (kg)

k = kinetic rate (s^{-1})

The kinetic rate, k, is defined by input of an Arrhenius type pre-exponential factor and an activation energy:

$$k = A_1 \exp\{-E/RT\} \tag{6.12}$$

Soot Formation Model

The transport equations for normalized radical nuclei concentration b^*_{nuc} and soot mass fraction Y_{soot} given by the Moss-Brookes model are:

$$\frac{\partial(\rho Y_{soot})}{\partial t} + \boldsymbol{\nabla} \cdot (\rho \vec{\mathbf{v}} Y_{soot}) = \boldsymbol{\nabla} \cdot \left(\frac{\mu_t}{\sigma_{soot}} \boldsymbol{\nabla} Y_{soot} \right) + \frac{\mathrm{d}M}{\mathrm{d}t} \tag{6.13}$$

$$\frac{\partial(\rho b^*_{nuc})}{\partial t} + \boldsymbol{\nabla} \cdot (\rho \vec{\mathbf{v}} b^*_{nuc}) = \boldsymbol{\nabla} \cdot \left(\frac{\mu_t}{\sigma_{nuc}} \boldsymbol{\nabla} b^*_{nuc} \right) + \frac{1}{N_{norm}} \frac{\mathrm{d}N}{\mathrm{d}t} \tag{6.14}$$

where Y_{soot}= soot mass fraction

M= soot mass concentration (kg/m^3)

b^*_{nuc}=normalized radical nuclei concentration (particles x10^{-15}/kg)=$\frac{N}{\rho N_{norm}}$

N= soot particle number density (particles/m^3)

N_{norm}= 10^{15} particles

The Moss-Brookes-Hall model [95], which is an extension of the Moss-Brookes model, is applicable for higher hydrocarbon fuels. The extended version is a model developed by Wen et al., [96] based on model extensions proposed by Hall et al., [95] and an oxidation model proposed by Lee et al. [97]. The work of Hall [95] is based on a soot inception rate due to two-ringed and three-ringed aromatics, as opposed to the Moss-Brookes assumption of a soot inception due to acetylene. The inception rate of soot particles was given to be eight times the formation rate of species $C_{10}H_7$ and $C_{14}H_{10}$, as shown by

$$\begin{aligned}(\frac{\mathrm{d}N}{\mathrm{d}t})_{inception} = {} & 8C_{\alpha,1}\frac{N_A}{M_p}[\rho^2(\frac{Y_{C_2H_2}}{W_{C_2H_2}})^2\frac{Y_{C_6H_5}W_{H_2}}{W_{C_6H_5}Y_{H_2}}]\exp\left\{\frac{-T_{\alpha,1}}{T}\right\} \\ & + 8C_{\alpha,2}\frac{N_A}{M_p}[\rho^2\frac{Y_{C_2H_2}Y_{C_6H_6}Y_{C_6H_5}W_{H_2}}{W_{C_2H_2}W_{C_6H_6}W_{C_6H_5}Y_{H_2}}]\exp\left\{\frac{-T_{\alpha,2}}{T}\right\}\end{aligned} \tag{6.15}$$

where $C_{\alpha,1}$ = 127 x 10^{888} s^{-1}, $C_{\alpha,2}$ = 178 x 10^{950} s^{-1}, $T_{\alpha,1}$ = 4378 K, and $T_{\alpha,2}$ = 6390 K as determined by Hall et al. In their model, the mass of an incipient soot particle was assumed to be 1200 kg/kmol (corresponding to 100 carbon atoms, as opposed to 12 carbon atoms used by Brookes and Moss). The mass density of soot was assumed to be 2000 kg/m^3.

The coagulation of soot particles in the free molecular regime is given by

$$(\frac{\mathrm{d}N}{\mathrm{d}t})_{coagulation} = -C_\beta(\frac{24RT}{\rho_{soot}N_A})^{1/2}d_p^{1/2}N^2 \tag{6.16}$$

where C_β is a model constant for coagulation rate and the value is unity, N_A is Avogadro number, and d_p is the mean diameter of a soot particle.

The source term for soot mass concentration from surface growth is

$$(\frac{\mathrm{d}M}{\mathrm{d}t})_{surfacegrowth} = C_\gamma(\frac{X_{sgs}P}{RT})^m \exp\left\{-\frac{T_\gamma}{T}\right\}[(\pi N)^{1/3}(\frac{6M}{\rho_{soot}})^{2/3}]^n \tag{6.17}$$

where C_γ, m and n are model constants. C_γ = 9000.6 $kg.m.kmol^{-1}.s^{-1}$, X_{sgs} is the mole fraction of the participating surface growth species, T_γ = 12100 K which is the activation temperature of surface growth rate.

Benzene is considered as the soot inception compound and the surface growth is assumed to be due to the addition of benzene molecules to the primary soot particles. For the soot oxidation term, oxidation due to O_2 (based on measurements and a model based on Lee et al. [97]) was added, in addition to soot oxidation due to the hydroxyl radical. By assuming that the kinetics of surface reactions are the limiting mechanism and that the particles are small enough to neglect the diffusion effect on the soot oxidation, they derived the specific rate of soot oxidation by molecular oxygen. Therefore, the full soot oxidation term, including that due to hydroxyl radical, is of the form

Table 6.1: Boundary conditions for pyrolysis simulation

Symbol	Unit	1	2	3
T_∞ (wall)	K	1273	1473	1673
T_0 (all inlets)	K	350	350	350
m_F (asphaltene)	g/h	58.8	58.8	58.8
m_{CG} (N_2)	g/h	543.06	543.06	543.06
m_{GA} (N_2)	g/h	232.74	232.74	232.74

$$\begin{aligned}(\frac{\mathrm{d}M}{\mathrm{d}t})_{oxid} &= -C_{oxid}C_{w,1}\eta_{coll}(\frac{X_{OH}P}{RT})\sqrt{T}(\pi N)^{1/3}(\frac{6M}{\rho_{soot}})^{2/3} \\ &\quad - C_{oxid}C_{w,2}(\frac{X_{O_2}P}{RT})\exp\left\{\frac{-T_{w,2}}{T}\right\}\sqrt{T}(\pi N)^{1/3}(\frac{6M}{\rho_{soot}})^{2/3}\end{aligned} \tag{6.18}$$

Here, the collision efficiency is assumed to be 0.13 and the oxidation rate scaling parameter is assumed to be unity. The model constants used are as follows:

$C_{w,1} = 105.81$ kg.m.kmol^{-1}.K$^{-1/2}$.s^{-1}

$C_{w,2} = 8903.51$ kg.m.kmol^{-1}.K$^{-1/2}$.s^{-1}

$T_{w,2} = 19778$ K

6.2.2 Boundary conditions

Mass flow rate normal to the boundary is specified as the boundary condition for both the inlets, one for carrier gas (inner) and the other for gasification agent (outer). Outer wall of the inlet nozzle is kept as stationary, no slip, and zero heat flux. All the walls in the reactor are considered as stationary and smooth with no slip boundary condition. A constant temperature boundary condition is applied to the reactor furnace wall. The boundary condition for the outlet of the reactor is set to be outflow. The discrete phase particles

Table 6.2: Boundary conditions for partial oxidation simulation

Symbol	Unit	1	2	3
T_∞ (wall)	K	1473	1473	1473
T_0 (all inlets)	K	350	350	350
m_F (asphaltene)	g/h	58.8	58.8	58.8
m_{CG} (N_2)	g/h	543.06	543.06	543.06
m_{GA} (Air)	g/h	232.74	387.9	543.06
λ	m^3/m^3	0.13	0.22	0.31

are assumed to reflect once reaching the walls and exit the domain at the outlet of the reactor. The discrete phase is entering through the inner tube of inlet with nitrogen as carrier gas. The boundary conditions for the pyrolysis simulation are given in Table 6.1. The reactor wall temperature is varied from 1273 K to 1673 K keeping all other parameters constant to study the effect of pyrolysis temperature on soot formation. For pyrolysis, the carrier gas as well as gasification agent is nitrogen. For partial oxidation simulation, air is supplied as the gasification agent and the amount of air supplied is used to calculate the value of λ which is the stoichiometric oxygen fraction required for total combustion. Partial oxidation simulations are carried out at a constant temperature of 1473 K to study the effect of stoichiometric oxygen content on soot formation. The boundary conditions for partial oxidation simulations are shown Table 6.2.

6.2.3 Numerical method

ANSYS FLUENT is a control volume based solving method to convert a general scalar transport equation to an algebraic equation that can be solved using numerical methods. This method consists of integrating the transport

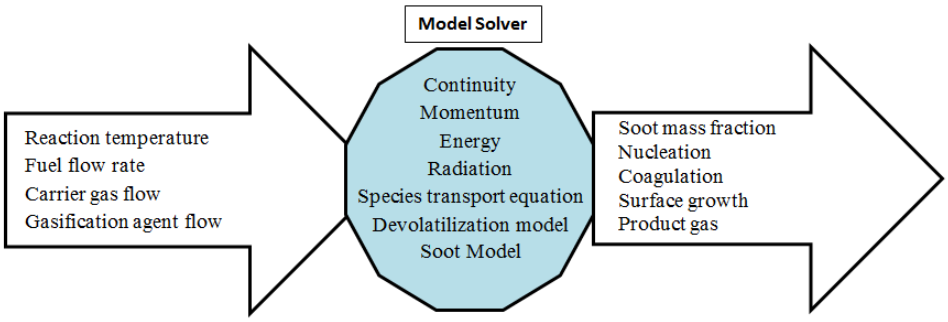

Figure 6.3: Schematic diagram of the model.

equation about each control volume. The pressure-velocity coupling is solved with the standard Fluent coupled scheme and the spatial discretizations are solved with QUICK scheme. The thermodynamic properties of the asphaltene particles are assumed to be constant. The diagram of the model is shown in Figure 6.3 which explains the input required for the model and the main outputs from the solver after solving the required equations.

6.3 Results and Discussion

As discussed earlier the flow and energy simulations are completed initially to establish the flow through the reactor. The carrier gas nitrogen entering through the inner inlet develops a full flow profile before entering the reactor. The velocities are high at the entrance region of the reactor and upon entering the larger diameter reactor, the velocity decreases. Similarly for the temperature profile, the cold gas entering is getting heated from the hot walls as it enters the reactor. The velocity and temperature profiles are shown in Figures 6.4 and 6.5 respectively.

The pyrolysis is conducted at different temperatures and the soot formation is studied. The soot mass fraction along the axial length of the reactor is plotted in Figure 6.6. The axial length is through the axis of symmetry of the reactor. It is observed that the soot mass fraction increases with increase

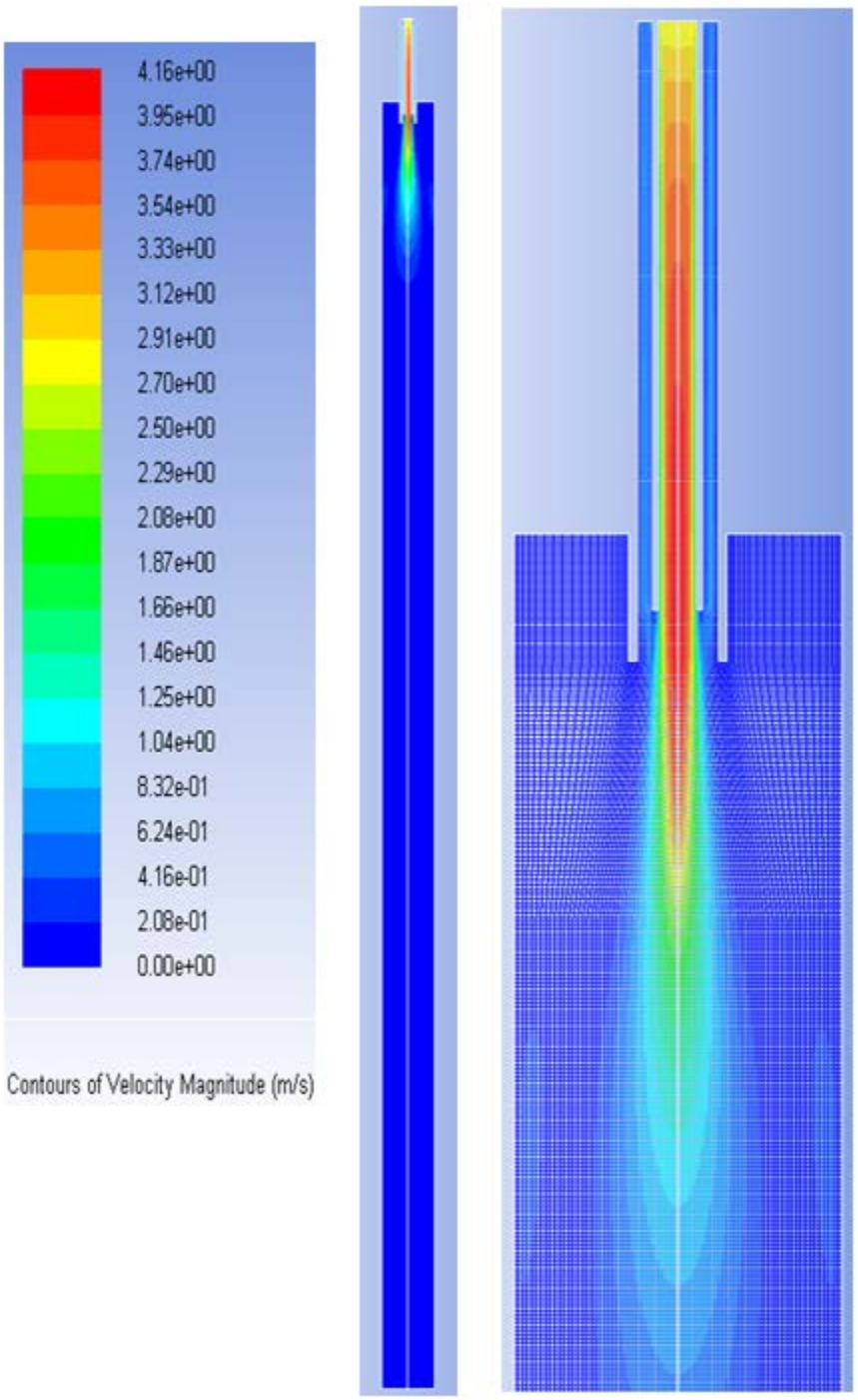

Figure 6.4: Velocity profile in the reactor.

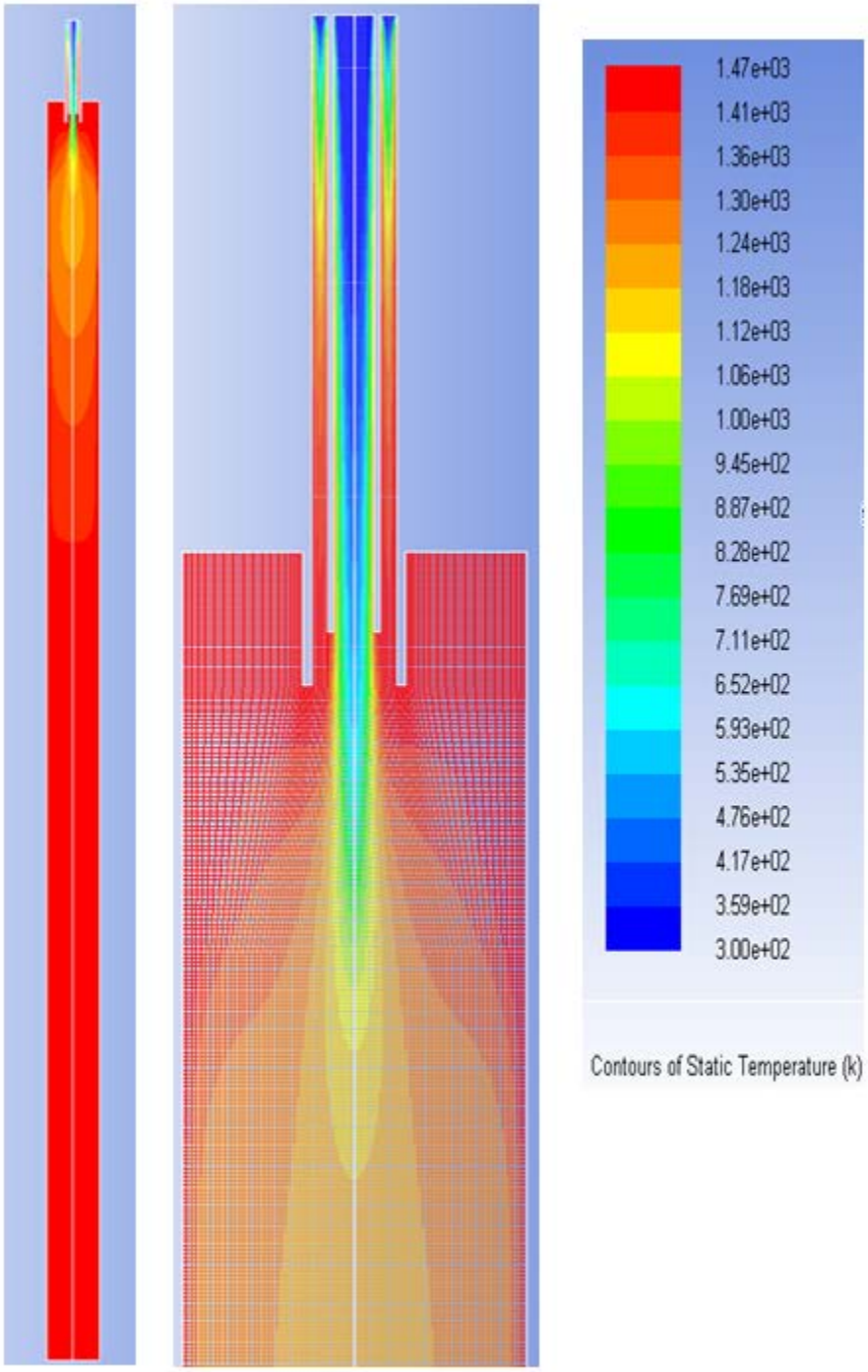

Figure 6.5: Temperature profile in the reactor.

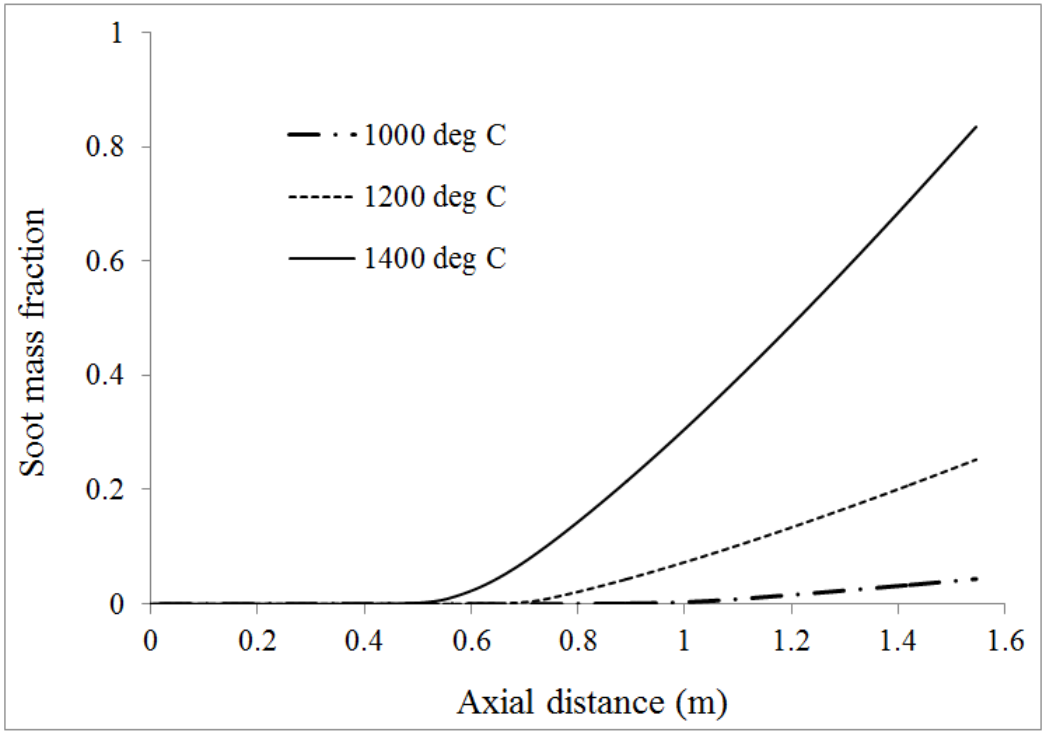

Figure 6.6: Soot mass fraction during pyrolysis along the axial length of the reactor.

in pyrolysis temperature which is in agreement with our own experimental results. The x- axis is the total length of the reactor. At a higher temperature of 1673 K, the soot starts forming even at the entrance region within $(1/3)^{rd}$ length of the reactor, whereas, at a lower temperature of 1273 K, the soot appears only at the final $(1/3)^{rd}$ length of the reactor. This can be explained in terms of soot nucleation, coagulation and surface growth occurring along the axis of the reactor as shown in Figure 6.7. All of these phenomena occur very early in the reactor at higher temperatures and result in high mass fraction of soot at higher temperature. The comparison between the experimental soot mass fraction and its modeling results is shown in Figure 6.8.

Partial oxidation simulations are completed by varying the stoichiometric oxygen available for the reactions. The λ value of 0.13 means the air supplied is only 13 % of what is actually required for completed combustion. As the

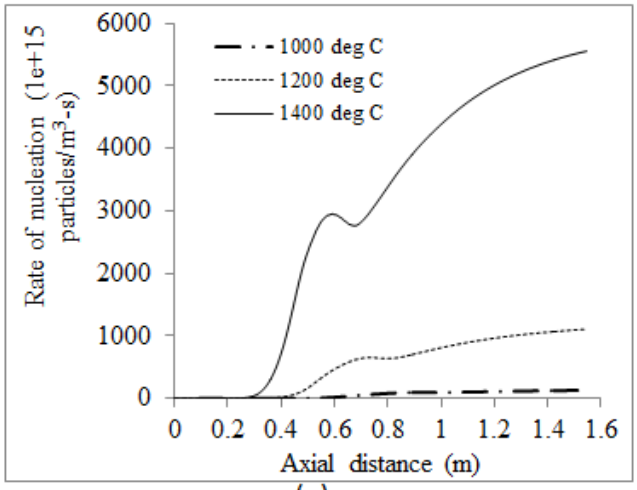

(a)

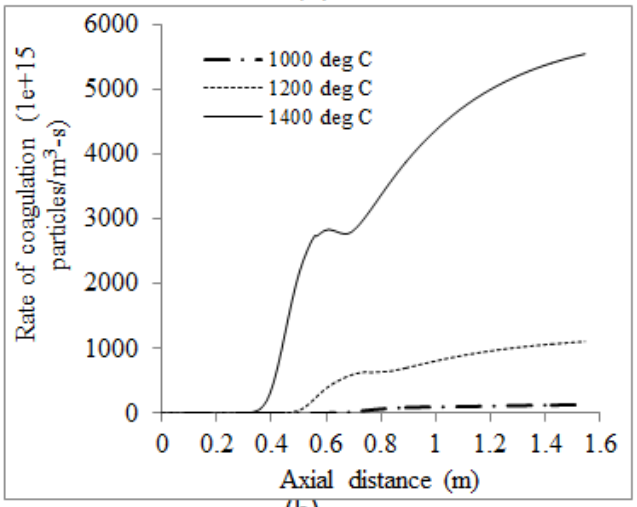

(b)

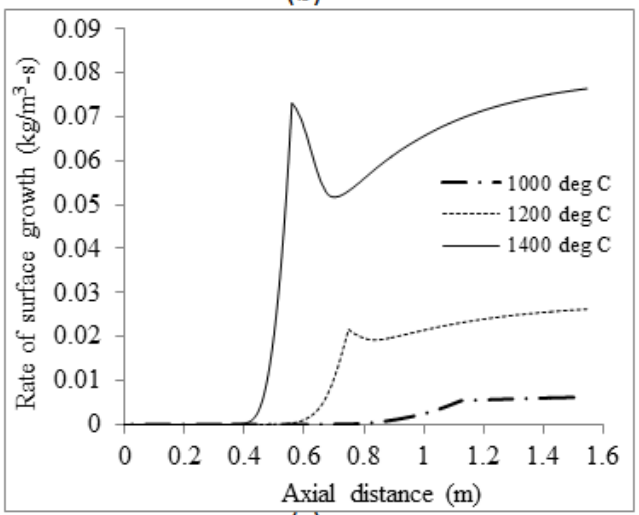

(c)

Figure 6.7: Nucleation, coagulation and surface growth of soot during pyrolysis.

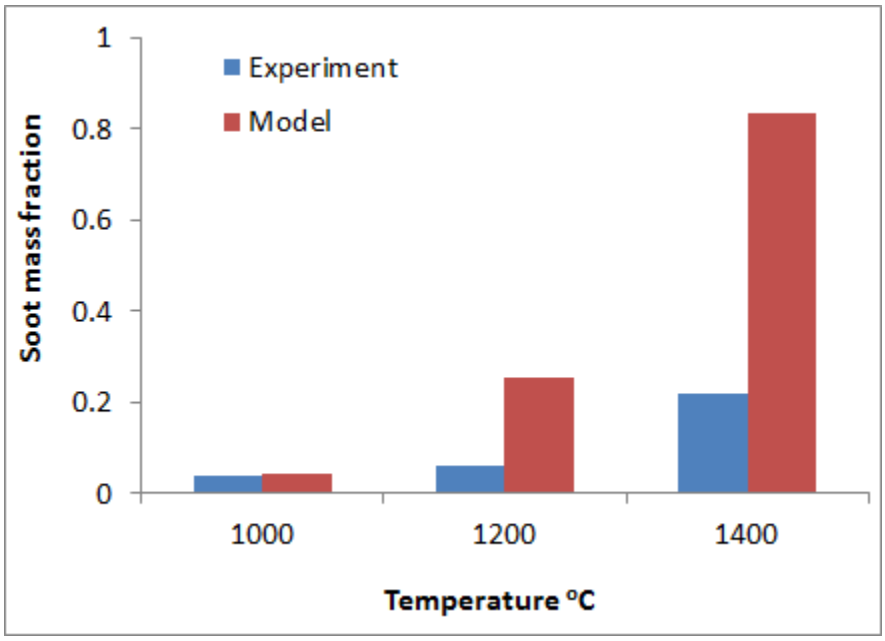

Figure 6.8: Comparison between experimental and modeling results on pyrolysis soot mass fraction.

stoichiometric ratio increases, the soot mass fraction decreases along the axis of the reactor as shown in Figure 6.9 which is in agreement with the literature results [46, 47, 49]. The soot formation is favored by the sub stiochiometric conditions. The incipient nucleation is quite similar for all partial oxidation cases. But the coagulation and surface growth is very rapid for the lower stoichiometric case as shown in Figure 6.10.But the soot oxidation will be maximum for the higher λ value simulation. This results in a higher mass fraction of soot for lower λ value simulations.

6.4 Conclusions

A simple model was developed using ANSYS FLUENT by incorporating the single rate devolatilization model, volumetric species transport reactions and Moss-Brooks-Hall soot model into the basic continuity, momentum and energy equations. The model acts as a simple tool to estimate soot formation in a reactor where the reaction conditions are favorable for soot formation. The influence of different steps of soot formation like nucleation, coagulation, and

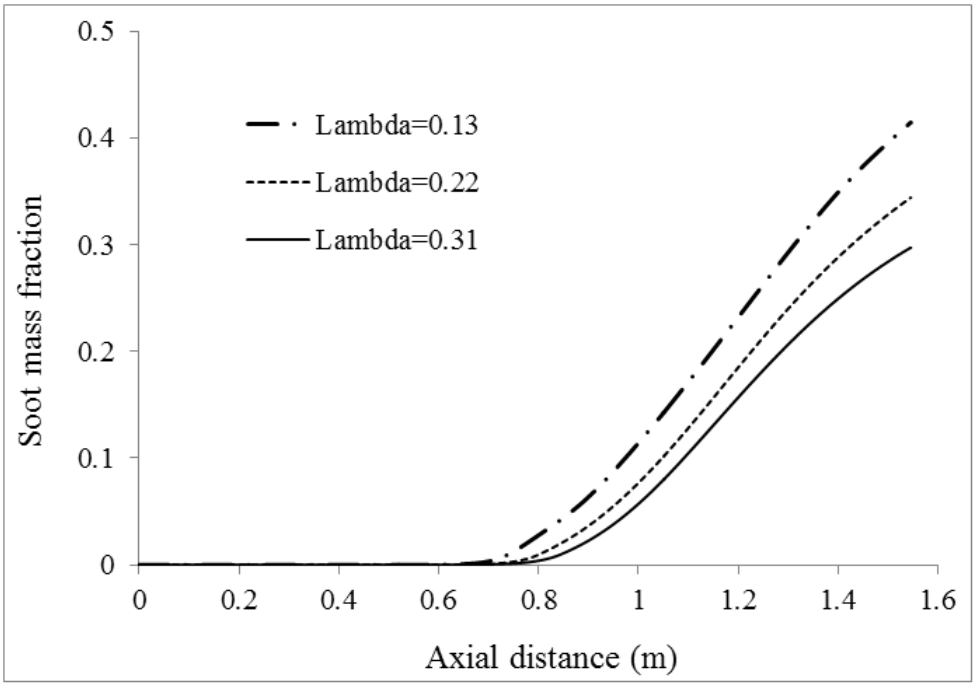

Figure 6.9: Soot mass fraction during partial oxidation along the axial length of the reactor.

surface growth on the soot formation can be analyzed using the model. The model requires refining in terms of different devolatilization mechanisms for various fuels, soot oxidation models, and implementation of detailed chemistry. This model can be used as an initial step for a more comprehensive model for various applications/conditions.

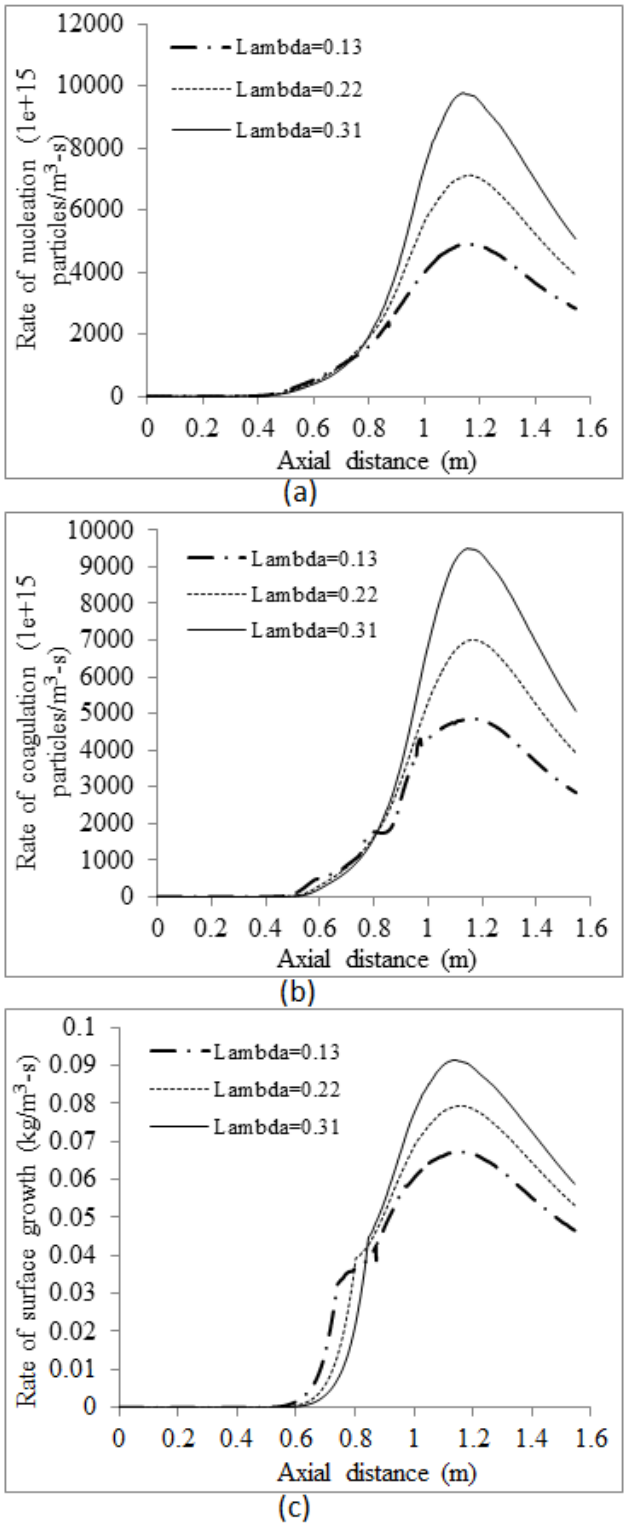

Figure 6.10: Nucleation, coagulation and surface growth of soot during partial oxidation.

Chapter 7

Conclusions and Recommendations

7.1 Conclusions

In this work, soot formation during asphaltene gasification is studied in detail. The dependence of operating conditions on the properties of the soot is analyzed. The main reaction atmospheres considered were pyrolysis, partial oxidation, and steam gasification. The pyrolysis process itself is studied by varying the temperature of the entrained-flow reactor, particle size of the feed, and residence time. The partial oxidation of asphaltene is done at different stoichiometric ratios of oxygen and keeping the temperature constant. The steam gasification experiments are conducted at a fixed temperature for different steam/fuel ratios. The soot collected from each experiment was analyzed for morphology, particle size distribution, and trace metal content.

According to the particle size distribution, morphology, and elemental composition, it was clear that there was no effect of feed particle size on the characteristics of the soot formed. Temperature plays a major role in determining the yield, morphology, and hydrogen and sulfur contents of the soot. The yield of soot increased with increasing temperature over the range of temperatures examined. At low temperatures, tar was found to be mixed with soot, but the soot separated from tar had the same morphology as the soot

formed at higher temperatures. At higher temperatures the tar was converted to soot or light gases. The presence of tar at low temperature confirmed that asphaltenes have a soot formation mechanism similar to that of coal. The size of the primary soot particles decreased with increasing temperature. The observed soot morphology is consistent with the soot inception and surface growth mechanism described. The hydrogen and sulfur contents in the soot decreased with increasing temperature as a result of the release of hydrogen sulfide. The size of primary soot particles increased with increasing pyrolysis residence time because of the extra time available for spherules to undergo surface growth with acetylene and PAHs. Increasing the residence time had no effect on the hydrogen and sulfur contents of the soot. These experiments and analyses could have applications in designing industrial asphaltene gasification systems, where the gasification temperature is >1300 °C and residence time is around 10 s.

The distribution of metals in soot and char formed during the pyrolysis, partial oxidation and steam gasification was investigated. The pyrolysis temperature plays a major role in the trace metal content of the char and soot. At 1000 and 1200 °C, soot contains more trace metals, such as V, Ni, Fe Al, Mg, and Ca, compared to char. At 1400 °C, however, char contains more trace metals compared to soot. With an increase in the pyrolysis temperature, the V and Ni contents decrease for both char and soot. The excess liberation of the organically bound trace metals at higher temperatures is the reason for char to have less concentration of trace metals at high temperatures. However, the inability of soot to capture the excess available trace metals in the reactor results in less value at high temperatures. Some condensed trace metal particles on the surface of the soot also evaporate at high temperatures. An increase in the stoichiometric oxygen content decreases the soot yield during partial oxidation of asphaltenes as a result of the increase in the oxygen/carbon ratio. It is found that the V and Ni contents in both the char ash and soot ash decrease with an increase in stoichiometric oxygen in the feed. The metals in the char react

with the available extra oxygen present in the reactor, and that reaction causes the decrease in V and Ni contents in char. For soot, however, the trace metals present react with oxygen. In addition, the condensation of some elements might not take place on the surface of the soot as a result of the oxygen atmosphere. During asphaltene gasification with steam, the V content increases with an increase in the steam/fuel weight ratio for both char and soot. The Ni content slightly decreases in char with an increase in the steam/fuel ratio, whereas the Ni content increases in soot with an increase in the steam/fuel ratio. An understanding of the decomposition of asphaltenes, the subsequent formation of soot, and the interaction of inorganic matter with char and soot will help in solving post-gasification fouling and erosion problems.

The soot-water, soot-cake and cooler fouling samples collected from an industrial asphaltene gasifier are analyzed to compare with the soot from lab scale entrained-flow reactor. Vanadium and nickel are the major metallic components present in soot-water and soot-cake samples. Presence of other components like calcium, silicon, iron, molybdenum and titanium is also noteworthy as these are the common elements in low fusion temperature components. The studies performed so far do not reveal the type of compounds these elements form; therefore, further investigation is required to characterize the type of compounds present in soot samples. The high metallic content of the soot shows that collection of metallic species, the act for which soot blowing is intended, has been to some extent successful in preventing slag formation in the gasifier. The very low soot content in the fouling sample collected from the syngas cooler concludes that the deposits are formed in the cooler with a different mechanism for which soot blowing has not had a very positive effect. The fouling deposits contain very little carbon (2-3 % soot). The metal species evolved during gasification are of different types and major part of it is captured or associated with soot formed and exit the gasification system as soot-water and soot-cake. But a minor quantity of metals which are not associated with soot are getting deposited when cooled in the syngas cooler.

A CFD model for soot formation is developed using ANSYS FLUENT. The model accounts for devolatilization model, volumetric species transport reactions and Moss-Brooks-Hall soot model in addition to the basic continuity, momentum and energy equations. The model acts as a simple tool to estimate the soot formation in a reactor where the reaction conditions are favorable for soot formation. The influence of different steps of soot formation like nucleation, coagulation, and surface growth on soot formation can be analyzed using the model. This model can be used as a starting point of a more comprehensive model for various applications/conditions.

7.2 Recommendations for future work

- The metals present in the feed asphaltene are not fully captured by soot formed during gasification. The remaining metals either got deposited inside the tube walls in the form of inorganic compounds or liberated in the gaseous phase and collected downstream. It is important to investigate the fate of major metals present in asphaltene during gasification. In order to achieve that, the gaseous, liquid (condensed) and solid products of gasification need to be analyzed in detail. The flue gas leaving the reactor can be passed through water to collect some of the minerals present in the gas.

- The soot formed inside the gasifier undergoes oxidation/combustion reactions according to the oxidation agent availability and reactivity of the soot particle. It is worthwhile to study the difference in reactivities of soot from various processes like pyrolysis, partial oxidation and gasification.

- Computational fluid dynamic modeling of the soot formation from asphaltene gasification can be improved by incorporating different physics to the existing model. The simplifications used in the present comprehensive model can be minimized to achieve a better CFD model. The

model requires refining in terms of different devolatilization mechanisms for various fuels, soot oxidation models, and implementation of detailed chemistry.

Bibliography

[1] International Energy Outlook 2013 (IEO2013), Tech. Rep. DOE/EIA-0484(2013), U.S. Energy Information Administration: Washington, DC, 2013.

[2] The Facts on Oil Sands, Upstream Dialogue, Tech. Rep., Canadian Association of Petroleum Producers: Calgary, AB, 2011.

[3] About Canadas Oil Sands, Tech. Rep., Canadian Association of Petroleum Producers: Calgary, AB, 2012.

[4] R. Kerr, J. Birdgeneau, B. Batt, P. Yang, G. Nieuwenburg, P. Rettger, J. Arnold, Y. Bronicki, The long lake project-the first field integration of SAGD and upgrading, in: SPE International Thermal Operations and Heavy Oil Symposium and International Horizontal Well Technology Conference, Society of Petroleum Engineers, 2002.

[5] Environmental and Health Impacts of Canadas Oil Sands Industry, Tech. Rep., Royal Society of Canada Expert Panel Report, December 2010.

[6] R. P. Dutta, W. C. McCaffrey, M. R. Gray, K. Muehlenbachs, Thermal cracking of Athabasca bitumen: influence of steam on reaction chemistry, Energy & fuels 14 (3) (2000) 671–676.

[7] M. Siskin, S. Kelemen, C. Eppig, L. Brown, M. Afeworki, Asphaltene molecular structure and chemical influences on the morphology of coke produced in delayed coking, Energy & Fuels 20 (3) (2006) 1227–1234.

[8] Crude Oil Forecast, Markets and Pipelines, Tech. Rep., Canadian Association of Petroleum Producers: Calgary, AB, June 2012.

[9] G. J. Stiegel, M. Ramezan, Hydrogen from coal gasification: an economical pathway to a sustainable energy future, International Journal of Coal Geology 65 (3) (2006) 173–190.

[10] E. G. Pereira, J. N. da Silva, J. L. de Oliveira, C. S. Machado, Sustainable energy: a review of gasification technologies, Renewable and Sustainable Energy Reviews 16 (7) (2012) 4753–4762.

[11] R. W. Bryers, Fireside slagging, fouling, and high-temperature corrosion of heat-transfer surface due to impurities in steam-raising fuels, Progress in energy and combustion science 22 (1) (1996) 29–120.

[12] B. Haynes, G. Prado, Soot and PAH Formation in Coal Combustion, Pulverized Coal Combustion: Pollutant Formation and Control (1980) 8–90.

[13] D. Neves, H. Thunman, A. Matos, L. Tarelho, A. Gómez-Barea, Characterization and prediction of biomass pyrolysis products, Progress in Energy and Combustion Science 37 (5) (2011) 611–630.

[14] H. G. Wagner, Soot formation in combustion, in: Symposium (International) on Combustion, vol. 17, Elsevier, 3–19, 1979.

[15] R. Siegel, J. Howell, Thermal Radiation Heat Transfer, 3rd ed, Hemisphere Publishing, Bristol, PA, 1992.

[16] R. Ahluwalia, K. Im, Spectral radiative heat transfer in coal furnaces using a hybrid technique, Tech. Rep., Argonne National Lab., IL (United States), 1994.

[17] R. Bilbao, A. Millera, M. U. Alzueta, Influence of the temperature and oxygen concentration on NOx reduction in the natural gas reburning process, Industrial engineering chemistry research 33 (11) (1994) 2846–2852.

[18] M. Z. Jacobson, Climate response of fossil fuel and biofuel soot, accounting for soot's feedback to snow and sea ice albedo and emissivity, Journal of Geophysical Research: Atmospheres 109 (D21).

[19] M. Ambrogio, G. Saracco, V. Specchia, C. van Gulijk, M. Makkee, J. Moulijn, On the generation of aerosol for diesel particulate filtration studies, Separation and purification technology 27 (3) (2002) 195–209.

[20] J. S. M. Speight, Chemistry of Asphaltenes, chap. On the Molecular Nature of Petroleum Asphaltenes, American Chemical Society: Washington D. C., 1–15, 1981.

[21] R. B. Long, Chemistry of Asphaltenes, chap. The concept of asphaltenes, ACS: Washington DC, 17–27, 1981.

[22] B. Berahman, A Preliminary Study on Pyrolysis and Gasification of Asphaltenes and Coal-Asphaltenes Slurry in Entrained Flow Reactor, Master's thesis, University of Alberta, AB, 2012.

[23] F. Nellensteyn, The constitution of asphalt, J. Inst. Pet 10 (1924) 311–325.

[24] J. Pfeiffer, The Properties of Asphaltic Bitumen, Elsevier, Amsterdam, 1950.

[25] J. M. Sheremata, M. R. Gray, H. D. Dettman, W. C. McCaffrey, Quantitative molecular representation and sequential optimization of Athabasca asphaltenes, Energy & Fuels 18 (5) (2004) 1377–1384.

[26] K. Qian, K. E. Edwards, M. Siskin, W. N. Olmstead, A. S. Mennito, G. J. Dechert, N. E. Hoosain, Desorption and ionization of heavy petroleum molecules and measurement of molecular weight distributions, Energy & fuels 21 (2) (2007) 1042–1047.

[27] M. R. Gray, Consistency of asphaltene chemical structures with pyrolysis and coking behavior, Energy & Fuels 17 (6) (2003) 1566–1569.

[28] E. S. Boek, D. S. Yakovlev, T. F. Headen, et al., Quantitative molecular representation of asphaltenes and molecular dynamics simulation of their aggregation, Energy & Fuels 23 (3) (2009) 1209–1219.

[29] H. Groenzin, O. C. Mullins, Asphaltene molecular size and structure, The Journal of Physical Chemistry A 103 (50) (1999) 11237–11245.

[30] O. C. Mullins, H. Sabbah, J. Eyssautier, A. E. Pomerantz, L. Barre, A. B. Andrews, Y. Ruiz-Morales, F. Mostowfi, R. McFarlane, L. Goual, et al., Advances in asphaltene science and the Yen–Mullins model, Energy & Fuels 26 (7) (2012) 3986–4003.

[31] C. Higman, M. Van der Burgt, Gasification, Gulf professional publishing, 2011.

[32] M. Ashizawa, S. Hara, K. Kidoguchi, J. Inumaru, Gasification characteristics of extra-heavy oil in a research-scale gasifier, Energy 30 (11) (2005) 2194–2205.

[33] H. Watanabe, M. Otaka, S. Hara, M. Ashizawa, K. Kidoguchi, J. Inumaru, Modelling and simulation for extra heavy oil gasification on entrained flow gasifier, in: Proceeding of ASME, international joint power generation conference (IJPGC 2002), Phoenix, USA, 2002.

[34] L. Smith Moreno-Arciniegas, F.-E. Rodríguez-Corredor, L.-E. Afanador-Rey, J.-L. Grosso-Vargas, Syngas obtainment from the gasification of asphaltenes of the San Fernando crude oil, CT&F-Ciencia, Tecnología y Futuro 3 (5) (2009) 189–202.

[35] Y. Chhiti, S. Salvador, J.-m. Commandre, F. Broust, C. Couhert, Wood bio-oil noncatalytic gasification: Influence of temperature, dilution by an alcohol and ash content, Energy & Fuels 25 (1) (2010) 345–351.

[36] B. R. Stanmore, J.-F. Brilhac, P. Gilot, The oxidation of soot: a review of experiments, mechanisms and models, Carbon 39 (15) (2001) 2247–2268.

[37] M. Mallardo, Experimental Methods for Structural and Morphological Study of Fine and Ultrafine Particulate Produced from Combustion Processes, Ph.D. thesis, Università degli Studi di Napoli Federico II, 2010.

[38] H. Wang, M. Frenklach, A detailed kinetic modeling study of aromatics formation in laminar premixed acetylene and ethylene flames, Combustion and flame 110 (1) (1997) 173–221.

[39] H. Richter, J. B. Howard, Formation of polycyclic aromatic hydrocarbons and their growth to soota review of chemical reaction pathways, Progress in Energy and Combustion science 26 (4) (2000) 565–608.

[40] M. S. Skjøth-Rasmussen, P. Glarborg, M. Østberg, M. B. Larsen, S. Sørensen, J. E. Johnsson, A. Jensen, T. Christensen, A study of benzene formation in a laminar flow reactor, Proceedings of the Combustion Institute 29 (1) (2002) 1329–1336.

[41] M. Frenklach, Reaction mechanism of soot formation in flames, Physical Chemistry Chemical Physics 4 (11) (2002) 2028–2037.

[42] I. M. Kennedy, Models of soot formation and oxidation, Progress in Energy and Combustion Science 23 (2) (1997) 95–132.

[43] J. A. Koziński, R. Saade, Effect of biomass burning on the formation of soot particles and heavy hydrocarbons. An experimental study, Fuel 77 (4) (1998) 225–237.

[44] K. Qin, W. Lin, P. A. Jensen, A. D. Jensen, High-temperature entrained flow gasification of biomass, Fuel 93 (2012) 589–600.

[45] J. Ma, Soot formation during coal pyrolysis, Ph.D. thesis, Brigham Young University, 1996.

[46] A. T. Wijayanta, M. S. Alam, K. Nakaso, J. Fukai, M. Shimizu, Optimized combustion of biomass volatiles by varying O 2 and CO 2 levels:

A numerical simulation using a highly detailed soot formation reaction mechanism, Bioresource technology 110 (2012) 645–651.

[47] A. T. Wijayanta, M. S. Alam, K. Nakaso, J. Fukai, Numerical investigation on combustion of coal volatiles under various O 2/CO 2 mixtures using a detailed mechanism with soot formation, Fuel 93 (2012) 670–676.

[48] J. C.-Y. Chen, Effects of secondary reactions on product distribution and nitrogen evolution from rapid coal pyrolysis, Ph.D. thesis, Stanford University, Stanford, CA, 1991.

[49] G. Chen, Y. Zhang, J. Zhu, Y. Cao, W. Pan, Coal and biomass partial gasification and soot properties in an atmospheric fluidized bed, Energy & Fuels 25 (5) (2011) 1964–1969.

[50] R. D. Nenniger, Aerosol Produced from Coal Pyrolysis, Ph.D. thesis, Massachusetts Institute of Technology, Cambridge, MA, 1986.

[51] S. V. Shurupov, Some factors that govern particulate carbon formation during pyrolysis of hydrocarbons, Proceedings of the Combustion Institute 28 (2) (2000) 2507–2514.

[52] B. S. Haynes, H. G. Wagner, Soot formation, Progress in Energy and Combustion Science 7 (4) (1981) 229–273.

[53] A. F. Sarofim, J. P. Longwell, M. J. Wornat, J. Mukherjee, The role of biaryl reactions in PAH and soot formation, in: Soot formation in combustion, Springer, 485–499, 1994.

[54] J. A. Miller, C. F. Melius, Kinetic and thermodynamic issues in the formation of aromatic compounds in flames of aliphatic fuels, Combustion and Flame 91 (1) (1992) 21–39.

[55] J. Warnatz, U. Maas, R. Dibble, Combustion: physical and chemical fundamentals, modeling and simulation, experiments, pollutant formation. 2006, Springer, 2006.

[56] M. Frenklach, H. Wang, Detailed modeling of soot particle nucleation and growth, in: Symposium (International) on Combustion, vol. 23, Elsevier, 1559–1566, 1991.

[57] A. Karimi, K. Qian, W. N. Olmstead, H. Freund, C. Yung, M. R. Gray, Quantitative evidence for bridged structures in asphaltenes by thin film pyrolysis, Energy & Fuels 25 (8) (2011) 3581–3589.

[58] S. Rahmani, W. C. McCaffrey, H. D. Dettman, M. R. Gray, Coking kinetics of asphaltenes as a function of chemical structure, Energy & fuels 17 (4) (2003) 1048–1056.

[59] Y. Zhao, M. R. Gray, K. H. Chung, Molar kinetics and selectivity in cracking of Athabasca asphaltenes, Energy & fuels 15 (3) (2001) 751–755.

[60] Y. Zhao, F. Wei, Y. Yu, Effects of reaction time and temperature on carbonization in asphaltene pyrolysis, Journal of Petroleum Science and Engineering 74 (1) (2010) 20–25.

[61] A. Bowden, P. Draper, H. Rowling, The problem of fuel-oil ash deposition in open-cycle gas turbines, Proceedings of the Institution of Mechanical Engineers 167 (1) (1953) 291–312.

[62] M. A. Duchesne, A. Y. Ilyushechkin, R. W. Hughes, D. Y. Lu, D. J. McCalden, A. Macchi, E. J. Anthony, Flow behaviour of slags from coal and petroleum coke blends, Fuel 97 (2012) 321–328.

[63] F. Frandsen, K. Dam-Johansen, P. Rasmussen, Trace elements from combustion and gasification of coalan equilibrium approach, Progress in energy and combustion science 20 (2) (1994) 115–138.

[64] S. Bonnamy, A. Oberlin, J. Trichet, Two examples of uranium associated with organic matter, Organic Geochemistry 4 (2) (1982) 53–61.

[65] S. Bonnamy, A. Oberlin, Heat-treatment of two heavy petroleum products containing vanadium and nickel, Carbon 20 (6) (1982) 499–504.

[66] W. H. O. (WHO), et al., Air quality guidelines for Europe. WHO regional publication, European series, World Health Organization, Regional Office for Europe, Copenhagen .

[67] X. Liu, Y. Zhang, S. Yi, C. Huang, J. Liao, H. Li, D. Xiao, H. Tao, Preparation of V 2 O 3 nanopowders by supercritical fluid reduction, The Journal of Supercritical Fluids 56 (2) (2011) 194–200.

[68] Dekati low pressure impactor user manual ver. 3.4, 2007.

[69] N. Mahapatra, Pyrolysis of asphaltenes in an atmospheric entrained flow reactor: A study on gasification reactivity and properties of chars, Master's thesis, University of Alberta, AB, 2014.

[70] N. Mahapatra, V. Kurian, B. Wang, F. Martens, R. Gupta, Pyrolysis of asphaltenes in an atmospheric entrained flow reactor: A study on char characterization, Fuel 152 (2015) 29–37.

[71] R. G. S. Ritchie, R. S. Roche, W. Steedman, Non-isothermal programmed pyrolysis studies of oil sand bitumens and bitumen fractions: 1. Athabasca asphaltene, Fuel 64 (3) (1985) 391–399.

[72] H. Zhang, Nitrogen evolution and soot formation during secondary coal pyrolysis, Ph.D. thesis, Brigham Young University, Provo, UT, 2001.

[73] J. B. Howard, Carbon addition and oxidation reactions in heterogeneous combustion and soot formation, Proc.Combust.Inst. 23 (1990) 1107–1127.

[74] M. J. Wornat, A. F. Sarofim, J. P. Longwell, Pyrolysis-induced changes in the ring number composition of polycyclic aromatic compounds from a high volatile bituminous coal, Twenty-Second Symposium (International) on Combustion (1988) 135–143.

[75] J. Ma, T. H. Fletcher, B. W. Webb, Thermophoretic sampling of coal-derived soot particles during devolatilization, Energy & fuels 9 (5) (1995) 802–808.

[76] M. J. Wornat, A. F. Sarofim, J. P. Longwell, Changes in the degree of substitution of polycyclic aromatic compounds from pyrolysis of a high-volatile bituminous coal, Energy & fuels 1 (5) (1987) 431–437.

[77] K. R. Doolan, J. C. Mackie, R. J. Tyler, Coal flash pyrolysis: secondary cracking of tar vapours in the range 870–2000 K, Fuel 66 (4) (1987) 572–578.

[78] P. R. Solomon, M. A. Serio, E. M. Suuberg, Coal pyrolysis: experiments, kinetic rates and mechanisms, Progress in Energy and Combustion Science 18 (2) (1992) 133–220.

[79] M. Wentzel, H. Gorzawski, K.-H. Naumann, H. Saathoff, S. Weinbruch, Transmission electron microscopical and aerosol dynamical characterization of soot aerosols, Journal of aerosol science 34 (10) (2003) 1347–1370.

[80] H. Groenzin, O. C. Mullins, Molecular size and structure of asphaltenes from various sources, Energy & Fuels 14 (3) (2000) 677–684.

[81] R. Filby, D. Strong, Nickel (II) and vanadium (IV) complexes in Alberta oil-sand bitumens, in: Tar sand and oil upgrading technology. AIChE symposium series, vol. 282, 1–9, 1991.

[82] L. Zychlinski, J. Z. Byczkowski, A. P. Kulkarni, Toxic effects of long-term intratracheal administration of vanadium pentoxide in rats, Archives of environmental contamination and toxicology 20 (3) (1991) 295–298.

[83] R. G. Cooper, Vanadium pentoxide inhalation, Indian journal of occupational and environmental medicine 11 (3) (2007) 97–102.

[84] L. F. Drbal, P. G. Boston, K. L. Westra, Power Plant Engineering by Black and Veatch, Springer, Newyork, 1996.

[85] B. Wang, V. Kurian, N. Mahapatra, F. Martens, R. Gupta, Investigation of corrosion and fouling in syngas cooler tubes, Fuel Processing Technology 141 (2016) 202–209.

[86] A. Williams, Fundamentals of oil combustion, in: Energy Combust. Sci, vol. 2, 167–179, 1976.

[87] G. L. Fisher, D. Chang, M. Brummer, Fly ash collected from electrostatic precipitators: microcrystalline structures and the mystery of the spheres, Science 192 (4239) (1976) 553–555.

[88] R. D. Smith, J. A. Campbell, K. K. Nielson, Characterization and formation of submicron particles in coal-fired plants, Atmospheric Environment (1967) 13 (5) (1979) 607–617.

[89] H. Dunning, J. Moore, H. Bieber, R. Williams, Porphyrin, Nickel, Vanadium, and Nitrogen in Petroleum., Journal of Chemical and Engineering Data 5 (4) (1960) 546–549.

[90] C. Allouis, F. Beretta, A. DAlessio, Structure of inorganic and carbonaceous particles emitted from heavy oil combustion, Chemosphere 51 (10) (2003) 1091–1096.

[91] G. Chilingarian, T. Yen, Asphaltenes and Asphalts, 1, vol. 40, Elsevier, 1994.

[92] A. L. Brown, T. H. Fletcher, Modeling soot derived from pulverized coal, Energy & fuels 12 (4) (1998) 745–757.

[93] M. S. Alam, A. T. Wijayanta, K. Nakaso, J. Fukai, Study on coal gasification with soot formation in two-stage entrained-flow gasifier, International Journal of Energy and Environmental Engineering 6 (3) (2015) 255–265.

[94] FLUENT User's Guide, ANSYS Release 16.0, Chapter 7: Physical Properties, 2014.

[95] R. Hall, M. Smooke, M. Colket, Physical and chemical aspects of combustion, Gordon and Breach .

[96] Z. Wen, S. Yun, M. Thomson, M. Lightstone, Modeling soot formation in turbulent kerosene/air jet diffusion flames, Combustion and Flame 135 (3) (2003) 323–340.

[97] K. Lee, M. Thring, J. Beer, On the rate of combustion of soot in a laminar soot flame, Combustion and Flame 6 (1962) 137–145.

Appendix A

Appendix

A.1 Temperature calibration of the reactor

The temperature set points for the mullite tube is specified using the Labview software from the computer attached to the heating controller. Three thermocouples are fixed at three different heights (named top, middle and bottom) of the mullite tube for the temperature feedback for heating. The thermocouples are touching the outside wall of the reactor tube. Once the heating of the reactor is completed, all three thermocouples show the same temperature according to the set point. But the actual inside temperature of the reactor may be different because of the end effects due to ambient heating. Therefore, the temperature calibration of the reactor is completed using a long calibrated thermocouple manufactured by Omega Engineering Inc. This thermocouple is calibrated for different temperatures such as 600, 800, and 1250 °C. For the temperature calibration of the reactor, initially the reactor is heated to a set point. After that, the long thermocouple is positioned at different locations along the length of the reactor and the temperature values shown by the thermocouple are noted. The thermocouple tip is maintained at the middle part of the cross section of the tube by placing a circular fiberfrax sheet at the tip of the thermocouple. The calibration is completed for 800 °C and 1000 °C and the details are shown in Figure A.1. The end effects are clearly seen in the calibration results as expected. For 800 °C set point, the inside temperature was as low as 700 °C at both ends and the value went as high as 890 °C in the

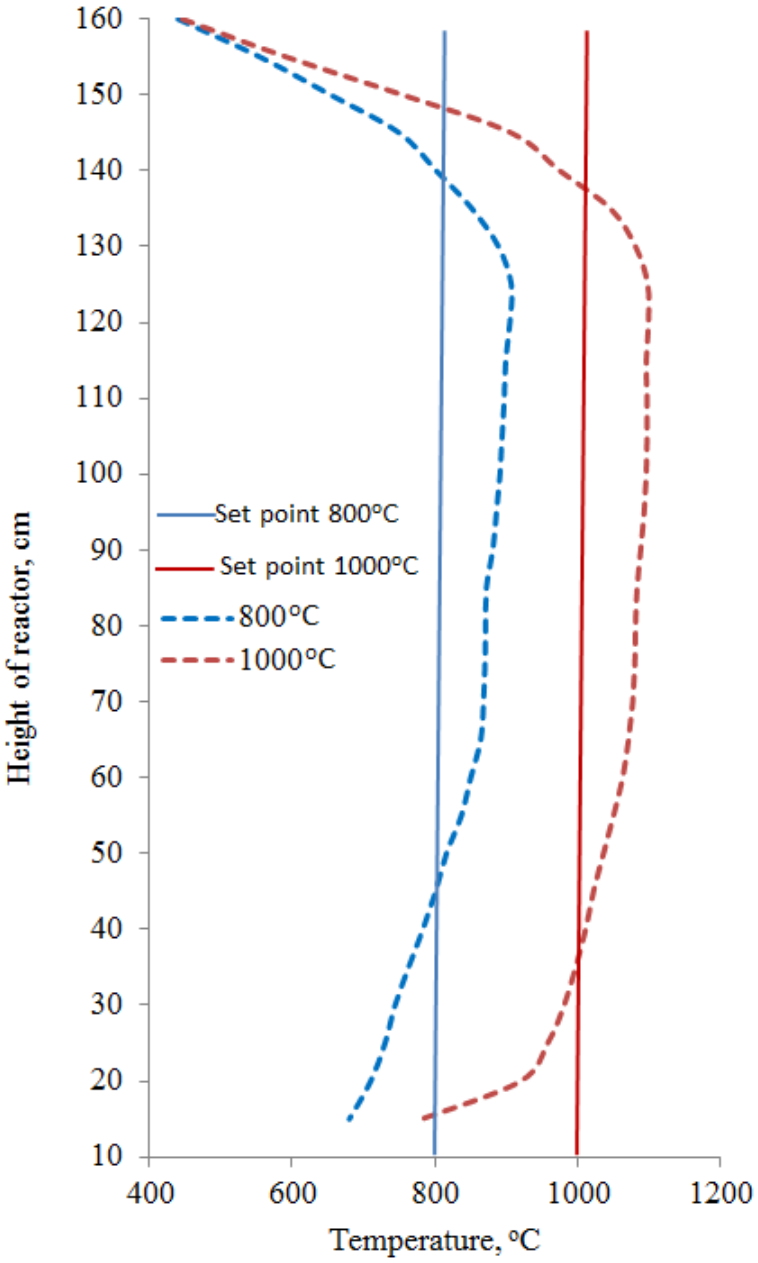

Figure A.1: Temperature calibration of the reactor.

middle section of the tube.

A.2 Process Flow Diagram of the experimental set up

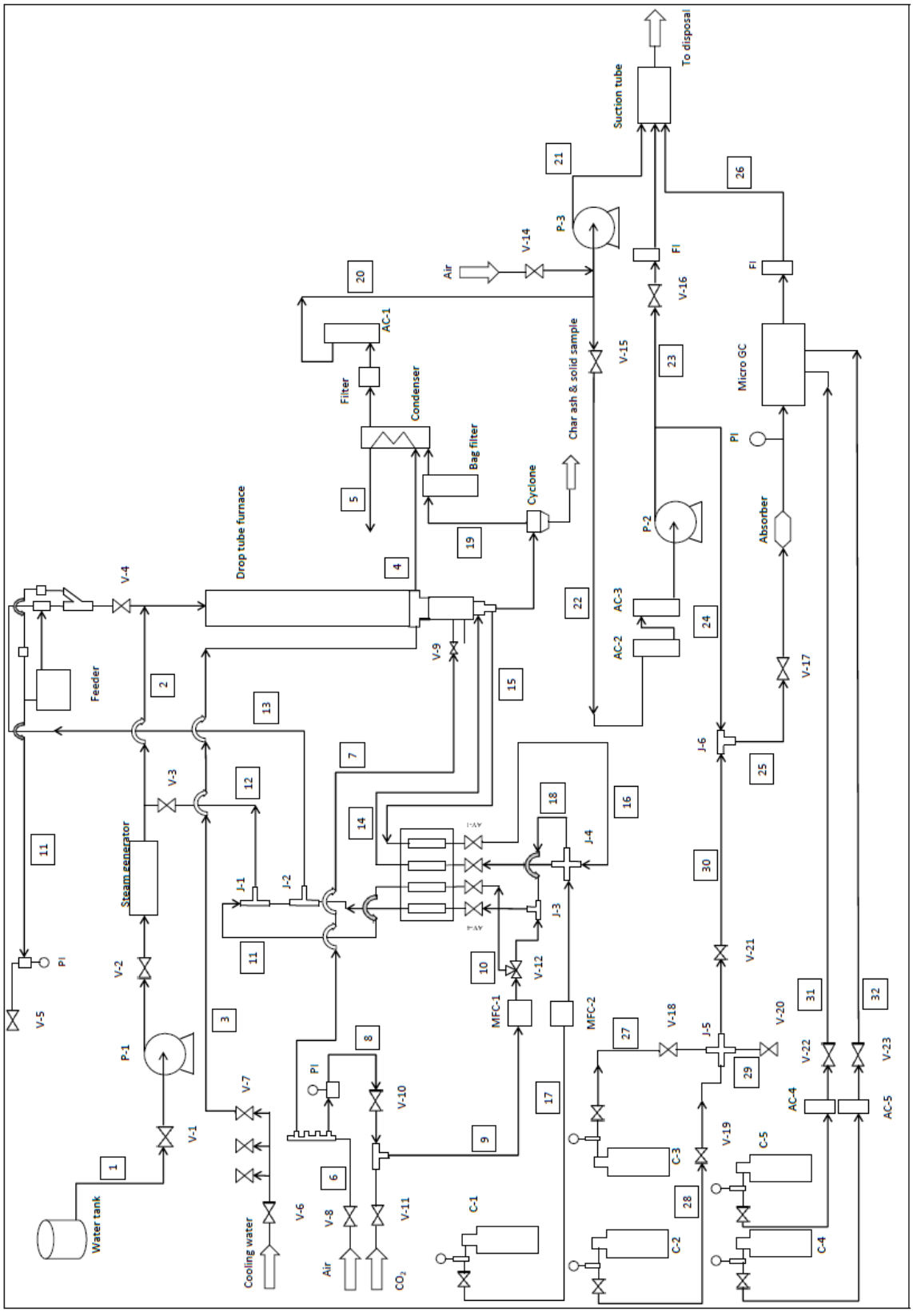

Figure A.2: Process flow diagram of the set up.